JOURNAL

DES MATERIAUX NUCLEAIRES

OF NUCLEAR MATERIALS

CONTENTS

Papers or letters should be sent to one of the Editors,

R. W. CAHN (Dept. of Metallurgy, University of Birmingham, Birmingham 15, England).
J. P. HOWE (Atomics International, P.O. Box 309, Canoga Park, California, U.S.A.).
P. LACOMBE (Centre de Recherches Métallurgiques de l'Ecole des Mines, Blvd. St. Michel 60, Paris VI, France)

either directly or through a member of the Editorial Advisory Board.

Papers or letters should be written in English, French or German; papers should have a summary in the appropriate language. Translations of the summary into the two other languages will be added by the Editors.

Instructions to contributors will be found in Vol. 1, No. 1 (pp. 111–112).

Books for review should be sent to one of the Editors.

The Journal of Nuclear Materials will initially be published quarterly.

The subscription price of a volume of 360 pages is $18.00, 130 s., Gld. 68.50 per volume, post-free.

Subscriptions should be sent to the publishers, North-Holland Publishing Company. P.O. Box 103, Amsterdam or to any subscription-agent.

Les articles ou les lettres devront être envoyés à un des Rédacteurs-en-chef,

R. W. CAHN (Dept. of Metallurgy, University of Birmingham, Birmingham 15, England).
J. P. HOWE (Atomics International, P.O. Box 309, Canoga Park, California, U.S.A.).
P. LACOMBE (Centre de Recherches Métallurgiques de l'Ecole des Mines, 60 Bd. St. Michel, Paris VI, France)

ou directement ou par un membre du Conseil des Rédacteurs.

Les articles ou les lettres devront être rédigés en anglais, français ou allemand, les articles avec un résumé dans la langue correspondante. Les traductions du résumé dans les deux autres langues seront ajoutées par les éditeurs.

Les instructions aux auteurs se trouvent dans le Vol. 1, No. 2 (pp. 211–212).

Les Livres (exemplaires de presse) devront être envoyés à un des Rédacteurs-en-chef.

Le Journal des Matériaux Nucléaires paraîtra initialement tous les trois mois.

Prix de souscription par volume d'environ 360 pages: $18.00, 130 s., Gld. 68.50, franco.

Les abonnements devront être envoyés aux éditeurs, North-Holland Publishing Company, P.O. Box 103, Amsterdam, ou à votre librairie.

REVIEW ARTICLE

THE NATURE AND PROPERTIES OF TRANSITION METAL HYDRIDES

G. G. LIBOWITZ

Atomics International, A Division of North American Aviation, Inc., Canoga Park, California, USA

The basic chemical and physical properties of transition metal hydrides are reviewed with particular emphasis on the hydride phases rather than dilute solutions of hydrogen in metals. The review includes discussions of the phases present in metal-hydrogen systems, their crystal structures, pressure-composition-temperature relations, thermodynamic properties, and electrical and magnetic properties.

The nature of transition metal hydrides is considered. Evidence is given to show that they are definite chemical compounds (rather than solid solutions) having some degree of ionic character. The large deviations from stoichiometry exhibited by these compounds can be explained on the basis of lattice defects.

Les propriétés chimiques et physiques fondamentales des hydrures des métaux de transition sont passées en revue en insistant particulièrement sur les phases hydrures plutôt que sur les solutions diluées d'hydrogène dans les métaux. Cette mise au point discute des phases présentes dans les systèmes métal-hydrogène, de leurs structures cristallines, des relations entre pression, composition et température, des propriétés thermodynamiques et des propriétés électriques et magnétiques.

La nature des hydrures des métaux de transition est examinée. Il est démontré que ce sont des composés chimiques définis (plutôt que des solutions solides) possédant un certain caractère ionique. Les grands écarts à la stoechiométrie que présentent ces composés peuvent être expliqués en se basant sur les défauts réticulaires.

Es werden die grundlegenden chemischen und physikalischen Eigenschaften von Hydriden der Übergangsmetalle besprochen, wobei grösserer Wert auf Hydridphasen als auf feste Lösungen von Wasserstoff in Metallen gelegt wird. Der gegebene Überblick enthält Erörterungen über die Phases in Metall-Wasserstoff-Systemen, über ihre Struktur, über Zusammenhänge zwischen Druck, Konzentration und Temperatur, über thermodynamische Eigenschaften und über elektrische und magnetische Eigenschaften.

Der Aufbau der Hydride der Übergangsmetalle wird betrachtet. Dabei werden Hinweise dafür angegeben, dass es sich um definierte chemische Verbindungen (und nicht um feste Lösungen) mit dem Charakter ähnlich Ionenkristallen handelt. Die grossen Abweichungen dieser Verbindungen von der stöchiometrischen Zusammensetzung können durch Gitterfehler erklärt werden.

TABLE OF CONTENTS

1. Introduction

Since hydrogen is theoretically the most effective thermal neutron moderator, it becomes highly desirable to find materials which contain a high concentration of hydrogen atoms per unit volume. This objective can be accomplished most efficiently through the utilization of metallic hydrides. Therefore, the hydrides of the transition metals have been the subject of a great deal of study since the advent of nuclear power. Table 1 shows the number of hydrogen

TABLE 1

N_H Values for hydrogen containing compounds

Compound	$N_H \times 10^{-22}$ (atoms/cc)
Liq. H_2 ($-253°$ C)	4.2
Liq. CH_4 ($-164°$ C)	6.3
H_2O	6.7
LiH	5.9
ZrH_2	7.2
UH_3	8.2
TiH_2	9.5

atoms per cubic centimeter, N_H, for some more familiar hydrides as compared with water, liquid hydrogen, and a saturated organic molecule.

$$N_H = \frac{\text{(Density of Hydride)}}{\text{M.W. of hydride}} \text{ (No. of H atoms per molecule)} \times 6.02 \times 10^{23}.$$

The N_H values shown for the hydrides and water are at room temperature. Although N_H for the transition metal hydrides are not significantly greater than for liquid hydrogen or water, the value of the hydrides as nuclear moderators lies in their stability at higher temperatures. Whereas water and organic molecules vaporize (or decompose) at higher temperatures, the N_H values for the transition metal hydrides do not change appreciably until their dissociation temperature (usually several hundred degrees) is reached. From the standpoint of a moderating material, a useful hydride should have a high hydrogen to metal ratio, high density, low molecular weight, and a low dissociation pressure.

It is the purpose of this paper first to review

the basic chemical and physical properties of transition metal hydrides (and related hydrides of interest) which could lead to an elucidation of the fundamental nature of these materials. This discussion will cover the phases present in metal-hydrogen systems, their crystal structures, pressure-composition-temperature relations, thermodynamic properties of hydrides, and, where available, their electrical and magnetic properties. Secondly, some ideas on the bonding and nature of these substances will be presented, and correlated with experimentally determined properties.

In 1947, Smith [1] presented a rather complete review on occlusion of hydrogen by metals (predominantly the transition metals), and in 1952, Hurd [2] published a book on the chemistry of hydrides in which some space was devoted to a review of hydrides of the transition metals. Therefore, in this paper, emphasis will be placed on work performed subsequent to these dates, and also on the hydride phases rather than dilute solutions of hydrogen in metals.

2. Properties of transition metal hydrides

2.1. HYDRIDES OF THE GROUP IV A METALS

Titanium Hydride

Phase Relations: A detailed study of the pressure-composition-temperature relations in the titanium-hydrogen system was first carried out by McQuillan [3]. The phase diagram he obtained from this work is essentially the one shown in Fig. 1 with the dotted line representing McQuillan's extrapolations of his measured data (full line). Presumably, as hydrogen is dissolved in titanium metal, the α to β transformation temperature is lowered giving rise to the two phase region ($\alpha + \beta$) observed at the lower hydrogen compositions (< 0.7 H/Ti) in the pressure-composition isotherms. Unfortunately, there have been no X-ray studies of this system at high temperatures and low hydrogen contents to establish if the second phase is actually the high temperature body centered cubic β modification of titanium metal. At higher hydrogen contents, a γ or hydride phase is formed which
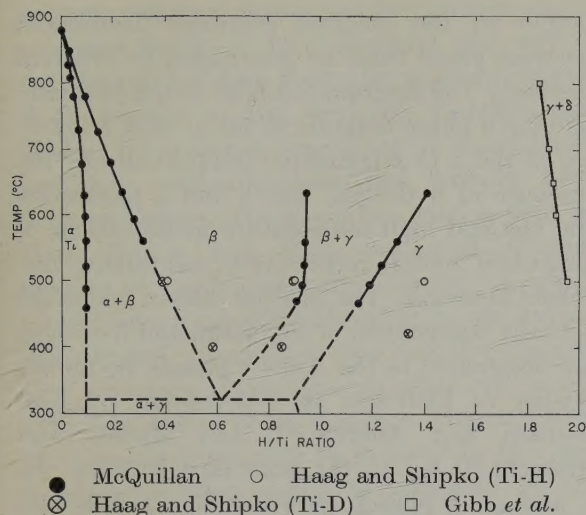
Fig. 1. Titanium-hydrogen phase diagram.

approaches the stoichiometric formula TiH_2.

Fig. 1 also includes the points obtained from the subsequent *P-C-T* study of this system by Haag and Shipko [4]). These authors also studied the titanium-deuterium and titanium-tritium systems and observed no isotopic effect with respect to either dissociation pressures or phase boundaries. Except for the boundary between the $\beta + \gamma$ phases and the γ phase, the agreement with McQuillan's work seems to be quite good. Gibb, McSharry and Bragdon [5]) report an additional phase at close to stoichiometric TiH_2 from a study of pressure-composition isotherms. Although it is shown as δ in fig. 1, the existence of this phase is questionable since the authors calculated their compositions on the basis of their starting material being stoichiometric TiH_2, and no actual experimental points were obtained on the two phase plateau regions of the isotherm.

Thermodynamic Properties: The heat of formation of the nonstoichiometric hydride present in the two-phase region at 400–500° C ($TiH_{1.4}$) is −22.6 kcal/mole as calculated from the data of Haag and Shipko.

The dissociation pressure of the hydride to β-Ti and hydrogen is given by the relation †

† Except where explicitly given this form of relation will be used and the values of A and B given for the phase under discussion.

$$\log P_{10} \text{ (mm)} = \frac{-A}{T} + B$$

where $A = 8630$ and $B = 12.43$. These values were calculated from the data of McQuillan.

Crystal Structure: An X-ray structure determination of the hydride phase by Hägg [6]) revealed that the titanium atoms were in a face-centered cubic structure with a lattice parameter ranging from 4.40 to 4.46 Å with increasing hydrogen content. This structure was confirmed in an X-ray and neutron diffraction study by Sidhu, Heston and Zauberis [7]). The neutron diffraction results on titanium deuteride showed that the hydrogen (or deuterium) atoms occupied the tetrahedral positions in the face-centered cubic titanium lattice to form a fluorite structure. The lattice parameter of $TiD_{1.971}$ was 4.440 Å. As the composition approached TiD_2, the cubic unit cell deformed to a face-centered tetragonal cell. A further study of this deformation was carried out by Yakel [8]) who demonstrated the occurrence of a second order transformation below 310° K. At 315° K both $TiD_{1.98}$ and $TiH_{1.99}$ are cubic with lattice parameters of 4.440 Å and 4.454 Å, respectively. As the temperature is decreased below 310° K, there is a continuous expansion of the crystal in two directions (a and b axes) and a contraction in the third (c axis) to form a face-centered tetragonal structure. The minimum c/a ratio reached at 79° K was 0.945.

A high temperature high pressure X-ray study of titanium hydride (at hydrogen contents close to TiH_2) by Goon and Malgiolio [9]) revealed a maximum in the lattice parameter of the f.c.c. structure with temperature at constant hydrogen pressure. The temperature at which the maximum occurred varied with hydrogen pressure (e.g., at 100 psi, 280 psi, and 435 psi, the temperatures at which the maximum occurred were about 350°, 450° and 500° C, respectively). The initial increase in lattice parameter appears to be normal thermal expansion. Goon proposes that the subsequent contraction is due to the filling of octahedral sites in the f.c.c. lattice with a corresponding formation of vacant tetrahedral sites. Wolfarth [10]) has explained

maxima in magnetic susceptibility isotherms obtained by Trzebiatowski and Stalinski [11]) as due to antiferromagnetism. However, Wilkinson and Shull [12]) at Oak Ridge National Laboratory found no evidence of antiferromagnetic ordering in a neutron diffraction study of titanium hydride. The maxima in magnetic susceptibility isotherms may be associated with the maxima in lattice parameter observed by Goon. There is an obvious necessity for further work to explain both the tetragonality at lower temperatures and the maxima in lattice parameter and magnetic susceptibility at higher temperatures.

Zirconium Hydride

At the present time, the hydride of most interest from the nuclear reactor standpoint is zirconium hydride because of its relatively high value of N_H, high temperature stability, and the low capture cross section (0.18 barns) of zirconium. For these reasons, the zirconium hydrogen system has been studied more than any other metal-hydrogen system in recent years.

Phase Relations: A composite phase diagram for this system is shown in fig. 2. All
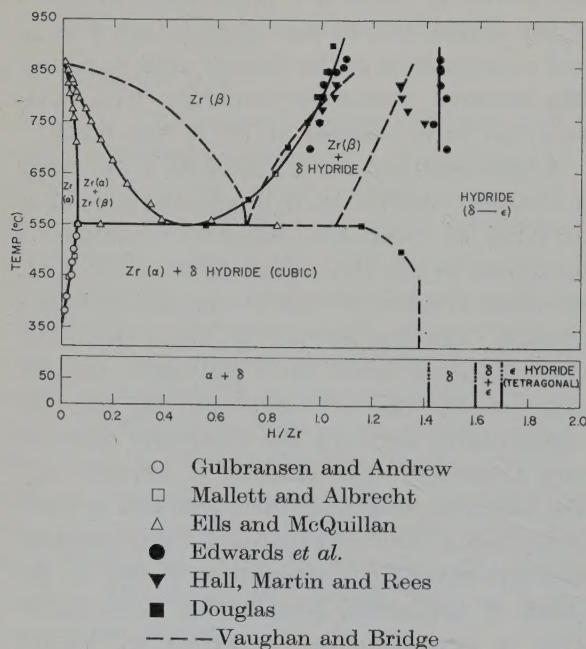
Fig. 2.   Zirconium-hydrogen phase diagram.

points on the diagram represent boundaries between phase fields as determined by different methods. The diagram is similar to the titanium-hydrogen phase diagram in form, with a lowering of the α to β transition temperature by the presence of hydrogen. The α and β phases are the low and high temperature modifications of zirconium metal, respectively, containing dissolved hydrogen. The hydride phases, which are actually compounds of zirconium and hydrogen are designated as the δ and ε phases. Solubility studies of hydrogen in α-zirconium by Gulbransen and Andrew [13]), and Mallett and Albrecht [14]) led to the boundary between the α and $\alpha + \delta$ phases shown in fig. 2. Ells and McQuillan [15]) measured equilibrium pressures from 500° to 950° C for hydrogen contents up to $ZrH_{0.8}$, thus obtaining the limits of the two phase ($\alpha + \beta$) region. A high temperature X-ray phase study of this system by Vaughan and Bridge [16]) gave very poor agreement for the boundary between the two phase ($\alpha + \beta$) region and the one phase β region as shown by the dashed curve in fig. 2. The large discrepancy between the two investigations is probably due to the difference in experimental methods. The equilibrium pressure study is inherently more precise since this method determines the actual points on the phase boundary from breaks in the isotherms. On the other hand, the X-ray method depends on an estimation of the boundary between two regions containing points representing the phases present. In addition, a phase present in low concentration cannot be detected by X-ray diffraction analysis.

The points representing the boundary between the β and two phase $\beta + \delta$ regions have been obtained from pressure-composition-temperature measurements by Edwards, Levesque and Cubicciotti [17]), and Hall, Martin and Rees [18]), and also from a heat content study by Douglas [19]) as well as from the work of Ells and McQuillan, and Vaughan and Bridge. The results of all five investigations give very good agreement with each other for this boundary. However, there was considerable disagreement between three different determinations of the boundary

between the $\beta + \delta$ region and the hydride region as shown in fig. 2. It is doubtful that any of the three sets of data shown are entirely correct. With respect to the work of Vaughan and Bridge, the inherent inaccuracy of X-ray phase boundary determinations has already been discussed above. The zirconium sample used by Hall, Martin and Rees contained a large amount of oxygen impurity (0.4 wt %), which should have a considerable effect on the uptake of hydrogen. In addition, the negative slope of this boundary is opposite to what one would expect in such a phase diagram. The isotherms of Edwards et al. may be in error in the high hydrogen content region as indicated by the rapid decrease in slope of their $\log P$ versus $1/T$ isochores [20] at H/Zr values above 1.6. It has been pointed out by Gilbert [21] that this is thermodynamically improbable. A current investigation [22] of this system indicates that the $(\beta + \delta)$/hydride boundary has a positive slope and occurs at lower hydrogen contents than the boundary given by Edwards et al.

The X-ray data of Vaughan and Bridge indicate that the $(\alpha + \delta)/\delta$ boundary is vertical below 450° C. Further evidence for the position of this boundary is given by the heat content study of Douglas. However, since it is sometimes difficult to reach equilibrium at lower temperatures, there may be some question as to the accuracy of this boundary.

The two phase $\delta + \varepsilon$ region has been observed at room temperature by several investigators. An X-ray study by Gulbransen and Andrew [23] indicated that this region extended from H/Zr = 1.55 to about 1.62. Trzebiatowski and Stalinski's X-ray work [24] gave an approximate range for the $\delta + \varepsilon$ region of H/Zr = 1.63 to 1.73. The range of this two phase region can be also determined from thermoelectric power measurements on zirconium hydride carried out by Bickel [25] at this laboratory. From these data, the two-phase region was found to exist between H/Zr = 1.57 and 1.73. An average of these three investigations indicates that the $\delta + \varepsilon$ region lies approximately between H/Zr = 1.6 to 1.7 as shown in fig. 2. There is no evidence for the

existence of this two phase region at higher temperatures. The pressure-composition isotherms of Edwards et al.[17], and a more recent P-C-T study [22] indicate no plateaus or breaks in this composition range as would be required by a two phase region. Therefore, the $\delta + \varepsilon$ two phase region must become narrower with increasing temperature until it disappears entirely at higher temperatures. Whitwham et al.[26] believe that the ε phase is formed by a pseudo-martensitic transformation from the δ phase.

There is a strong possibility that the two phase $\delta + \varepsilon$ region in the Zr-H system may actually not exist. Edwards and Levesque [27], in a study of the Zr-H-O system, observed that the two phase $\delta + \varepsilon$ region, present below about 15 at % oxygen, narrowed with decreasing oxygen content. They believed that this two phase region is still present in the binary Zr-H system. However, since their conclusion was based on extrapolated data, the possibility that the two phase $\delta + \varepsilon$ region in the binary Zr-H system may be due to oxygen impurity should be considered.

Crystal Structures: There has been some confusion as to the structures of the phases present at high hydrogen compositions in the zirconium hydrogen system. Hägg [6] reported the five phases shown in table 2. The β and γ

TABLE 2

Zirconium-hydrogen phases as reported by Hägg [6]

Composition (H/Zr)	Designation	Structure	Lattice Parameters
0–0.05	α	h.c.p.	$a = 3.25$; $c = 5.17$
0.25	β	f.c.c.	$a = 4.66$
0.50	γ	h.c.p.	$a = 3.55$; $c = 5.45$
1.0	δ	f.c.c. (fluorite)	$a = 4.78$
2	ε	f.c.t.	$a = 4.96$; $c = 4.44$

phases reported by Hägg have not been observed by subsequent investigators. They are probably non-equilibrium phases; although the f.c.c. β phase may really be δ phase hydride, with the reported composition $ZrH_{0.25}$ being in

error. The β phase shown in fig. 2 is actually the high temperature b.c.c. form of Zr, with the lattice parameter increasing [16]) from 3.51 to 3.68 Å at $ZrH_{0.82}$.

Gulbransen and Andrew [23]) have confirmed the δ and ε phases of Hägg. In addition, they observed a new phase designated as γ', which had f.c.t. structure with $c/a = 1.08$ ($a = 4.61$ Å, $c = 4.975$ Å), and co-existed with the α and δ phases. From the work of Vaughan and Bridge, and the P-C-T data at high composition, it appears that there is a single hydride phase at high temperatures; a face-centered tetragonal structure with continuously varying c/a ratio. The hydride at the (β + hydride)/hydride boundary (i.e., the hydride co-existing with β-Zr) has a c/a ratio greater than one. As the hydrogen content increases, the c/a ratio decreases becoming one (f.c.c. structure) at about $H/Zr = 1.5$. Further addition of hydrogen causes the c/a ratio to become less than one. Gulbransen's γ' phase, therefore, may be the high temperature hydride which co-exists with β-Zr at high temperatures and is metastable at room temperature.

On the basis of three experimental points (at $H/Zr = 1.22$, 1.50, 1.86), Vaughan and

Fig. 3.   Variation in c/a ratio with hydrogen content in ε-zirconium hydride.

Bridge show a linear decrease in c/a ratio with hydrogen content over the whole hydride range at room temperature. Actually, the range over which the c/a ratio changes is much narrower. Their last two points completely bypass the two phase ($\delta + \varepsilon$) region shown in Fig. 2. Also, the point at $H/Zr = 1.22$ is in the two phase ($\alpha + \delta$) region. Trzebiatowski and Stalinski [24]) have shown that there is a decrease in c/a ratio with hydrogen content at room temperature in the single phase ε region as shown in fig. 3. This decrease was also observed by Sofina and co-workers [28]).

An X-ray and neutron diffraction study [29]) of ZrH_2 confirmed a f.c.t. structure for the zirconium atoms with the hydrogen atoms located in the tetrahedral positions to give a slightly tetragonal "fluorite" structure. The lattice parameters were $a = 4.978$ Å and $c = 4.449$ Å. Yakel [8]) and Goon [9]) agreed with these values and also observed an increasing c/a ratio with temperature similar to that in titanium hydride.

Thermodynamic Properties: From the dissociation pressure data in the two phase $\alpha + \delta$ region of Gulbransen and Andrew [23]), the heat of formation of δ-zirconium hydride from hydrogen saturated α-Zr is calculated to be -48.3 kcal per mole of H_2 absorbed in the temperature range 400°–550° C. According to fig. 2, the composition of the δ hydride phase formed at temperatures below 450° C is $ZrH_{1.38}$. At 400° C, the reaction can be written:

$$ZrH_{0.02}(\alpha) + 0.68\ H_2 \rightarrow ZrH_{1.38}(\delta).$$

Using the value of -27.6 kcal/mole H_2 for the heat of solution of hydrogen in α-Zr given by Douglas [19]), and re-calculating per mole of hydride, the heat of formation, $\Delta H°_{400°C}$, of δ zirconium hydride is -33.1 kcal/mole hydride ($ZrH_{1.38}$) at 400° C. From heat content measurements, Douglas gives a value of -42.7 kcal/mole H_2 for the conversion of hydrogen saturated α-Zr to δ zirconium hydride at 550° C. This is 5.6 kcal less than the value derived from Gulbransen's [23]) data.

Assuming the composition of $ZrH_{1.5}$, and an
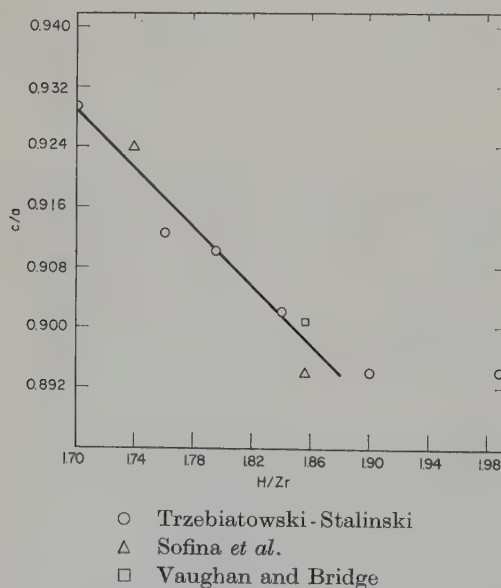
approximate value of 2.25 cal/degree C for the heat capacity of the hydride, Gulbransen and Andrew [23]) give the following relation for the free energy of formation of the hydride:

$$\Delta F^\circ = -34\,930 - 2.25\,T\ln T + 43.88\,T.$$

For the heat of formation of δ-hydride from hydrogen saturated β-zirconium, Edwards [20]) obtains a value of -49.6 kcal/mole H_2 from dissociation pressure measurements in the range $600°$–$900°$ C. Douglas' value is -50.7 kcal/mole H_2 at $550°$ C.

For the two phase $\beta + \delta$ pressure plateau, the data of Edwards for dissociation pressure give values of $+10\,850$ and 12.22 for A and B, respectively. Hall, Martin and Rees [18]) measurements yield values [30]) of $+10\,300$ and 11.75. For the two phase $\alpha + \delta$ region, the values of A and B are $+10\,540$ and 11.80, respectively, as calculated from Gulbransen's data.

Hafnium Hydride

The phases present in the hafnium-hydrogen system at room temperature were determined in an X-ray study by Sidhu and McGuire [31]). The first hydride phase appeared at a very low concentration of hydrogen. It was a slightly deformed f.c.c. hydride which co-existed with α-hafnium metal up to a hydrogen content ratio of about H/Hf = 1.6. Between H/Hf 1.6 and 1.8, the cubic hydride was no longer deformed and existed as a single phase. At about an H/Hf ratio of 1.8, a face centered tetragonal hydride was formed which co-existed with the cubic phase up to an H/Hf ratio of about 1.86. From an H/Hf ratio of 1.86 to 2, f.c.t. hydride exists as a single phase, the c/a ratio decreasing [32]) with increasing hydrogen content as in ε zirconium hydride. The lattice parameters of the f.c. tetragonal HfH_2 are [33]) $a_0 = 4.919$ and $c_0 = 4.363$, and that of the f.c. cubic phase $a_0 = 4.708$ Å. A neutron diffraction study [7]) of the corresponding hafnium deuterides, revealed that the deuterium (or hydrogen) existed in the tetrahedral positions of a fluorite-type lattice similar to the structure of zirconium hydride.
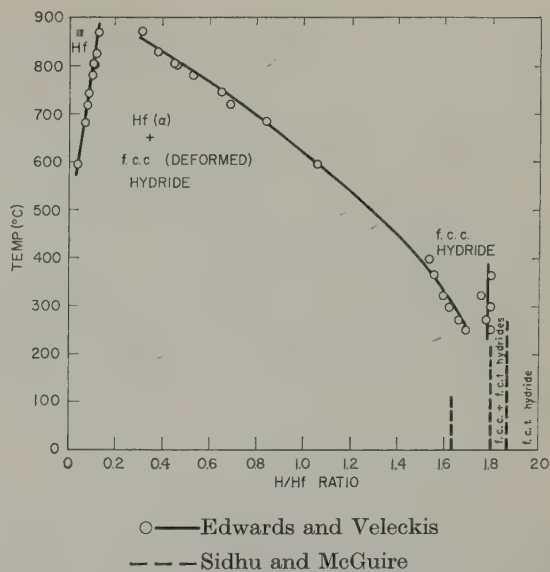
Fig. 4.   Hafnium-hydrogen phase diagram.

A pressure-composition-temperature study of the hafnium-hydrogen system has been carried out by Edwards and Veleckis [34]). The phase diagram derived therefrom is shown in fig. 4 along with the phases obtained from X-ray studies [31]) (represented by the dotted line). The two phase region (α-Hf metal + f.c.c. hydride) shows up clearly as pressure plateaus in the pressure-composition isotherms, while the two-phase hydride region (f.c.c. + f.c.t.) appears as a break in the increasing pressure high composition portions of the isotherms. The phase boundaries obtained from the *P-C-T* studies agree fairly well with those from the X-ray study. It has been observed by Sidhu *et al.*[7]) that the position of the (α-Hf + f.c.c.)/f.c.c. phase boundary is quite sensitive to the conditions under which the samples were prepared. This may explain the slight discrepancy in the position of this boundary as determined by the two different investigations.

From the *P-C-T* studies the dissociation pressure of the cubic hydride can be expressed by the usual relation if $A = 7250$ and $B = 8.65$. From these data the heat of formation of the nonstoichiometric cubic hydride from hydrogen saturated α-Hf is calculated as -33.2 kcal/mole hydrogen.

The effect of pile-irradiation on the hafnium hydrides was investigated by Sidhu, Campos and Zauberis [35]). Samples of both the cubic and tetragonal hydrides were irradiated for almost a month in a heavy water reactor under a thermal neutron flux of 4.5×10^{12}, an epicadmium neutron flux of 3×10^{11} and a gamma-ray flux of 1600 r/sec. The samples were studied by X-rays about a year after removal from the reactor. No change in structure of hydrogen composition was observed indicating that the hydrides undergo no permanent changes under reactor radiation.

2.2. RARE EARTH HYDRIDES

Except for ytterbium and europium, the rare earth metals appear to form two hydrides corresponding to the stoichiometric formulas MH_2 and MH_3. Pressure-composition-temperature relations of the hydrides of the first four metals in the rare earth series were studied by Mulford and Holley [36]), and an X-ray and neutron diffraction investigation of the same four hydrides plus samarium hydride was made by Holley et al.[37]). Hydrogen has a limited solubility in these rare earth metals (La, Ce, Pr and Nd). Definite dihydrides are formed which co-exist with the corresponding hydrogen saturated metal. The dihydrides actually have hydrogen contents slightly less than the stoichiometric value of two. They have a fluorite structure, with the lattice parameters shown in table 3. Further addition of hydrogen yields a continuous solid solution which approaches the stoichiometric formula HM_3. The neutron diffraction measurements indicate that the additional hydrogen enters the octahedral sites of the fluorite structure, with contraction of

TABLE 3
Lattice constants of rare earth dihydrides

Hydride	Lattice parameter (Å)
LaH_2	5.667 ± 0.001
CeH_2	5.581 ± 0.001
PrH_2	5.517 ± 0.001
NdH_2	5.470 ± 0.001
SmH_2	5.376 ± 0.003

the lattice. Korst and Warf [38]) observed that the lattices of these hydrides began to contract at about $MH_{1.8}$, indicating the occupation of octahedral sites before all the tetrahedral sites were filled.

From the pressure-composition-temperature data of Mulford, the dissociation pressures of the hydrides and their heats of formation from the hydrogen saturated metal, Δ_H, can be calculated in the temperature range $500°$–$800°$ C. These are shown in table 4 along with the corresponding values obtained from P-C-T measurements by Korst. The values given for A and B represent the terms in the dissociation pressure equation given above. Except for the case of cerium hydride, the agreement between the two different P-C-T investigations is reasonably good. The value given by Korst is probably the more accurate one, since there is no apparent reason for the Δ_H of cerium hydride to differ so much from the other three hydrides.

Although the stoichiometric composition MH_3 was not attained by either Mulford or Korst, Dialer and Rothe [39]) claimed the preparation of a cerium hydride corresponding to the exact stoichiometric composition $CeH_{3.000 \pm 0.002}$. Such accuracy is probably not warranted [38]) in view of the experimental procedures used. More

TABLE 4
Dissociation pressures and heats of formation of rare earth hydrides

Hydride	A		B		Δ_H (kcal/mole H_2)	
	Mulford	Korst	Mulford	Korst	Mulford	Korst
LaH_2	10 860	10 850	10.76	10.64	-49.7	-49.6
CeH_2	7 420	10 760	7.71	10.63	-33.9	-49.2
PrH_2	10 450	10 870	10.23	10.53	-47.8	-49.7
NdH_2	9 800	11 030	9.37	10.48	-44.8	-50.5

recently, Mikheeva and Kost [40] report a cerium hydride with a hydride content up to $CeH_{3.16}$.

A study [41] of the gadolinium-hydrogen system revealed the formation of two hydrides approaching the stoichiometric formulas MH_2 and MH_3. The dihydride has a fluorite structure (similar to the hydrides discussed above) with a lattice parameter of 5.303 Å. The trihydride, however, has a structure different from the tribydrides of the rare earths previously discussed. Rather than a cubic structure derived from GdH_2 by filling octahedral sites, the trihydride of gadolinium has a hexagonal structure with lattice parameters $a_0 = 3.73$ and $c_0 = 6.71$ Å.

From P-C-T studies, the heat of formation of GdH_2 from hydrogen saturated gadolinium metal is -46.9 kcal/mole in the temperature range 600–800° C, and the dissociation pressure of the dihydride is given if $A = 10\,250$ and $B = 9.72$. The trihydride has a much lower thermal stability than the dihydride, and probably dissociates (H_2 pressure reaches 1 atm) at about 400° C.

The di- and tri-hydrides of erbium have also been prepared [42], they have fluorite and hexagonal structures, respectively. The dissociation pressure of the dihydride, ErH_2, is given if $A = 11\,780$ and $B = 10.91$ and the heat of formation is about -54 kcal/mole.

The hydrides of ytterbium and europium differ considerably from the hydrides of the other rare earth metals. An X-ray diffraction study [43] showed that these metals formed hydrides approaching the stoichiometric formula MH_2, having orthorhombic structures isomorphous with the alkaline earth metal hydrides. The lattice parameters of the hydrides were $a = 5.871$, $b = 3.561$, $c = 6.763$ Å for ytterbium deuteride, and $a = 6.21$, $b = 3.77$, $c = 7.16$ for europium deuteride. The reason for the different properties of these two hydrides lies in the electronic configuration of the metals. In ytterbium, the 4f shell is completely filled thus stabilizing these electrons and permitting only the two 6s electrons to engage in bonding. Similarly, in europium all seven 4f orbitals

contain one electron (according to Hund's rule of maximum multiplicity) resulting in a stabilized electron configuration. These two elements, therefore, form stable divalent compounds since their electron configuration is similar to the alkaline earth elements.

Electrical resistivity measurements [44–46] of some rare earth hydrides indicate that they may be semiconductors since their resistivities fall in the range 0.1–10^7 ohm cm, and they exhibit a negative temperature coefficient of resistivity.

2.3. HYDRIDES OF THE ACTINIDE SERIES ELEMENTS

The actinide series hydrides do not resemble each other as do the hydrides of the two series discussed above. The three metals which are of most interest to nuclear reactor technology, U, Th and Pu, form hydrides of different hydrogen to metal ratios and structures. The hydrides will be discussed in order of atomic number.

Actinium Hydride

An actinium hydride having the stoichiometric formula AcH_2 was prepared by Farr et al.[47]. X-ray structure studies indicated that the actinium atoms were arranged in a face centered cubic structure with a lattice parameter of 5.670 Å. Presumably, the hydrogen atoms are situated in the tetrahedral positions to form a fluorite structure.

Thorium Hydride

A pressure-composition-temperature study of the thorium-hydrogen system by Nottorf [48] revealed that thorium reacted readily with hydrogen to form two definite hydrides, one approaching a stoichiometric composition ThH_2 and the other approaching the H/Th ratio of 3.75. The dissociation pressure of the lower hydride corresponds to $A = 7700$ and $B = 9.54$; that of the higher hydride to $A = 4220$ and $B = 9.50$. The heats of formation of hydrogen deficient ThH_2 from hydrogen saturated thorium metal was about -35.2 kcal/mole H_2; and the heat of formation of hydrogen deficient $ThH_{3.75}$ from non-stoichiometric ThH_2 was -19.3

kcal/mole H_2. A subsequent P-C-T study of the dihydride by Mallett and Campbell [49]) gave $A = 7500$ and $B = 9.35$ for the dissociation pressure of the nonstoichiometric di-hydride, and -34.3 kcal/mole H_2 for its heat of formation. These values are in good agreement with those of Nottorf. It should be pointed out, however, that in both investigations the pressure of the two-phase regions $(Th + ThH_2)$ and $(ThH_2 + ThH_{3.75})$ were not constant as required by the phase rule, but increased slightly with increasing hydrogen content of the system, thus leading to sloping plateau regions of the isotherms. Since this is due to either impurity in the samples or thermal gradients [50]) along the sample during measurements, the values given may be somewhat in error.

From X-ray and neutron diffraction studies [29]), the crystal structure of ThH_2 was found to be isomorphous with zirconium hydride having a face centered tetragonal structure with $a_0 = 5.80$ Å and $c_0 = 5.03$ Å (or b.c.t. with $a_0 = 4.10$ Å). The hydrogen atoms are situated in the tetrahedral positions. The structure of the higher hydride was determined by Zachariasen [51]) from X-rays to be body centered cubic with a lattice parameter of 9.11 ± 0.02 Å. The unit cell contains 16 thorium atoms and 60 hydrogen atoms which definitely establishes the chemical formula Th_4H_{15} for the stoichiometric hydride.

Protactinium Hydride

A protactinium hydride was prepared by Sellers et al.[52]) by the reaction of protactinium metal with hydrogen at 250°. The hydride is cubic and isostructural with uranium hydride (see below) having a lattice parameter of 6.648 Å.

Uranium Hydride

The first comprehensive investigation of the uranium-hydrogen system was carried out by Spedding and co-workers [53]). Uranium was found to react readily with hydrogen to form a single pyrophoric hydride with the stoichiometric formula, UH_3. From pressure-composition-temperature studies the dissociation pres-
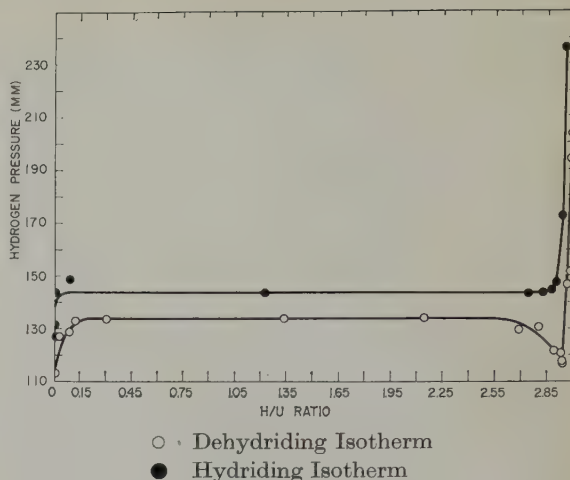
Fig. 5. Pressure-composition isotherms for the uranium-hydrogen system at 357° C (Spedding et al.[53]).

○ · Dehydriding Isotherm
● Hydriding Isotherm

sure corresponds to $A = 4500$ and $B = 9.28$ and the heat of formation was calculated to be -30.8 kcal/mole hydride. In studying the 357° C pressure-composition isotherm of this system, Spedding observed that the equilibrium pressures on hydriding were higher than those obtained on dehydriding. This hysteresis effect has also been observed in other metal-hydrogen systems [1]). As shown in fig. 5, the dehydriding isotherm also had a dip in the high composition end of the isotherm which could be reproduced in subsequent experimental runs. No explanation for these effects are given.

A dissociation pressure study of UH_3 by Flotow and Abraham [54]), in the temperature range 300°–420° C, yielded the following dissociation pressure equation:

$$\log_{10}P \text{ (mm)} = -\frac{6270.1}{T} - 6.0146 \log_{10}T + 28.9235,$$

and a heat of formation equal to -30.5 kcal/mole hydride. A high pressure dissociation study [55]) (up to 60 atm of H_2) gave the usual simpler expression for the dissociation pressure in the range 450°–650° C with $A = 4410$ and $B = 9.14$ from which a heat of formation of -30.3 kcal/mole hydride was obtained. This value is in good agreement with the values obtained by Spedding and Flotow and Abraham, and also with a calorimetrically dtermined [56]) value of -30.35 kcal/mole hydride at 25° C.

Therefore, it can be seen that the heat of formation of UH_3 remains reasonably constant over the wide temperature range 0–650° C.

From an X-ray diffraction study [57], the uranium atoms in the UH_3 structure were found to form the cubic β-tungsten structure with 8 U atoms per unit cell at $(0, 0, 0)$, $(\frac{1}{2}, \frac{1}{2}, \frac{1}{2})$, $(\frac{1}{4}, \frac{1}{2}, 0)$, $(0, \frac{1}{4}, \frac{1}{2})$, $(\frac{1}{2}, 0, \frac{1}{4})$, $(\frac{3}{4}, \frac{1}{2}, 0)$, $(0, \frac{3}{4}, \frac{1}{2})$, and $(\frac{1}{2}, 0, \frac{3}{4})$. The lattice parameter of uranium hydride is 6.645 Å. The positions of the hydrogen atoms in the UH_3 lattice were determined by neutron diffraction [58]. They are situated in the center of deformed tetrahedra equidistant from four U neighbors, the U-H distance being 2.32 Å. Each uranium atom is surrounded by twelve hydrogen atoms.

When uranium hydride is prepared at low temperatures, a new phase (α) appears [59], the lower the temperature the greater the proportion of α-phase in the β-phase (β-phase being the phase described above). The α-phase is stable at 100° C but converts to β-phase at 250° C. This low temperature phase can also be prepared by an electrolytic method [60]. The structure of this phase is body centered cubic with two uranium atoms per unit cell at $(0, 0, 0)$ and $(\frac{1}{2}, \frac{1}{2}, \frac{1}{2})$ and six hydrogen atoms at $\pm (\frac{1}{4}, 0, \frac{1}{2})$, $\pm (\frac{1}{2}, \frac{1}{4}, 0)$ and $\pm (0, \frac{1}{2}, \frac{1}{4})$, and a lattice parameter of 4.155 ± 0.05 Å.

Magnetic susceptibility measurements by several investigators [61–63] showed that uranium hydride becomes ferromagnetic at about 173° K. Some rough electrical conductivity measurements [53] on uranium hydride indicated that its resistivity was of the same order of magnitude as uranium metal.

Neptunium Hydride

Neptunium metal is reported [64] to react rapidly with hydrogen at 50° C to form a hydride having the composition $NpH_{3.6–3.8}$. If this hydrogen to metal ratio is correct, it may be similar to the higher thorium hydride.

Plutonium Hydrides

Plutonium metal forms two hydrides having the stoichiometric formulas PuH_2 and PuH_3. Pressure-composition-temperature studies [65] yielded $A = 8165$ and $B = 10.01$ for the dissociation pressure of the dihydride, and a corresponding heat of formation from hydrogen saturated plutonium metal of -37.4 kcal/mole H_2. The dihydride has a fluorite structure similar to the rare earth hydrides with a lattice parameter of 5.359 Å.

Mulford and Sturdy [65] observed that PuH_2 will dissolve hydrogen in the octahedral interstices of its lattice with a corresponding decrease in lattice parameter. At about $PuH_{2.7}$ (the actual H/Pu ratio varies with temperature) a hexagonal phase is formed which seems to coexist with the cubic PuH_2 up to a hydrogen content of about $PuH_{2.9}$ at which composition only the hexagonal phase is present. This behavior is analogous to that of gadolinium hydride except that the boundaries of the two phase (cubic hydride + hexagonal hydride) region are not as sharply defined. The lattice parameters of the hexagonal tri-hydride are $a_0 = 3.78$ and $c_0 = 6.76$ Å. An X-ray study of $PuH_{2.7}$ by McDonald and Fardon [67] gave values for the lattice parameter of the hexagonal hydride which were identical with those of Mulford. Their value for the cubic hydride was 5.34 Å which was the value given by Mulford at the composition of $PuH_{2.5}$.

Americium Hydride

Americium metal reacts [68] violently with hydrogen at 50° C to yield a hydride of the formula $AmH_{2.7 \pm 0.3}$. A lower hydride, AmH_2 has also been reported [69].

2.4. HYDRIDES OF THE GROUP V A METALS

In general, the Group V A metals form hydrides approaching the stoichiometric formula MH. The change from metal to hydride seems to be a continuous one with no sharp change in structure. Two phase regions, if they exist, seem to occur at much lower temperatures than they do for hydrides of the Groups III A and IV A metals.

Vanadium Hydride

The hydride having the highest hydrogen to vanadium ratio was $VH_{0.94}$ prepared by Trzeciak et al.[70] from iodide process vanadium. X-ray diffraction showed the hydride to be body centered tetragonal with $a_0 = 3.02$ Å and $c_0 = 3.36$ Å. Vanadium metal has a b.c.c. structure [71] with $a_0 = 3.028$ Å. A neutron diffraction study [72] of $VD_{0.75}$ gave a b.c.c. structure for the hydride with $a_0 = 3.148$ Å. The positions of the deuterium atoms could not be determined above 207° K. Below this temperature, the deuterium atoms ordered themselves into a primitive cubic lattice with $a_0 = 6.30$ Å, twice the lattice parameter of the vanadium cell in the hydride. Therefore, it appears that the b.c.c. vanadium lattice expands with addition of hydrogen, eventually distorting to a tetragonal lattice at high hydrogen contents.

Niobium Hydride

Because of its high temperature properties and relatively low cross section, niobium has recently become of interest to the nuclear reactor field. Pressure-composition-temperature and X-ray studies on the niobium-hydrogen system have been carried out by Albrecht et al.[73]). The P-C-T studies show that there is continuous solubility of hydrogen in niobium above 300° C. Below this temperature, however, a hydride phase is formed. Albrecht showed that this hydride or β-phase is body centered cubic with $a_0 = 3.42$ Å. The α-phase is also b.c.c. with a lattice parameter [71]) of 3.301 Å. At room temperature the two phases, hydrogen saturated α-Nb ($a_0 = 3.308$ Å) and β-niobium hydride, co-exist between the approximate compositions 0.09 to 0.7 H/Nb. Above H/Nb = 0.7, only β-phase is present, its lattice parameter increasing [74]) to 3.447 Å at $NbH_{0.83}$.

According to Brauer and Hermann [75]), the β-phase is actually a deformed b.c.c. structure and can better be considered as face centered orthorhombic with $a_0 = 4.84$, $b_0 = 4.90$, and $c_0 = 3.45$ Å at $NbH_{0.89}$.

The heat of solution of hydrogen in niobium increases from 16.1 kcal/mole at H/Nb = 0.01 to 23.3 kcal/mole at H/Nb = 0.70.

Tantalum Hydride

Horn and Zeigler [76]) found hydrogen to be continuously soluble in tantalum metal (b.c.c.[71], $a_0 = 3.303$) up to H/Ta = 0.49 with the lattice parameter increasing to 3.399 Å. Brauer and Hermann [75]) report a solubility of H/Ta = 0.2 with the lattice parameter increasing to 3.34 Å. The β-hydride forms at this point. The solubility reported by Stalinski [77]) was H/Ta = 0.37, the lattice parameter of the metal increasing to 3.363 Å. The reason for this large variation in reported solubilities can be partially explained from fig. 6 which is a partial phase diagram of the Ta-H system determined from heat capacity data, X-ray measurements, and electrical resistivity measurements by Waite, Wallace and Craig [78]). The slope of the boundary between α-tantalum and the α + β two phase region is fairly shallow at about room temperature thus causing the solubility limit of hydrogen in tantalum to be sensitive to slight temperature variations.

Tantalum metal is body centered cubic, the lattice parameter of the α-phase expanding with increasing hydrogen content according to the relation:
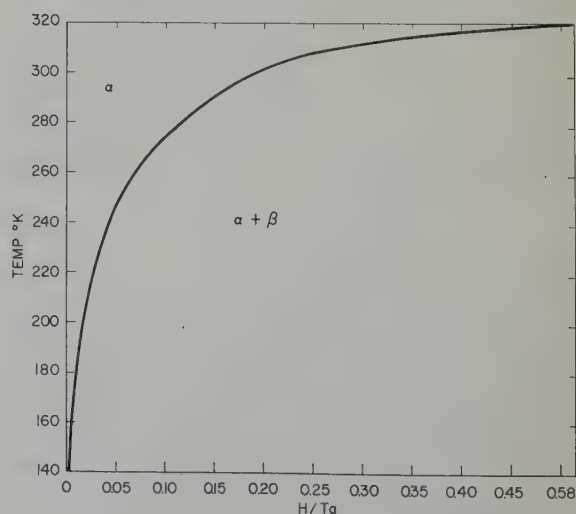

Fig. 6. Partial phase diagram of the tantalum-hydrogen system.

$$a_0 = 3.303 + 2.5 \times 10^{-3} N,$$

where N is the atomic percent of hydrogen. The β-phase is body centered tetragonal at about $TaH_{0.5}$ with $a_0 = 3.38$ Å and $c = 3.41$ Å. The hydrogen atoms are believed to occupy the octahedral interstices ($\frac{1}{2}$, $\frac{1}{2}$, 0). With increasing hydrogen content, the β-phase gradually becomes orthorhombic. At $TaH_{0.8}$, the lattice parameters [75] of the orthorhombic structure are $a_0 = 4.728$, $b_0 = 4.778$ and $c_0 = 3.428$ Å.

Nuclear magnetic resonance studies [79] of tantalum hydride indicated that the hydrogen atoms had strong internal motion above 215° K but become tightly bound below this temperature.

2.5. HYDRIDES OF METALS ABOVE GROUP V A

The transition metals above Group V do not, in general, form hydrides. Some of them such as Mn, Fe, Ni will dissolve small quantities of hydrogen. However, hydrides of Pd, Cr and Cu have been prepared.

Palladium Hydride

Historically more study has been devoted to the palladium-hydrogen system than any other metal-hydrogen system. Since an excellent review of this system is given by Smith [1]), only a short discussion will be given here to include some of the more recent work.

Hydrogen dissolves in face centered cubic palladium with an expansion [71] of the lattice from 3.891 Å to 3.894 Å at $PdH_{0.05}$. At about this composition, a new phase is formed having the same f.c.c. structure as palladium but a larger lattice parameter, 4.027 Å. This new phase can be considered a hydride phase but is usually designated as β. The two phases co-exist until an H/Pd ratio of about 0.7, above which only the hydride phase exists. The β-phase continues to expand with addition of hydrogen to about 4.07 Å. Pressure-composition-temperature studies [80,81] indicate that the stoichiometric composition would be PdH. The dissociation pressure of the hydride is given by the usual relation if $A = 1877$ and $B = 7.48$. From

a calorimetric study of the heat of absorption and desorption of hydrogen in palladium, Nace and Aston [82] have calculated the heat of formation of palladium hydride (of hydrogen content $PdH_{0.5}$) from pure palladium as -9.440 kcal/mole H_2. Nace and Aston [83] have also made a low temperature thermodynamic study of this system.

From a neutron diffraction study, Worsham et al. [84] have established that the hydrogen atoms in palladium hydride are situated in the octahedral interstices of the f.c.c. palladium lattice to give a hydrogen deficient sodium chloride structure.

Chromium Hydride

By electrodeposition of chromium at high current densities, Snavely [85] has claimed the formation of two chromium hydrides; a hexagonal hydride with limiting stoichiometric formula CrH, and a face centered cubic hydride whose limiting stoichiometric formula is CrH_2. The maximum H/Cr ratio observed was 1.7. Trzeciak et al. [70] prepared a chromium hydride of maximum H/Cr equal to 1.6. It decomposes above about $-10°$ C.

Copper Hydride

The direct combination of copper and hydrogen gas does not yield a hydride. However, a hydride, CuH, can be prepared by the reaction of copper sulfate with hypophosphorous acid [86]. The structure is the hexagonal wurtzite structure with lattice parameters $a_0 = 2.89$ and $c_0 = 4.61$ Å. A neutron diffraction study [87] showed that the hydrogen atoms were at the $(0, 0, \frac{3}{8})$, $(\frac{1}{3}, \frac{2}{3}, \frac{7}{8})$ positions and the copper atoms at the $(0, 0, 0)$ and $(\frac{1}{3}, \frac{2}{3}, \frac{1}{2})$ positions.

2.6. ALLOY HYDRIDES

Although there has been a fair amount of work on the solubility of hydrogen in alloys, until recently virtually no work has been done on the formation of hydrides from alloys. However, because of the advantages of developing new hydrides with desirable properties for nuclear power applications, studies are being

performed on various alloy-hydrogen systems, at the present time.

Trzeciak et al.[70] have investigated the hydrogen retention of a large number of titanium and zirconium alloys. Under hydriding conditions which gave a H/Ti ratio of 1.75 for pure titanium, the addition of vanadium caused an increase of the hydrogen to metal ratio to 1.96 at 14 at % V. At 69 at % V, a maximum N_H equal to 10.1 was reached. The addition of Nb, Mo, Mn and Zr also caused some increase in the hydrogen retentive capacity of titanium. The maximum H/M ratio of 2.16 was obtained with 18 at % Mo. Chromium caused a decrease in H/M ratio.

For the case of zirconium, Nb, V, Mo, Sn and Cr all caused a decrease in the hydrogen to metal ratio. On the other hand, addition of 2.3 at % Ni caused an increase of H/M from 1.92 to 2.17. However, the presence of 33 at % Ni caused a decrease to an H/M of 1.04.

A study of the effect of alloying elements on the thermal stability of zirconium hydrides indicated no large effect caused by low concentrations of alloying elements. The formation of intermetallic compounds, however, seemed to result in a decrease in thermal stability.

Gulbransen et al.[88] studied the reaction of 50 wt percent U-Zr alloy with hydrogen. In all cases, the only hydride phase formed seemed to be zirconium hydride.

Libowitz, Hayes and Gibb [89] showed that the intermetallic compound ZrNi formed a definite hydride approaching the stoichiometric composition $ZrNiH_3$. The maximum H/Zr ratio observed was 2.93. This hydride has the structure of the intermetallic compound, which is othorhombic [90]), rather than one resembling zirconium hydride. The dissociation pressure is considerably higher than that of zirconium, reaching one atmosphere at about 275° C. The pressure-composition isotherms exhibited a very large hysteresis effect.

At the temperature studied (100–250° C), close to one hydrogen atom per zirconium atom dissolved in the alloy before formation of the trihydride. It has not been established whether a monohydride, ZrNiH, exists at lower temper-

atures. In any case, the heat of the reaction:

$$ZrNiH + \tfrac{1}{2}(2-x)H_2 \rightarrow ZrNiH_{3-x}$$
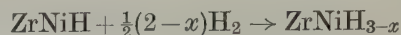
was found to be -18.4 kcal/mole H_2.

A study of the reaction of the intermetallic compound Zr_2Ni with hydrogen was carried out by Gibb and Krutenat [91]. The sample contained some excess nickel. Assuming this was present as ZrNi as indicated by the phase diagram of the Zr-Ni system [92], the maximum composition of the hydride formed would be $Zr_2NiH_{4.85}$. This is higher than the value $Zr_2NiH_{3.12}$ obtained by Trzeciak et al.[57]. Further investigations are being carried out on the Zr-Ni-H system.

3. The Saline Hydrides

Although the hydrides of the alkali and alkaline earth metals are not classed as transition metal hydrides, a brief discussion of their properties will be given here as a basis for comparison with transition metal hydrides. These hydrides are also of interest to nuclear technology mainly for shielding applications.

The hydrides of the Group I A and II A metals are predominantly ionic and are, therefore, often referred to as saline or salt-like hydrides. The hydrides of the alkali metals have the face centered cubic sodium chloride structure and resemble the alkali halides in their physical properties. The lattice parameters are shown in table 5. Lithium hydride is the only hydride which can be melted at normal hydrogen pressures, the others dissociating before reaching their melting point. The dissociation pressures are related to temperature by the values of A and B shown along with heats of formation in table 5.

The alkali hydrides are also similar to the alkali halides in the formation of color centres. Pretzel [98] has observed several absorption bands in lithium hydride one of which is due to the F center, its maximum occurring at 5660 Å thus giving rise to a bluish color in the crystal.

The alkaline earth hydrides from calcium through barium form orthorhombic crystals whose lattice parameters are given in table 6. These hydrides also dissociate before melting.

Their heats of formation and dissociation pressures are also given in table 6.

Magnesium hydride, MgH_2, was prepared [101] by heating magnesium in hydrogen under high pressures (up to 70 atm). Its dissociation pressure is quite high (reaches one atm at about

considering the energy necessary to dissociate the hydrogen molecule, and also the high exothermic heats of formation of the hydrides, it appears that rather strong metal-hydrogen bonds are formed in a hydride. Alternatively, the nature of the saline hydrides supports the

TABLE 5

Properties of alkali metal hydrides

Hydride	Lattice parameter [93] (Å)	Dissociation pressures		Heats of formation (kcal/mole) hydride
		A	B	
LiH	4.083	8224	9.926 [96]	−21.67 [95]
NaH	4.897	5958	10.47 [94]	−13.49 [95]
KH	5.708	6300	11.86 [97]	−13.82 [95]
RbH	6.049	4930	9.51 [97]	−11.3 [97]
CsH	6.389	4410	9.25 [97]	−10.1 [97]

TABLE 6

Properties of the alkaline earth hydrides

Hydride	Lattice parameters [99] (Å)			Dissociation pressures		Heat of formation [84] (kcal/mole)
	a_0	b_0	c_0	A	B	
CaH_2	6.851	5.948	3.607	10870	11.49 [97]	−45.1
SrH_2	7.358	6.377	3.882	10400	11.10 [100]	−42.3
BaH_2	7.845	6.801	4.175	6450	8.20 [100]	−40.9

285° C) and can be expressed by the relation [102]:

$$\log_{10} P (\text{atm}) = -\frac{4.090 \times 10^3}{T} - 2.441 \log_{10} T$$
$$+ 4.524 \times 10^{-3} T - 2.277 \times 10^{-6} T^2 + 12.214.$$

The heat of formation of MgH_2 is -18.6 kcal/mole at 25° C. Its crystal structure is body centered tetragonal with $a_0 = 4.517$ Å and $c_0 = 3.021$ Å. There are two magnesium atoms per unit cell at $(0, 0, 0)$ and $(\frac{1}{2}, \frac{1}{2}, \frac{1}{2})$ and four hydrogen atoms at $\pm (x, x, 0), \pm (x+\frac{1}{2}, \frac{1}{2}-x, \frac{1}{2})$ where $x = 0.306$.

4. The Nature of Transition Metal Hydrides

In reviewing the phase relations of transition metal hydrides, it is seen that they can all deviate from their stoichiometric compositions to a considerable extent. It has generally been assumed that hydrogen enters a transition metal lattice interstitially as protons with the extra electrons being distributed in the d-band (or f-band) of the metal-like lattice. However,

notion that the crystal can be regarded as made up of hydride anions and metal cations. The particular case of LiH being almost literally this structure. The nature of the metal-hydrogen binding and the reason for the deviations from stoichiometry are probably the two problems of most interest in transition metal hydrides.

4.1. THEORETICAL STRUCTURAL CONSIDERATIONS

By comparing experimentally determined pressure-composition-temperature relations with those derived theoretically on the basis of a proposed model, insight can be gained into the structure of hydrides. Using the assumption that the energy of absorption of hydrogen increases as the number of sites already occupied increases, Lacher [103] derived, from statistical mechanical considerations, the pressure-composition-temperature relations for the absorption

of hydrogen by a metal. For the hydrogen pressure, P, as a function of the fraction of interstitial sites occupied, θ, and temperature, T, he obtained an expression which can be put into the form:

$$\ln P = \ln P_0 + 2\ln \frac{\theta}{1-\theta} + \frac{4T_c}{T}(1-2\theta) \quad (1)$$

where P_0 is the pressure at $\theta = \frac{1}{2}$ (i.e., the pressure of the two-phase region, metal + hydride), and T_c is the critical temperature or temperature at which the metal and the hydride are miscible. The agreement between the isotherms calculated from this equation and those observed for the palladium-hydrogen system were quite good. Harasima et al.[104] extended Lacher's derivations by considering the effect of the expansion of the lattice on the energy of the interstitial protons during the absorption of hydrogen. This resulted in an additional θ^2 term in eq. (1) and asymmetry of the isotherms with respect to the critical point. This asymmetry is actually observed experimentally.

Using a thermodynamic treatment and assuming that the nonstoichiometry of hydrides was due to the solid solution of metal in the hydride phase, Messer [105] derived the following expression for pressure-composition isotherms in metal-hydrogen systems:

$$\ln P = \ln P_0 + \frac{2}{s}\ln \frac{n}{s-n} + \frac{4T_c}{sT}\left(1-2\frac{n}{s}\right) \quad (2)$$

where n is the hydrogen to metal ratio at pressure P, and s is the hydrogen to metal ratio in the stoichiometric hydride. Since $\theta = n/s$, this equation agrees with that of Lacher except for the $1/s$ factor of the last two terms in Messer's equation.

A somewhat broader statistical mechanical approach to the problem of interstitial solid solutions was taken by Rees [106]. He assumed that all the interstitial sites are not crystallographically equivalent as hydrogen atoms are added. For sites of the first kind, the absorption energy is E_1; for the second kind E_2, etc. The number of sites of any particular kind available for occupation depends the upon number of the previous kind already occupied. For example, sites of the ith kind are created by occupation

of sites of the $(i-1)^{th}$ kind. Using this assumption and a method similar to Lacher's, Rees derived component isotherms for each kind of site as follows:

$$\ln P = 2\ln \frac{\theta_i}{1-\theta_i} + \frac{D_0 - 2E_i - 4\theta E_{ii}}{kT} + \ln f(T)$$

$$\ln P = 2\ln \frac{\theta_{(i+1)}}{\theta_i - \theta_{(i+1)}}$$
$$+ \frac{1}{kT}\left[D_0 - 2E_{(i+1)} - 4\frac{\theta_{(i+1)}}{\theta_i}E_{i+1,i+1}\right]$$
$$+ \ln f(T)$$

where D_0 is the dissociation energy of molecular hydrogen, E_i is the energy of a hydrogen atom in a site of the ith kind, E_{ii} represents the attractive interaction energy of two interstitial H atoms in sites of the ith kind, and $f(T)$ is a slowly varying function of temperature. The total pressure-composition isotherm derived from these component isotherms gives rise to a separate plateau region for each kind of site present. Therefore, these equations are particularly applicable to metal hydrogen systems in which more than one hydride phase is formed, or in which the β-phase of the metal is formed in addition to a hydride phase. The assumption is made that the effect of changes in lattice symmetry and cell dimensions are negligible.

Martin and Rees [107] have applied these equations to the P-C-T data on the zirconium-hydrogen system [18]. A value of 66.6 kcal/mole was calculated for the energy of hydrogen atoms in β-Zr sites and 70.4 kcal/mole for H atoms in the hydride phase. The interaction energies were 2.52 and 4.57 kcal/mole, respectively. The heat of formation of ZrH_2 was calculated to be -41.4 kcal/mole. This is slightly lower than the experimental values of Douglas [19] and Edwards [17].

These equations have also been applied to the titanium-hydrogen system by Kant [108]. The values of E_i and E_{ii} were 63.9 and 1.0 kcal/mole, respectively for the β-phase, and 66.9 and 3.5 kcal/mole for the γ-phase. A calculated value of -32.9 kcal/mole was obtained for the heat of formation of TiH_2.

Except in Messer's thermodynamic treatment, these methods assume interstitial solid solution

of the hydrogen in a metal lattice. Because of their large deviations from stoichiometry, metallic appearance, and high electrical conductivity, transition metal hydrides have been referred to as solid solutions or interstitial compounds. This would imply that the structure of the metal lattice in the hydride has the same structure as in the pure metal. That this is not the case for the Group III A and IV A metals can be seen from table 7 where only cerium and actinium do not change structure on hydriding. Therefore, transition metal hydrides appear to be definite chemical compounds (i.e., compounds having a characteristic structure different from that of the component elements). Even for the case of cerium and actinium, the large discontinuous increase in lattice parameter indicates the formation of a definite compound rather than a solid solution.

Nuclear magnetic resonance studies [79] on several hydrides gave broad resonance line widths at room temperature for TiH_2, ZrH_2 and ThH_2, of the same order of magnitude as for the saline hydrides CaH_2 and NaH. The broad line width indicated that the hydrogen atoms were tightly bound in the hydride lattice. On the other hand, the line widths of tantalum, vanadium [109], and palladium [110] hydrides indicate internal motion of the hydrogen atoms.

If the group III A and IV A hydrides are definite chemical compounds, their non-stoichio-

metry can be attributed to lattice defects, either hydrogen vacancies or metal interstitials, since the hydrides are always hydrogen deficient. Assuming the presence of lattice defects, Anderson [111] has derived pressure-composition-temperature relations for binary one-to-one compounds. Libowitz [112] modified Anderson's treatment to include compounds of the form AB_s, where s is not necessarily equal to unity. For the case of anion vacancies in the lattice, the following expression was obtained:

$$\ln P = \ln P_0 + 2 \ln \frac{n}{s-n} + \frac{2E_{DD}}{kT}\left(\frac{2n}{s} - 1\right) \quad (3)$$

where $2E_{DD}/z$ is the attractive interaction energy between two defects, and z is the number of nearest neighbor hydrogen sites around each hydrogen site. On the other hand, assuming metal interstitials, the following expression was obtained [113]:

$$\ln P = \ln P_0 + \frac{2}{s} \ln \left[\frac{n+n\alpha-s}{s-n}\right] + \frac{2E_{DD}}{skT}\left[\frac{2n+n\alpha-2s}{\alpha n}\right] \quad (4)$$

where α is the proportionality constant between the number of interstitial positions and the number of metal atoms on normal lattice sites. α depends on the structure of the hydride. Eq. (4) differs from the equation previously given [112] for metal interstitials which was derived from incorrect assumptions. Eqs. (3) and (4) can also be derived from strictly thermodynamic principles by treating vacancies and interstices as chemical entities.

If the composition in eq. (3) were expressed as the fraction of vacant sites rather than hydrogen to metal ratio, this equation would be essentially identical to the ones given by Anderson [111] and Lacher. The agreement with Lacher's equation is not surprising since Lacher was assuming interstitial hydrogen in a metal lattice which is equivalent to hydrogen vacancies in a hydric lattice. However, eq. (4) differs from the previous equations by the $1/s$ factor in the last two terms, even when the composition is expressed in fraction of interstitial sites occupied. The equation does becomes identical to Anderson's for one-to-one binary compounds

TABLE 7

Structures of metals and corresponding hydrides

Metal	Metal structure	Hydride	Hydride structure
Ti	h.c.p.	TiH_2	f.c.c.
Zr	h.c.p.	ZrH_2	f.c.t.
Hf	h.c.p.	HfH_2	f.c.t.
La	h.c.p.	LaH_2	f.c.c.
Ce	f.c.c. ($a_0 = 5.16$ Å)	CeH_2	f.c.c. ($a_0 = 5.58$ Å)
Pr	h.c.p.	PrH_2	f.c.c.
Nd	h.c.p.	NdH_2	f.c.c.
Sm	rhombohedral	SmH_2	f.c.c.
Gd	h.c.p.	GdH_2	f.c.c.
Ac	f.c.c. ($a_0 = 5.31$ Å)	AcH_2	f.c.c. ($a_0 = 5.67$ Å)
Th	f.c.c.	ThH_2	f.c.t.
		Th_4H_{15}	b.c.c.
Pa	b.c.t.	PaH_3	β-W (cubic)
U	orthorhombic	UH_3	β-W (cubic)

(i.e., when $s = 1$). The $1/s$ factor arises from the fact that the formation of an interstitial metal atom, which is in excess over the stoichiometric ratio, is associated with the loss of s hydrogen atoms from the lattice. Since Messer [105] was implicitly assuming the formation of interstitial metal (by considering the activity of metal rather than the activity of vacancies) his equation also contained the $1/s$ factor. Messer's equation differs from eq. (4), however, because its derivation did not include interstitial positions as a chemical entity.

It should be pointed out that eqs. (3) and (4) were derived assuming only one type of defect is predominant, and that the interaction energy term, E_{DD}, is independent of the concentration of defects. By comparing with experimental P-C-T data, these equations can be used to determine whether hydrogen vacancies or metal interstitials are the cause of the non-stoichiometry of hydrides, as well as to calculate defect interaction and formation energies.

The application [112] of these equations to the uranium-hydrogen system indicated that hydrogen vacancies were present in the uranium hydride lattice. The interaction energy between two vacancies was calculated as 66. kcal/mole. During the dissociation of a hydride, the following processes can be considered to occur (assuming the formation of hydrogen vacancies):

$$E_D + H \text{ (lattice site)} \rightarrow \square + H \text{ (surface)}$$

$$H \text{ (surface)} \rightarrow \tfrac{1}{2} H_2 \text{ (gas)} + \tfrac{1}{2} D_0$$

$$(N_v z/N)\, \square \rightarrow \tfrac{1}{2}(N_v z/N)\,\square_2 + \tfrac{1}{2}(N_v z/N)\,(2E_{DD}/z)$$
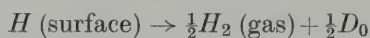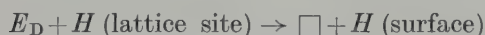
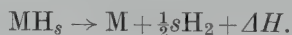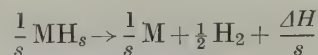where E_D is the energy necessary to form a hydrogen vacancy, $\square$, D_0 is the dissociation energy of hydrogen, $(N_v z/N)$ is the number of vacancy pairs per vacancy, N_v is the number of hydrogen vacancies in the lattice, and N is the number of hydrogen sites. When a lattice is dissociated $N_v = N$. Therefore, the total energy required for dissociation of a hydride is $E_D - \tfrac{1}{2}D_0 - E_{DD}$. The dissociation equation for a hydride, MH_s, is usually written:

$$MH_s \rightarrow M + \tfrac{1}{2}s H_2 + \Delta H.$$

Writing this equation per gram atom of hydrogen:

$$\tfrac{1}{s} MH_s \rightarrow \tfrac{1}{s} M + \tfrac{1}{2} H_2 + \frac{\Delta H}{s}$$

where ΔH is the heat of formation per mole of hydride. Therefore,

$$\frac{\Delta H}{s} = -(E_D - \tfrac{1}{2}D_0 - E_{DD}).$$

The energy necessary to form a vacancy can now be calculated from the heat of formation of the hydride, and the interaction energy between vacancies, $(2E_{DD}/z)$. For uranium hydride a value of 68.3 kcal/mole was calculated for E_D.

In general, the dissociation of a hydride can be described in the following manner. As hydrogen is removed from a hydride near its stoichiometric composition, defects are formed (either hydrogen vacancies or interstitial metal). These defects attract each other with an energy $2E_{DD}/z$ and agglomerate. As more hydrogen is removed, a point is reached at which the lattice cannot accommodate any more defects. Further removal of hydrogen causes the hydride lattice to break down or dissociate into two phases; the hydride saturated with defects, and the metal saturated with dissolved hydrogen (or a lower hydride). The nonstoichiometric homogeneity range is determined by the attractive interaction energy between defects, $2E_{DD}/z$. The greater the value of E_{DD}, the smaller the concentration of vacancies necessary to break down the lattice.

4.2. The ionic character of transition metal hydrides

The nature of the chemical bond in transition metal hydrides is not known. However, there is evidence that the bond in the Group III A and IV A hydrides has some ionic character. Attempts to calculate a hydrogen atom radius from interatomic distances in these compounds on the basis of metallic or covalent bonding have led to variable values. Because of the similarity between the heats of formation of rare earth hydrides and saline hydrides, Dialer [114] suggested that the metal-hydrogen

bonds in the rare earth hydrides of composition MH_2 are ionic. Libowitz and Gibb [115] extended the assumption of ionic bonding to all the hydrides of the Group III A and IV A metals including the lanthanide and actinide series and obtained a constant value of 1.29 ± 0.05 Å for the hydride anion radius using Zachariasen's cation radii and coordination number corrections [116] as shown in table 8. The only hydride which does not give good agreement with this picture is HfH_2 which has a calculated H-radius of 1.20 Å. Regardless of the valence exhibited by the metal in the hydride, the radii used are for cations with the rare gas electronic structure, except for the lanthanide series where the filling of the 4f shell was considered to have negligible influence on the xenon electronic structure, and plutonium where the more stable tetravalent state was used. Therefore, in every case, the charge of the cation exceeds its valence in the hydride. The extra electrons which do not contribute to the formation of hydride anions probably take part in residual metallic bonding thus giving rise to the high electrical conductivity of these compounds. This ionic character would also explain the brittleness of these compounds. This type of bonding also seems to be characteristic of the transition metal chalcogenides. Studies [117] on some rare earth monochalcogenides indicated

that trivalent cations and divalent anions were present in the lattices, with the additional electron per atom contributing to the metallic nature of these compounds. Magnetic and crystallographic studies of thorium [118] and uranium [119] sulfides showed that tetravalent cations were present even in the subsulfides of these metals, with metallic bonding accounting for the additional electrons.

The value of 1.29 Å for the ionic radius of the hydride anion is in fair agreement with the hydride anion radii calculated in the saline hydrides if the electronegativity of the cation is considered. The hydride anion radius decreases from about 1.53 Å to 1.37 Å in the series CsH to LiH, i.e., with increasing electronegativity of the cation. Since the electronegativities of the transition metals are all higher than lithium, a value for the radius of the hydride anion somewhat less than 1.37 Å would be expected.

Magnetic susceptibility studies of transition metal hydrides have usually been cited as evidence for the formation of protons on hydriding. Fitzwilliam et al.[120] have observed that the paramagnetic susceptibility of zirconium decreases on the addition of hydrogen, a minimum occurring at H/Zr equal to two. Similar observations have been made on the palladium-hydrogen [1], niobium-hydrogen [121], tantalum-hydrogen [77] and lanthanum- hydrogen [122] systems. In each case, the magnetic susceptibility decreases with increasing hydrogen content, in palladium a constant value being reached at H/Pd = 0.7. (It should be mentioned here that susceptibility measurements on the titanium-hydrogen system show an increase in paramagnetic susceptibility with composition[11]). The decrease in magnetic susceptibility with hydrogen content for most hydrides has been explained by the filling of holes in the d-band of the metal with electrons from the hydrogen atoms to form protons. However, the pairing of electron spins in the formation of hydride anions will also give decreasing magnetic susceptibility with increasing hydrogen content.

The observed migration of protons in the

TABLE 8

Hydride anion radii in metallic hydrides

Hydride	M-H distance (Å)	C.N. correction	H-radius, (Å)
TiH_2	1.93	0.08	1.25
ZrH_2	2.09	0.08	1.24
LaH_2	2.45	0.08	1.33
CeH_2	2.42	0.08	1.32
PrH_2	2.39	0.08	1.31
NdH_2	2.37	0.08	1.30
SmH_2	2.33	0.08	1.28
GdH_2	2.30	0.08	1.27
AcH_2	2.46	0.08	1.27
ThH_2	2.41	0.08	1.34
PaH_3	2.32	0.19	1.23
UH_3	2.32	0.19	1.27
PuH_2	2.32	0.08	1.34

Av. 1.29 ± 0.05 Å

palladium-hydrogen [123]), tantalum-hydrogen and titanium-hydrogen [124]) systems has often been cited as evidence for the existence of protonic hydrogen. However, all these measurements were carried out at hydrogen contents low enough so that only the metallic phase containing hydrogen in solution was present. To date, there have been no results available on hydrogen migration in an electric field in the single phase hydride region.

In some preliminary calculations by Gibb [125]), in which the ability of a metal to form a hydride is deduced from lattice energies, good agreement with experimental fact was obtained for lattice energies calculated on the basis of an ionic model for transition metal hydrides.

5. Conclusion

A review of the properties of transition metal hydrides shows that, in general, the hydrides within any one group of the periodic table have similar properties. The Group IV A metals all form hydrides with a maximum hydrogen to metal ration of two. These hydrides all have a cubic fluorite structure at lower hydrogen contents and become increasingly tetragonal as the hydrogen to metal ratio approaches two. This effect is most pronounced in zirconium hydride and least in titanium hydride.

The rare earth metals form cubic trihydrides in addition to dihydrides having the cubic fluorite structure (except ytterbium and europium). The trihydride takes on a hexagonal structure for the case of gadolinium and hydrides of higher atomic number. On the other hand, the actinide series hydrides do not seem to have much in common with each other. The plutonium hydrides resemble the hydrides of the rare earth metals of higher atomic number, but the hydrides of uranium and thorium are quite different, although the lower hydride of thorium ThH_2 does have a fluorite structure. There has been insufficient work on the other hydrides in this series to draw any conclusion as to similarities in properties.

The hydrides of the Group V A metals form hydrides approaching the stoichiometric ratio

MH, and have structures identical or similar to the parent metal. The only other transition metals which appear to form hydrides are palladium, chromium, and copper and some alloys of hydride-forming with non-hydride-forming metals.

In conclusion, it should be emphasized that the hydrides of the transition metals, in particular those of Group III A and IV A metals (including lanthanides and actinides), are definite chemical compounds rather than interstitial solid solutions. The large deviations from stoichiometry in these compounds can be attributed to lattice defects as in most transition metal oxides or sulfides. The metallic hydrides appear to have some degree of ionic character along with their metallic properties. However, there is obviously need for further study in order to fully understand the nature and bonding of these interesting compounds.

References

[1] D. P. Smith, Hydrogen in Metals (Univ. of Chicago Press, 1948)

[2] D. T. Hurd, An Introduction to the Chemistry of the Hydrides (John Wiley and Sons, Inc., 1952)

[3] A. D. McQuillan, Proc. Roy. Soc. (London) 204 (1950) 309

[4] R. M. Haag and F. J. Shipko, J. Am. Chem. Soc. 78 (1956) 5155

[5] T. R. P. Gibb, Jr., J. J. McSharry and R. W. Bragdon, J. Am. Chem. Soc. 73 (1951) 1751

[6] G. Hägg, Z. Physik Chem. Abt. B 11 (1931) 433

[7] S. S. Sidhu, L. Heston and D. D. Zauberis, Acta Cryst. 9 (1956) 607

[8] H. L. Yakel, Jr., ibid 11 (1958) 46

[9] E. J. Goon and J. Malgiolio, A.E.C. Report NYO-7547 (April 1, 1958)

[10] E. P. Wohlfarth, Acta Met. 4 (1956) 225

[11] W. Trzebiatowski and B. Stalinski, Bull. Acad. Polon. Sci. 1 (1953) 131

[12] M. K. Wilkinson and C. G. Shull, Private communication

[13] E. A. Gulbransen and K. F. Andrew, J. Metals 7 (1955) 136

[14] M. W. Mallett and W. M. Albrecht, J. Electrochem. Soc. 104 (1957) 142

[15] C. E. Ells and A. D. McQuillan, J. Inst. Metals 85 (1956) 89

[16] D. A. Vaughan and J. R. Bridge, J. Metals 8 (1956) 528

17) R. K. Edwards, P. Levesque and D. Cubicciotti, J. Am. Chem. Soc. 77 (1955) 1307

18) M. N. A. Hall, S. L. H. Martin and A. L. G. Rees, Trans. Faraday Soc. 41 (1944) 306

19) T. B. Douglas, J. Am. Chem. Soc. 80 (1958) 5040

20) R. K. Edwards, P. Levesque and D. Cubicciotti, ONR Report NP-4884 (August 1953)

21) P. T. Gilbert, Jr., A.E.C. Report NAA-SR-1508 (October 1956)

22) G. G. Libowitz, to be published

23) E. A. Gulbransen and K. F. Andrew, J. Electrochem. Soc. 101 (1954) 474

24) W. Trzebiatowski and B. Stalinski, Rocznicki Chem. 30 (1956) 691

25) P. W. Bickel, Private communication

26) D. Whitwham, M. A. Huber and J. Hérenguel, Acta Met. 7 (1959) 65

27) R. K. Edwards and P. Levesque, J. Am. Chem. Soc. 77 (1955) 1312

28) V. V. Sofina, Z. M. Azarkh and N. N. Orlova, Kristallografiya 3 (1958) 539

29) R. E. Rundle, C. G. Shull and E. O. Wollan, Acta Cryst. 5 (1952) 22

30) S. L. H. Martin and A. L. G. Rees, Trans. Faraday Soc. 50 (1954) 343

31) S. S. Sidhu and J. C. McGuire, J. Appl. Phys. 23 (1952) 1257

32) S. S. Sidhu, Acta Cryst. 7 (1954) 447

33) S. S. Sidhu, J. Chem. Phys. 22 (1954) 1062

34) R. K. Edwards and E. Veleckis, paper presented at the 131st meeting of the American Chemical Society, Miami, Fla., September 1957; E. Veleckis, M.A. Thesis, Illinois Institute of Technology (1957)

35) S. S. Sidhu, F. P. Campos and D. D. Zauberis, Nuclear Sci. and Eng. 3 (1958) 778

36) R. N. R. Mulford and C. E. Holley, Jr., J. Phys. Chem. 59 (1955) 1222

37) C. E. Holley, Jr., R. N. R. Mulford, F. H. Ellinger, W. C. Koehler and W. H. Zachariasen, ibid 59 (1955) 1226

38) W. L. Korst and J. C. Warf, paper presented at the 129th Meeting of the American Chemical Society, Dallas, Texas, April 1956; W. L. Korst, Ph.D. Thesis, Univ. of So. Calif. (June 1956)

39) K. Dialer and W. Rothe, Naturwissenschaften 42 (1955) 44

40) V. I. Mikheeva and M. E. Kost, Zhur. Neorg. Khim. 3 (1958) 260; Chem. Abstr. 52 (1958) 19639

41) G. E. Sturdy and R. N. R. Mulford, J. Am. Chem. Soc. 78 (1956) 1083

42) R. N. R. Mulford, AECU-3813

43) W. L. Korst and J. C. Warf, Acta Cryst. 9 (1956) 452

44) J. C. Warf, J. Donohue and K. Hardcastle, ONR Report NP-6531 (October 1957)

45) J. Daou and R. Viallard, Compt. rend. 243 (1956) 2050

46) B. Stalinski, Bull. Acad. Polon. Sci. Cl III, 5 (1957) 1001

47) J. D. Farr, A. L. Giorgi, M. G. Bowman and R. K. Money, Los Alamos (USA) Report La-1545 (1953)

48) R. W. Nottorf, AECD 2984 (1945)

49) M. W. Mallett and I. E. Campbell, J. Am. Chem. Soc. 73 (1951) 4850

50) G. G. Libowitz, J. Phys. Chem. 62 (1958) 296

51) W. H. Zachariasen, Acta Cryst. 6 (1953) 393

52) P. A. Sellers, S. Fried, R. E. Elson and W. H. Zachariasen, J. Am. Chem. Soc. 76 (1954) 5935

53) F. H. Spedding, A. S. Newton, J. C. Warf, O. Johnson, R. W. Nottorf, I. B. Johns and A. H. Daane, Nucleonics 4 (1949) 1

54) H. E. Flotow and B. M. Abraham, US Atomic Energy Commission Publication, AECD-3074 (1951)

55) G. G. Libowitz and T. R. P. Gibb, Jr., J. Phys. Chem. 61 (1957) 793

56) B. M. Abraham and H. E. Flotow, J. Am. Chem. Soc. 77 (1955) 1446

57) R. E. Rundle, ibid 69 (1947) 1719

58) R. E. Rundle, ibid 73 (1951) 4172

59) R. N. R. Mulford, F. H. Ellinger and W. H. Zachariasen, ibid 76 (1954) 297

60) R. Caillat, H. Coriou and P. Perio, Compt. rend. 237 (1953) 812

61) W. Trzebiatowski, A. Sliwa and B. Stalinski, Roczniki Chem. 26 (1952) 110; ibid 28 (1954) 12

62) D. M. Gruen, J. Chem. Phys. 23 (1955) 1708

63) S. T. Lin and A. R. Kaufmann, Phys. Rev. 102 (1956) 640

64) S. Fried and N. Davidson, J. Am. Chem. Soc. 70 (1948) 3539

65) R. N. R. Mulford and G. E. Sturdy, ibid 77 (1955) 3449

66) R. N. R. Mulford and G. E. Sturdy, ibid 78 (1956) 3897

67) B. J. McDonald and J. B. Fardon, J. Chem. Soc. (1956) 781

68) E. F. Westrum and L. Eyring, J. Am. Chem. Soc. 73 (1951) 3396

69) J. J. Katz and G. T. Seaborg, The Chemistry of the Actinide Elements (Methuen, 1957) p. 349

70) M. J. Trzeciak, D. F. Dilthey and M. W. Mallett, Battelle Memorial Institute (USA) Report BMI 1112 (1956)

71) W. B. Pearson, A Handbook of Lattice Spacings and Structures of Metals and Alloys (Pergamon Press, 1958)

72) B. W. Roberts, Phys. Rev. 100 (1955) 1257

73) W. M. Albrecht, M. W. Mallett and W. D. Goode, J. Electrochem. Soc. 105 (1958) 219

74) D. R. Knowles, UKAEA Industrial Group Report IGR-R/C-190 (1957)

75) G. Brauer and R. Hermann, Z. Anorg. u. Allgem. Chem. 274 (1953) 11

76) F. H. Horn and W. T. Zeigler, J. Am. Chem. Soc. 69 (1947) 2762

77) B. Stalinski, Bull. Acad. Polon. Sci. 2 (1954) 245

78) T. R. Waite, W. E. Wallace and R. S. Craig, J. Chem. Phys. 24 (1956) 634

79) M. A. Garstens, Phys. Rev. 79 (1950) 397

80) L. J. Gillespie and F. P. Hall, J. Am. Chem. Soc. 48 (1926) 1207

81) L. J. Gillespie and L. S. Galstaun, ibid 58 (1936) 2565

82) D. M. Nace and J. G. Aston, ibid 79 (1957) 3619

83) D. M. Nace and J. G. Aston, ibid 79 (1957) 3627

84) J. E. Worsham, Jr., M. K. Wilkinson and C. G. Shull, J. Phys. Chem. Solids 3 (1957) 303

85) C. A. Snavely, Trans. Electrochem. Soc. 92 (1947) preprint;
C. A. Snavely and D. A. Vaughan, J. Am. Chem. Soc. 71 (1949) 313

86) J. C. Warf and W. Feitknecht, Helv. Chim. Acta 33 (1950) 613

87) J. A. Goedkoop and A. F. Andresen, Acta Cryst. 8 (1955) 118

88) E. A. Gulbransen, K. F. Andrew and R. J. Ruka, Westinghouse (USA) Research Lab. Sci. Paper 100FF1010-P1 (October 16, 1956)

89) G. G. Libowitz, H. F. Hayes and T. R. P. Gibb, Jr., J. Phys. Chem. 62 (1958) 76

90) J. F. Smith, M. E. Kirkpatrick, D. M. Bailey and D. E. Williams, AEC (USA) Report ISC-1050 (March 1959)

91) T. R. P. Gibb, Jr., and R. C. Krutenat, M.S. Thesis of R. C. Krutenat, Tufts Unic. (June 1958)

92) E. T. Hayes, A. H. Roberson and O. G. Paasche, Trans. Am. Soc. Metals 45 (1953) 893

93) R. E. Elson, H. C. Hornig, W. L. Jolly, J. W. Kury, W. J. Ramsey and A. Zalkin, University of California Radiation Laboratory (USA) Report, UCRL 4519 Rev. (June 1956)

94) M. D. Banus, J. J. McSharry and E. A. Sullivan, J. Am. Chem. Soc. 77 (1955) 2007

95) S. R. Gunn and L. G. Green, ibid 80 (1958) 4782

96) F. K. Heumann and O. N. Salmon, USAEC Report KAPL-1667 (1956)

97) C. E. Messer, USAEC Report NYO 3955 (1953)

98) F. E. Pretzel, Bull. Am. Phys. Soc. 2 (1957) 155

99) E. Zintl and A. Harder, Z. Elektrochem. 41 (1935) 33

100) M. D. Banus and R. W. Bragdon, Oak Ridge National Laboratory (USA) Report CF-52-2-212 (1952)

101) F. H. Ellinger, C. E. Holley, Jr., B. B. McInteer, D. Pavone, R. M. Potter, E. Staritsky and W. H. Zachariasen, J. Am. Chem. Soc. 77 (1955) 2647

102) J. F. Stampfer, Ph.D. Thesis, Univ. of New Mexico (1958)

103) J. R. Lacher, Proc. Roy Soc. A 161 (1937) 525

104) A. Harasima, T. Tanaka and K. Sakaoku, J. Phys. Soc. Japan 3 (1948) 208

105) C. E. Messer, USAEC Report NYO 3912 (1952); NYO 3914, (Feb. 8, 1954)

106) A. L. G. Reęs, Trans. Faraday Soc. 50 (1954) 335

107) S. L. H. Martin and A. L. G. Rees, ibid 50 (1954) 343

108) A. Kant, Report WAL-TR-541/1 (May 1958)

109) R. A. Oriani, E. McCliment and J. F. Youngblood, J. Chem. Phys. 27 (1957) 330

110) R. E. Norberg, Phys. Rev. 86 (1952) 745

111) J. S. Anderson, Proc. Roy. Soc. (London) A 185 (1946) 69

112) G. G. Libowitz, J. Chem. Phys. 27 (1957) 514

113) G. G. Libowitz, Unpublished work

114) K. Dialer, Monatsch. 79 (1948) 311

115) G. G. Libowitz and T. R. P. Gibb, Jr., J. Phys. Chem. 60 (1956) 510

116) C. Kittel, Introduction to Solid State Physics, 2nd Edn. J. Wiley and Sons, Inc., (1957) p. 81

117) A. Iandelli, Gazz. Chim. Ital. 85 (1955) 881

118) E. D. Eastman, L. Brewer, L. A. Bromley, P. W. Geller and N. L. Lofgren, J. Am. Chem. Soc. 72 (1950) 4019

119) M. Picon and J. Flahaut, Bull. Soc. Chim. France (1958) 772

120) J. Fitzwilliam, A. Kaufmann and C. Squire, J. Chem. Phys. 9 (1941) 678

121) W. Trzebiatowski and B. Stalinski, Bull. Acad. Polon. Sci. 1 (1953) 317

122) B. Stalinski, ibid 5 (1957) 997

123) A. Coehn and W. Specht, Z. Physik 62 (1930) 1;
A. Coehn and H. Jurgens, ibid 71 (1930) 179;
A. Coehn and K. Sperling, ibid 83 (1933) 291

124) W. B. Hillig, Ph.D. Thesis, Univ. of Michigan (1953)

125) T. R. P. Gibb, Jr., USAEC Report NYO 7548, Part I (May 1958); Part II (Jan. 1959)

THE TRANSFORMATION TEMPERATURES OF HIGH-PURITY URANIUM

BERNHARD BLUMENTHAL †

Argonne National Laboratory, Lemont, Ill. USA

The transformation temperatures of high-purity uranium were determined by repeated thermal analyses where the rates of heating and cooling were independently controlled. The solid state transformation temperatures and the logarithm of the heating or cooling rates are related linearly. The extrapolated functions intersect at a point where the disturbing effects of hysteresis, superheating and undercooling disappear, i.e. at the equilibrium temperature. The transformation temperatures are $667.7 \pm 1.3°$ C for $\alpha \rightleftharpoons \beta$ and $774.8 \pm 1.6°$ C for $\beta \rightleftharpoons \gamma$. The mean temperature for melting and freezing is $1132.3 \pm 0.8°$ C.

Les températures de transformation de l'uranium de haute pureté ont été déterminées par des analyses thermiques répétées en contrôlant indépendamment les vitesses de chauffage et de refroidissement. Les températures de transformation dans l'état solide varient linéairement en fonction du logarithme de la vitesse de chauffage ou de refroidissement. Les fonctions extrapolées se coupent en un point où les effets perturbateurs de l'hystérésis de surchauffe ou de sous-refroidissement disparaissent, c'est à dire à la température même de l'équilibre. Les températures de transformation sont $667.7 \pm 1.3°$ C pour $\alpha \rightleftharpoons \beta$ et $774.8 \pm 1.6°$ C pour $\beta \rightleftharpoons \gamma$. La température moyenne pour la fusion et la solidification est de $1132.3 \pm 0.8°$ C.

Die Umwandlungstemperaturen von reinstem Uran wurden mit Hilfe wiederholter, thermischer Analysen unter unabhängiger Kontrolle der Erhitzungs- und Abkühlungsgeschwindigkeit bestimmt. Die Umwandlungstemperaturen des festen Zustandes und der Logarithmus der Erhitzungs- und Abkühlungsgeschwindigkeit sind linear von einander abhängig. Die extrapolierten Kurven schneiden sich in einem Punkt, wo die störenden Einflüsse von Hysterese, Überhitzung und Unterkühlung verschwinden; dieser Punkt ist die Gleichgewichtstemperatur. Die Umwandlungstemperaturen sind $667.7 \pm 1.3°$ C für $\alpha \rightleftharpoons \beta$ und $774.8 \pm 1.6°$ C für $\beta \rightleftharpoons \gamma$. Das Mittel der Schmelz- und Erstarrungstemperaturen is $1132.3 \pm 0.8°$ C.

1. Introduction

Measurements of the solid state transformation temperatures of uranium were made as early as 1942 and of its melting point in 1930. The early data were reviewed by Katz and Rabinowitch [1]. Few of these measurements have any significance today since they were made on rather impure metal under conditions where the formation of large quantities of oxide and nitride was inevitable. Nevertheless, Chipman [2] reported in 1946, in summarizing the

work of the Metallurgical Laboratory, an $\alpha \rightleftharpoons \beta$ transformation temperature of 665° C, a $\beta \rightleftharpoons \gamma$ transformation temperature of 775° C and a melting point of 1130° C; data which approach present day measurements.

In making heat content measurements, Moore and Kelley [3] found two sharp transitions at $662° \pm 3°$ C and $772° \pm 3°$ C with no evidence of hysteresis. Resistivity measurements by Dahl and Van Dusen [4], however, revealed a large hysteresis for the solid state transformations. Their data were:

$$\alpha \rightarrow \beta = 667° \text{ C} \qquad \beta \rightarrow \gamma = 772° \text{ C}$$
$$\beta \rightarrow \alpha = 645° \text{ C} \qquad \gamma \rightarrow \beta = 764° \text{ C}.$$

The data by Dahl and Van Dusen were

† B. Blumenthal is Associate Metallurgist, Argonne National Laboratory, Lemont, Ill. He is presently on leave of absence from ANL and Consultant to the "Centre d'Etude de l'Energie Nucléaire" (CEN) Mol, Belgium.

evaluated by Ginnings and Corrucini [5]) for the purpose of calculating heats of transition. They used 668° C and 774° C, probably the highest values obtained by Dahl and Van Dusen. Similar results were obtained by some of the investigators of binary phase diagrams [6–13]).

While these results appeared to be fairly consistent, they were, nevertheless, looked upon with suspicion partly because of the impurity content of the metal and partly because of the large hysteresis effects, even at low rates of heating and cooling. The very large effect of the cooling rate on the transformation temperatures was shown by Duwez [14]) who, at a rate of 8000° C/sec, obtained supercooling of the $\gamma \to \beta$ and $\beta \to \alpha$ transformations by about 200° C and 300° C, respectively.

Only one reliable datum existed for the $\gamma \rightleftharpoons L$ phase change. Dahl and Cleaves [15]) determined the freezing point (L → γ only) by taking a sequence of cooling curves at a rate of 1° C/min. Successive determinations resulted in an increase of the freezing point from 1125° C to 1133° C. Simultaneously, a reduction of the carbon content was observed in the melt; the highest freezing point was associated with a carbon content of 6 ppm. Most of the other observers reported data below 1133° C without specifying the carbon content or giving other analytical data. With the advent of high purity uranium [16, 17, 18]) and the development of precise analytical methods for impurity determinations it became possible, and indeed desirable, to determine the transformation temperatures.

Differential thermal analyses on high purity uranium were made by Baumrucker [19]). He found $T_m = 1130.9 \pm 0.4°$ C at rates ranging from 0.60° to 3.88° C/min for melting and 1.13° to 2.80° C/min for freezing. For $\alpha \rightleftharpoons \beta$ he found 666.8 $\pm$ 0.4° C for heating and 657.7 $\pm$ 0.5° C for cooling at variable rates ranging from 0.8 to 2° C/min, with a hysteresis of 9.1° C. For $\beta \to \gamma$ he found 772.2 $\pm$ 0.4° C for heating and 767.8° $\pm$ 1.5° C for cooling at variable rates of 0.72 to 4.5° C/min, with a hysteresis of 4.4° C. Dilatometric measurements of the solid state transformation temperatures at the constant rate of 1° C/min by Lloyd [19]), showed much less hysteresis than those by Baumrucker. Lloyd found 662.6 $\pm$ 0.9° C for $\alpha \to \beta$, 660.5 $\pm$ 0.6° C for $\beta \to \alpha$, 764.0 $\pm$ 1.0° C for $\beta \to \gamma$ and 768.0 $\pm$ 1.2 for $\gamma \to \beta$. Lloyd's dilatometric data are lower than those by Baumrucker. Although these data were obtained on high purity uranium, the disturbing undercooling

TABLE 1

Composition of high purity uranium

Spec. No.	Chemical analysis in ppm				Spectrochemical analysis * in ppm							Remarks
	H	C	N	O	Al	Cr	Cu	Fe	Mg	Mn	Si	
B-721	—	26–35	<10	—	7	<1	1	2	1	<1	10	Before thermal analysis
	—	28–37	<10–19	1	7	<1	1	2	1	<1	20	After thermal analysis
B-724	—	26–35	<10	—	7	<1	1	2	1	<1	10	Before thermal analysis
	—	22–25	<10	1	7	<1	1	2	2	<1	10–15	After thermal analysis
B-726	—	34–40	<10	6.6	5	<1	1	2	1	<1	20	Before thermal analysis
	—	40–50	<10	2	7	<1	1	2	1	<1	10	After thermal analysis
B-728T	.21	5	<10	22–25	5	1	1	7	L 1	<1	15	Used in solid state only
B-734	—	7–10	12	25–26	5	<1	1	2	1	<1	10	Used in solid state only

* All other elements below limits of spectrochemical detection.

and superheating effects persisted and called for a closer control of the rate factor. It became necessary to clear up these questions and establish precise equilibrium temperatures as a preliminary to a study of the constitution of the low carbon U-C alloys by B. Blumenthal, where the effect of carbon on the transformation temperatures was expected to be small.

2. Materials

The material used in this investigation was remelted high purity electrolytic uranium; the pertinent analytical data are given in table 1.

3. Experimental Apparatus

The experimental apparatus was a modified version of the high vacuum Globar resistance furnace described previously [17]). Its vacuum system was left unchanged. The heating system was rebuilt to permit repeated thermal analyses at a predetermined, yet variable rate unaffected by load oscillations caused by the common on-off controls. The furnace was heated by two separate sets of Globars; one provided the manually adjusted base load (about 2/3 of the total), the other one the control load. The latter was supplied by a Variac, which was driven by an air operated diaphragm motor (Conoflow Corp.) in conjunction with a Minneapolis-Honeywell triple range pneumatic controller (2 to 8, 6 to 12, and 10 to 16 MV). The program control was imposed by a cam cut to suit the desired cycling pattern. Since the control thermocouple was touching the outside of the furnace tube, it did not register the true temperature inside the furnace. The temperature difference due to the changing conditions of the experiments was about 25° C. To compensate for this difference the cam was cut for a temperature that much higher. With this compensation it was possible to impart any desired temperature pattern to the specimen. Since the furnace had a low heat capacity, it followed the predetermined cycle with little lag.

For melting point determinations, a specimen of about 300 grams was contained in a urania crucible; a Pt/Pt-10 % Rh thermocouple protected by a urania tube was located in its center. Care was taken to make sure that the thermocouple was secured in its central position throughout the melting and freezing cycles. The rather rigid suspension is shown in fig. 1. For the solid state transformations a similar quantity of bare metal was suspended in the furnace as shown in fig. 2. The cold junctions of both the measuring and the control thermocouples were held at 0° C in well insulated Thermos bottles. Suitable precautions were
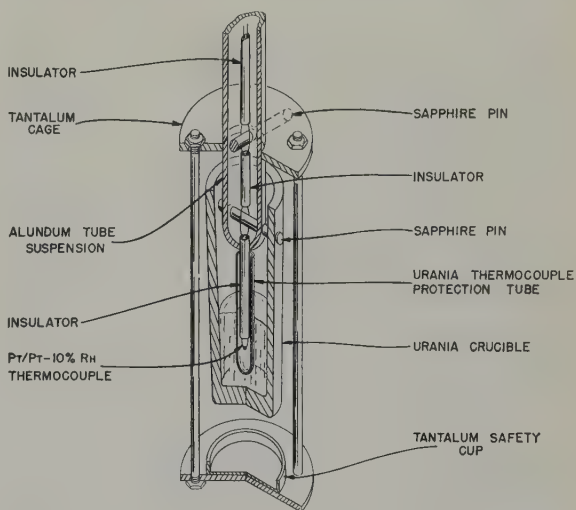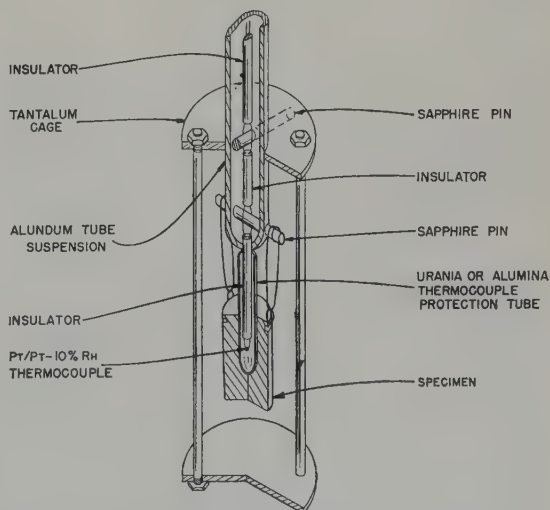

Fig. 1. Suspension of crucible for thermal analysis.

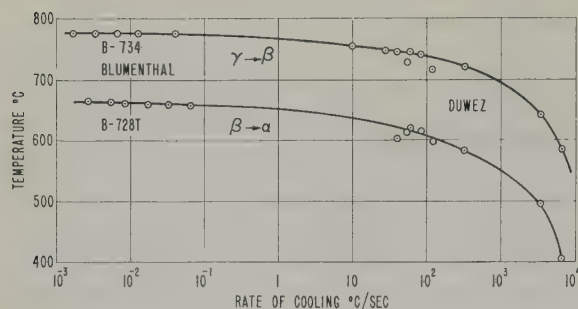Fig. 2. Suspension of specimen for solid state thermal analysis.

Fig. 3. Effect of cooling rate on the $\gamma \to \beta$ and $\beta \to \alpha$ transformation temperatures of high-purity uranium (at left data by Blumenthal, at right data by Duwez).

taken to shield crucible and melt from the cold sections of the furnace and to establish a uniform temperature gradient around the melt or the solid specimen. Despite the sensitivity of the urania refractories to thermal and mechanical stresses, the arrangement proved to be highly successful provided the system was not cooled to room temperature during an experiment. Many cycles at various rates in the range of $\pm 40°$ C around the melting point could be made over a period of days. A pressure of 5 to 7×10^{-7} mm Hg was maintained throughout each series of cycling experiments.

The specimen temperature was recorded by a specially built Leeds and Northrup Speedomax recorder with a span of 3 MV and ranges beginning at 0, 2.5, 5, 7.5, and 10 MV. Its sensitivity was 0.003 MV and its error within 0.009 MV. The instrument was calibrated for recording of the correct EMF and for mechanical differences in recording at rising or falling temperatures, before and after each experiment by means of a Rubicon potentiometer. In the later runs the paper position was checked by continuously tracing a straight line with a separate, fixed pen. Under these circumstances it was possible to read the EMF within ± 0.005 MV.

The measuring thermocouple was calibrated before and after each group of experiments over the range of 500° to 1250° C against a standard couple which had been calibrated by the National Bureau of Standards. The corrections applied to the actual temperature measure-

ments were obtained from smoothed out curves of these two calibrations. Care was taken to obtain a strain free thermocouple by annealing it in air at 1500° C. Thus four corrections were applied to each individual EMF measurement: one for errors in instrument recording, a second for errors due to paper position, a third for the calibration of the measuring thermocouple against the standard couple and a fourth for the calibration of the standard couple by NBS. Ultimately, the EMF was converted to degrees centigrade using the tables of NBS Circular No. 561.

Occasionally a heating or cooling curve, which generally confirmed the findings of the instrument, was made by direct potentiometric measurement.

4. Data

4.1. MELTING AND FREEZING

The data are given in table 2. The results were obtained at a constant rate of 0.74° C/min. Good arrests of about 22 minutes duration were obtained during the 7 to 11 cycles which were made on each specimen. Although the graphs produced by the automatic recorder gave no indication that superheating or undercooling took place, a direct potentiometric measurement on ingot B-727 showed very clearly that both effects did occur. The freezing temperatures were higher than the melting temperatures. The reason for this is not known. It may be explained, however, by the presence of a temperature gradient between the melt and the thermocouple which is shielded by a rather poorly conducting refractory (urania). This temperature gradient persists through the long arrests and causes the measured temperature to be lower during heating and higher during cooling. It is assumed that the gradients were the same on heating and cooling. The mean of the melting and freezing temperature is then the equilibrium solid $\rightleftharpoons$ liquid transformation point. This point is at $1132.3 \pm 0.8°$ C.

The difference of 1.4° C between the present results and those by Baumrucker cannot be

TABLE 2

Melting and freezing temperatures of high purity uranium at a rate of 0.74° C/min

Specimen No.	Melting point (° C)	Freezing point (° C)
B-721	1133.0	1135.1
	1132.3	1134.5
	1132.3	1134.1
	1131.9	1133.8
	1132.0	1133.9
	1132.5	1133.9
		1133.6
B-724	1131.8	1131.8
	1131.1	1131.3
	1130.9	1131.9
	1130.8	1131.9
	1131.4	1132.1
	1131.7	1131.8
	1131.6	1132.0
B-726	1130.1	1133.3
	1130.3	1133.3
	1130.6	1133.8
	1130.8	1133.3
	1130.9	1133.4
	1131.0	1133.4
	1130.7	1133.8
	1130.6	1132.9
	1130.9	1132.8
		1133.6
		1133.0
Mean of 3 ingots	1131.4 ± 0.4	1133.1 ± 0.4
Mean of melting and freezing	1132.3 ± 0.8	

explained easily. Since the melting temperatures agree within the limits of precision, the difference is due to the difference in the observed freezing temperatures. It is probable that Baumrucker missed the recalescence during solidification and that his data are too low. Since the higher temperatures agree with the earlier measurements on less pure material by Dahl and Cleaves and generally higher purity materials give higher equilibrium temperatures than lower purity materials, the higher values are believed to be more nearly true than the lower ones.

4.2. THE ALPHA-BETA TRANSFORMATION

The very large hysteresis between heating and cooling, even at low rates, and the large effect of the rate on the magnitude of this hysteresis, made a new approach to the determination of the solid state transformation points mandatory. A few direct potentiometric measurements showed clearly that not only undercooling, but also superheating are real. Furthermore, it is not at all sure that upon recalescence the latent heat evolved brings the specimen temperature back to the equilibrium temperature. Lag in response of the temperature sensing element is still another factor to be considered. The problem was, therefore, approached by measuring the transformation temperatures on heating and cooling at various constant rates. The spread between heating and cooling of the $\alpha \rightleftharpoons \beta$ transformation temperature decreased as the rate decreased. A plot of the transformation temperature versus the logarithm of the rate showed that the present data form a satisfactory continuation of Duwez'[14] data for high purity uranium obtained at much higher cooling rates (fig. 3). The left end of the curve may be regarded as a straight line. By the method of least squares, functions of the type:

$$T_{\mathrm{H}} = a_1 + b_1 \log_{10} r$$
$$T_{\mathrm{C}} = a_2 - b_2 \log_{10} r$$

were obtained, where T_{H} and T_{C} are the transformation temperatures in ° C on heating and cooling respectively, $\log_{10} r$ is the logarithm of the rate, and a_1, a_2, b_1 and b_2 are constants.
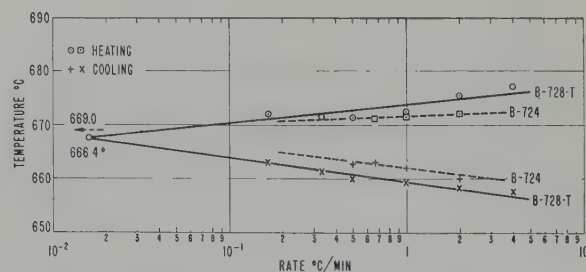

Fig. 4.   Effect of heating and cooling rate on the $\alpha \rightleftharpoons \beta$ transformation temperature of high-purity uranium (B-724 and B-728T).

The two lines intersect at the temperature $T = T_H = T_C$ which is the temperature where the disturbing factors of hysteresis, superheating and undercooling disappear and which may be regarded as the equilibrium temperature of the transformation under investigation. By this method the following equations and transformation temperatures were obtained:

For $\alpha \rightleftharpoons \beta$ (Ingot B-724)

$$T_H = 671.79 + 0.064\ \log_{10}r$$
$$T_C = 662.22 - 0.151\ \log_{10}r.$$

The two lines intersect at $T = 669.0°$ C and at $r = 2.4 \times 10^{-45°}$ C/min. This very slow rate is the result of the metal having been contained in a urania crucible, a procedure that was subsequently abandoned. Afterwards only bare specimens were used as shown in fig. 2.

For $\alpha \rightleftharpoons \beta$ (Ingot B-728T)

$$T_H = 673.96 + 4.19\ \log_{10}r$$
$$T_C = 659.61 - 3.76\ \log_{10}r.$$

The two lines intersect at $T = 666.4°$ C and at $r = 0.016°$ C/min. The mean of the two values is $667.7 \pm 1.3°$ C (fig. 4). The details of the measurements are given in table 3.

Baumrucker's mean value $666.8 \pm 0.4°$ C for heating agrees with this value within the limits of precision.

4.3.   THE BETA-GAMMA TRANSFORMATIONS

The same extrapolation method was used to determine the $\beta \rightleftharpoons \gamma$ transformation temperature (table 4). The two specimens (B-728T
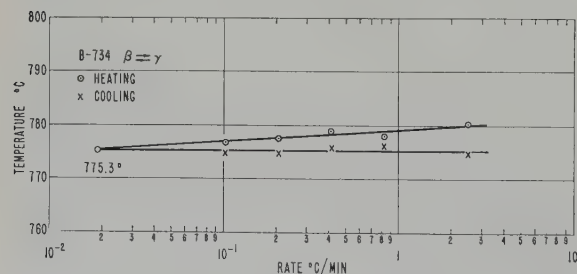

Fig. 5.   Effect of heating and cooling rate on the $\beta \rightleftharpoons \gamma$ transformation temperature of high-purity uranium (B-734).

and B-734) underwent superheating in a manner comparable to that observed for the $\alpha \rightarrow \beta$ transformation. The transformation temperatures on heating versus the logarithm of the rate may again be expressed by the relationship $T_H = a_1 + b_1 \log_{10} r$. The pertinent equations are:

B-728T . . . . . $T_H = 778.34 + 2.34\ \log_{10}r$

B-734   . . . . . $T_H = 779.11 + 2.19\ \log_{10}r$ (fig. 5).

TABLE 3

Mean $\alpha \rightleftharpoons \beta$ transformation temperatures of high purity uranium

Specimen No.	Rate (°C/min)	$\alpha \rightarrow \beta$		$\beta \rightarrow \alpha$	
		Temp. (°C)	No. of single meas.	Temp. (°C)	No. of single meas.
B-724	2.0	672.3	3	661.3	3
	1.0	671.7	9	662.1	9
	0.667	671.4	2	663.1	4
	0.50	671.5	2	663.0	2
B-728T	4.0	677.3	3	657.7	3
	2.0	675.7	8	658.5	8
	1.0	672.6	4	659.4	4
	0.50	671.6	3	660.0	2
	0.333	671.7	4	661.4	4
	0.167	672.1	2	663.1	2

TABLE 4

Mean $\beta \rightleftharpoons \gamma$ transformation temperatures of high purity uranium

Specimen No.	Rate (°C/min)	$\beta \rightarrow \gamma$		$\gamma \rightarrow \beta$	
		Temp. (°C)	No. of single meas.	Temp. (°C)	No. of single meas.
B-728T	2.47	780.2	3	774.7	3
	0.825	777.2	8	772.3	8
	0.412	777.1	3	777.6	3
	0.206	775.7	3	772.4	3
	0.103	777.3	3	775.0	3
B-734	2.47	780.3	4	774.9	4
	0.825	778.0	6	776.2	6
	0.412	779.0	3	775.8	3
	0.206	777.6	4	774.7	4
	0.103	776.9	3	774.8	3

No rate effect of the kind that was observed for the $\beta \to \alpha$ transformation took place on cooling although recalescence was noted in several, but not all, cycles. Thus, the cooling data are best represented by the mean of the observed values which graphically form a straight line parallel to the $\log_{10} r$ axis.

The intersection of the lines for heating and cooling and, therefore, the equilibrium transformation temperature is identical with the mean of the cooling curve data. They are:

$$\text{B-278T} \quad \ldots \ldots \quad T_C = 774.4 \pm 2.2^\circ \text{ C}$$

$$\text{B-734} \quad \ldots \ldots \quad T_C = 775.3 \pm 0.7^\circ \text{ C (fig. 5)}$$

The $\beta \rightleftharpoons \gamma$ transformation temperature of high purity uranium is $774.8 \pm 1.6^\circ$ C.

This temperature is 7° C higher than the mean of Baumrucker's cooling data, most of which were obtained at rates of 1.6° C/min and higher. It is possible that the tantalum thermocouple protection tube which was used by Baumrucker conducted enough heat away from the specimen to produce the lower value.

Similarly it is probable that heat transfer and heat conduction phenomena greatly influenced the measurements of Lloyd and account for the large difference even at comparable rates. On the other hand it is interesting to note that in the $\beta \to \alpha$ case when undercooling and recalescence are small and the insulating properties of the sleeve in the dilatometer had a favorable effect, the agreement between the dilatometric measurements of Lloyd and the present results is quite good.

4.4. THE BETA PHASE ANOMALY

The Beta phase anomaly encountered in the measurements of Duwez and Lloyd merits mention. A heat evolution was noted in the beta region on cooling. For the high purity specimens this occurred at temperatures ranging from 686° to 728° C, it also occurred in several of the runs made with impure materials. The phenomenon was characterized by a sudden increase in temperature resulting in a momentary slight expansion of the specimen, but with no change in the slope of the cooling curve. Other investigators have reported a break in the magnetic susceptibility curve of uranium at about 698° C.

In spite of a diligent search, no such anomaly was detected in the present thermal analyses. A similar search by Baumrucker also had negative results.

Since Blumenthal and Baumrucker used cast material of large grain size and Lloyd and Duwez fabricated material of much smaller grain size, it is possible that the effect is associated with the release of some strain energy introduced during the $\gamma \to \beta$ transformation. It is felt that the effect merits further investigation.

5. Conclusion

Because of the sensitivity of the solid state transformation to the rate at which measurements are made and because of the large effect which heat transfer and heat conduction phenomena have on the temperature measurements of all uranium transformations, only those measurements should be considered valid which take these factors into account. It is, therefore, felt that the present measurements and calculated transformation points come closest to true equilibrium conditions. The equilibrium transformation temperatures of high purity uranium are:

$$\alpha \rightleftharpoons \beta : \quad 667.7 \pm 1.3^\circ \text{ C}$$
$$\beta \rightleftharpoons \gamma : \quad 774.8 \pm 1.6^\circ \text{ C}$$
$$\gamma \rightleftharpoons \text{L} : 1132.3 \pm 0.8^\circ \text{ C}.$$

References

1) L. T. Katz and E. Rabinowitch, The Chemistry of Uranium. Part 1, Natl. Nucl. Energ. Series, Div. VIII, **5** (McGraw-Hill, New York, 1951) p. 149

2) J. Chipman, Metallurgy in the Development of Atomic Power. Manhattan District Declassified Document 539 (1946). (Office of Tech. Service U.S. Dept. of Commerce Wash. 25 D.C. USA)

3) S. E. Moore and K. K. Kelley, High Temperature Heat Contents of Uranium, Uranium Dioxide and Uranium Trioxide, J. Am. Chem. Soc. **69** (1947) 2105–2107

4) A. I. Dahl and M. S. Van Dusen, Resistance Temperature Relations and Thermoelectric Properties of Uranium, J. Research Natl. Bur. Std. **39** (1947) 53–58

5) D. C. Ginnings and R. J. Corruccini, Heat Capacities at High Temperatures of Uranium, Uranium Trichloride, and Uranium Tetrachloride J. Research Natl. Bur. Std. **39** (1947) 309–316

6) P. Gordon and A. R. Kaufmann, The Alloy Systems Uranium-Aluminium and Uranium-Iron Trans. A.I.M.E. **188** (1950) 182–194

7) J. D. Grogan, The Uranium-Iron System, J. Inst. Metal **77** (1950) 571–580

8) R. W. Buzzard, R. B. Liss and D. P. Fickle, Titanium-Uranium Alloy System in the Region from Zero to Thirty Atomic Percent Titanium, J. Research, Natl. Bur. Std. **50** (1953) 204–214

9) R. W. Buzzard, D. P. Fickle, and J. J. Park, The Silver-Uranium System, J. Research, Natl. Bur. Std. **52** (1954) 149–152

10) R. W. Buzzard and J. J. Park, The Gold-Uranium System, J. Research, Natl. Bur. Std. **53** (1954) 291–296

11) A. G. Knapton, The System Uranium-Titanium, J. Inst. Met. **83** (1954/55) 497–504

12) P. Chiotti, G. A. Tracy and H. A. Wilhelm, Magnesium-Uranium Alloy System, Trans. A.I.M.E. **206** (1956) 562–567

13) J. A. Catterall, J. D. Grogan and R. J. Pleasance, The System Uranium-Palladium, J. Inst. Metals **85** (1956/57) 63–67

14) P. Duwez, The Effect of the Rate of Cooling on the Allotropic Transformation Temperatures of Uranium, J. Appl. Physics **24** (1953) 153–156

15) A. I. Dahl and H. E. Cleaves, The Freezing Point of Uranium, J. Research, Natl. Bur. Std. **43** (1949) 513–518

16) C. Marzano and R. A. Noland, The Electrolytic Refining of Uranium, Argonne National Laboratory (USA) Report, ANL 5108 (1953)

17) B. Blumenthal, The Melting of High Purity Uranium, Trans. A.I.M.E. **203** (1955) 1199–1205

18) B. Blumenthal and R. A. Noland, High Purity Uranium, Progress in Nucl. Energy, Vol I, Series V (Pergamon Press, London, 1956) 62–80

19) B. Blumenthal, J. E. Baumrucker and L. T. Lloyd, The Transformation Temperatures of High Purity Uranium, Argonne National Laboratory (USA) Report, ANL 5957 (1959)

ATTACK OF GRAPHITE BY AN OXIDISING GAS AT LOW PARTIAL PRESSURES AND HIGH TEMPERATURES

J. E. ANTILL and K. A. PEAKALL

UKAEA *Atomic Energy Research Establishment, Harwell, Didcot, Berks., UK*

Experiments have been done to determine the kinetics of the oxidation of graphite at 900–1000° C in argon containing small amounts of oxygen, water vapour, carbon dioxide, hydrogen and carbon monoxide.

The reactivity of the gases decreased in the order oxygen, water vapour, carbon dioxide. The reaction rates increased with temperature and with the partial pressure of the oxidising gas, whilst hydrogen and carbon monoxide inhibited attack by water vapour and carbon dioxide respectively.

The relationships between the reaction rates and the partial pressures of the gases are in good agreement with theory, previous work and the supposition that hydrogen atoms are adsorbed on graphite in contact with hydrogen and water vapour.

———

Des expériences ont été réalisées pour déterminer la cinétique de l'oxidation du graphite à 900–1000° C dans de l'argon contenant de petites quantités d'oxygène, de vapeur d'eau, de gaz carbonique, d'hydrogène et d'oxyde de carbone.

La réactivité des gaz diminuait dans l'ordre oxygène, vapeur d'eau, gaz carbonique. Les vitesses de réaction croissaient avec la température et avec la pression partielle du gaz oxydant tandis que l'hydro-gène et l'oxyde de carbone inhibaient l'attaque par la vapeur d'eau et le gaz carbonique respectivement.

Les relations entre les vitesses de réaction et les pressions partielles des gaz sont en bon accord avec la théorie, les travaux antérieurs sur le sujet et aussi avec l'hypothèse d'une absorption des atomes d'hydrogène sur le graphite en contact avec l'hydrogène et la vapeur d'eau.

———

Die Kinetik der Oxydation von Graphit in Argon, dem kleine Mengen Sauerstoff, Wasserdampf, Kohlendioxyd, Wasserstoff und Kohlenmonoxyd zugesetzt waren, wurde bei 900–1000° C untersucht. Dabei wurde der Angriff bein Übergang von Sauerstoff auf Wasserdampf und dann auf Kohlendioxyd schwächer.

Die Reaktionsgeschwindigkeit stieg mit wachsender Temperatur und mit zunehmendem Partialdruck des oxydierenden Gases an. Wasserstoff und Kohlenmonoxyd hemmten den Angriff von Wasserdampf bzw. Kohlendioxyd.

Die Beziehung zwischen der Reaktionsgeschwindigkeit und dem Partialdruck der Gase steht in gutem Einklang mit theoretischen Vorstellungen, mit früheren Ergebnissen und mit der Annahme, dass bei Gegenwart von Wasserstoff und Wasserdampf Wasserstoffatome am Graphit absorbiert sind.

1. Introduction

The present design of the high temperature gas cooled reactor experiment to be built at Winfrith, England, has a graphite moderator and a fuel element of uranium and thorium carbides clad in a graphite can. The maximum temperature of the can is approximately 1000° C and the coolant is helium. Although the coolant is inert, compatibility problems exist as oxygen, carbon dioxide and water vapour, present as impurities, may react with the graphite to give carbon monoxide and hydrogen. The relevant literature has been summarised and out-of-pile experiments done to determine the kinetics of the attack of graphite, in an inert gas containing small amounts of reactive impurities.

Previous work on sorption and surface reactions has demonstrated the ability of carbon to retain oxygen atoms at certain active sites. Typical active sites are believed to be impurity atoms and the edges of graphitic planes. On an initially clean carbon surface oxygen atoms are adsorbed irreversibly from oxygen whilst carbon dioxide and water vapour are reduced

reversibly to carbon monoxide and hydrogen. These reactions may be expressed as

$$2C_t + O_2 \longrightarrow 2C_O$$

and

$$C_t + \frac{CO_2}{H_2O} \underset{k_2}{\overset{k_1}{\rightleftarrows}} C_O + \frac{CO}{H_2}, \qquad (1)$$
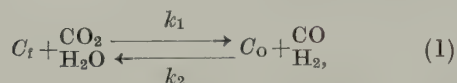
where C_t represents a free site and C_O a site possessing an oxygen atom. k_1 and k_2 are the relevant rate constants. Previous work indicates that even at temperatures as low as 600° C exchange reactions are fast.

Transfer of carbon to the gas phase may take place by the release of carbon monoxide from occupied sites and may be expressed as

$$C_O \overset{k_3}{\longrightarrow} CO + nC_t,$$
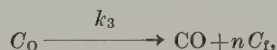
where n is an integer which normally has a value 1 but can be between 0 and 2 [1]).

The rate of loss of carbon (dm/dt) can be expressed as

$$\frac{dm}{dt} = k_3 (C_O) A, \qquad (2)$$

where (C_O) is the number of occupied sites per unit area and A is the available surface area.

Under steady state conditions the rate of formation of occupied sites will be equal to their disappearance.

$$\frac{d(C_O)}{dt} = k_1 p_O (C_t) - k_2 p_r(C_O) - k_3(C_O) = 0,$$

where p_O = the partial pressure of the oxidising gas i.e. O_2, CO_2, H_2O. p_r = the partial pressure of the reducing gas i.e. CO, H_2.

If C_t is the total number of reaction sites per unit area

$$(C_t) = (C_t) + (C_O)$$

and

$$(C_O) = \frac{k_1 p_O C_t}{k_1 p_O + k_2 p_r + k_3}. \qquad (3)$$

Substitution of equation (3) in (2) yields

$$\frac{dm}{dt} = \frac{k_3 k_1 p_O C_t A}{k_1 p_O + k_2 p_r + k_3} \qquad (4)$$

It follows that if the products are removed the steady rate of carbon loss will be proportional to the partial pressure of the oxidising gas if $k_1 p_O$ is small compared with $k_2 p_r + k_3$, and that the reciprocal of the reaction rate should be proportional to the partial pressure of carbon monoxide and hydrogen.

Although a vast amount of data has been published on the oxidation of coals, cokes, etc. little is applicable to the oxidation of a pure graphite at 1000° C in an inert gas containing small amounts of oxidising impurities. The most relevant work concerns the oxidation of pure carbon filaments in low partial pressures of oxygen, water vapour and carbon dioxide [2, 3, 4]). At most temperatures the reactivity of the gases decreases in the order oxygen, water vapour, carbon dioxide. The reactivity of graphite increases with temperature up to 1100–1400° C, and then steadily decreases to 1700° C due to the removal of active sites by an annealing process.

There is some confusion as to the effect of pressure and the order of the reactions but most workers are agreed that oxygen, water vapour and carbon dioxide behave similarly; the rates increase with pressure and the reactions are first order at 1200° C and zero order at 800–900° C. At the lower temperatures all the available active sites are therefore occupied and the dependence of the reaction rate upon chemical reactivity of the gas must be explained by differences in the activity and hence availability of sites. With a first order relationship the rates are directly proportional to pressure whilst with a zero order the gas penetrates the pores and the rates may depend upon pressure to a fractional powder.

The most reliable work appears to be that of Duval [2]) and Boulangier [3]) who interpreted their results from values for the ratio of number of gas molecules reacting to the number striking the carbon. The reaction rate (r) is related to this ratio (F) by the equation

$$r = 3.513 \times 10^{22} \frac{p}{\sqrt{MT}} \times F \text{ molecules/sec cm}^2$$

where p = partial pressure of the gas in mm Hg.

M = molecular weight of the gas

T = absolute temperature of the gas

r = number of gas molecules reacting/sec cm².

F was invariant with pressure at 1000° C for carbon dioxide and oxygen over the range 10^{-3}–10^{-2} mm Hg and therefore the rate was directly proportional to pressure and the reaction first order. The dependence of rate on water vapour pressure was complicated as F decreased with increasing pressure over the range 10^{-4}–10^{-2} mm Hg; the effect was explained by postulating the adsorption of hydrogen atoms on active sites.

Strickland-Constable [4] with 10^{-3}–10^{-1} mm Hg of water vapour and carbon dioxide obtained a fractional order reaction at 900–1100° C changing to first order at 1200° C.

Blyholder and others [5] showed that although the reaction with oxygen at pressures of 10^{-3}–10^{-1} mm Hg and temperatures of 800–900° C was zero order the reaction rate varied with pressure to the one half power due to appreciable diffusion of gas into the pores of the graphite.

Sabri Ergun [1] has demonstrated that carbon monoxide inhibits the attack of graphite by carbon dioxide and eq. (4) was found to explain the attack by CO–CO_2 gas mixtures at one atmosphere pressure over the temperature range 700–1400° C.

2. Experimental Procedure

Two sets of experiments have been done, in the first, rates of attack by 5–10 vpm oxygen, 0–1000 vpm water vapour and 0–500 vpm carbon dioxide in one atmosphere of argon were determined for three types of graphite at 900–1000° C; in the second the effects of 0–3000 vpm hydrogen on the oxidation by 300 vpm water vapour and of 0–5000 vpm carbon monoxide on the oxidation by 500 vpm carbon dioxide were determined for Pile Grade A graphite at 1000° C.

A conventional silica balance was used to measure rates of weight loss for the samples of graphite in a flowing stream of argon containing known amounts of the reactive gases. The graphite specimens were parallelepipeds $16 \times 5 \times 5$ mm; they weighed 700 mg and were suspended from the spring on a thin platinum wire. Great care was taken not to contaminate the graphite: the machining was done at a factory specialising in pile grade graphite and experimentalists always wore gloves when handling the specimens. Three different graphites were used in the experiments, namely Pile Grade A, EY9 (made by Morgan Crucible Co.) and EY9 which had been impregnated with a furfuryl alcohol resin and heat treated to approximately 1000° C to make it almost impervious to gas. They had densities between 1.7 and 1.8 g/cc. The gas was at atmospheric pressure and passed through the balance at 100–300 std. cc/min. The total burn-off during the course of the experiments varied between 20 and 150 mg, with the most reactive samples having the greatest burn-offs.

Argon sufficiently pure for all the experiments was obtained by passing the gas through manganous oxide at 150° C to lower the oxygen content to <1 vpm followed by anhydrous magnesium perchlorate to lower the water vapour content to <15 vpm. The oxides of carbon were added to the gas by passing it successively through heated beds of magnesium carbonate and graphite. Hydrogen was added by a conventional flowmeter technique, and water vapour by passing the argon-hydrogen mixture through a heated bed of cupric oxide or by passing a proportion of the main gas flow over a saturated solution of calcium chloride. When heated beds were used their temperature controlled the partial pressure of the additive. Experiments were only done with the 5–10 vpm of oxygen present as an impurity in cylinder argon and injection techniques were therefore not needed for this gas.

Oxygen was analysed by a Hersch meter, the oxides of carbon by an Infrared Gas Analyser and water vapour by an Electrolytic Water Analyser.

TABLE 1

Attack of graphite by gaseous impurities

Material	Temp. °C	Impurity conc: vpm					Rate of weight loss mg/cm² h	Flowrate (std. cc/min)
		O_2	CO_2	H_2O	CO	H_2		
Pile Grade A	1000	5–10	< 10	< 15			0.06 ± 0.002	150
EY9	1000	5–10	< 10	< 15			0.025 ± 0.002	75
EY9	1000	5–10	< 10	< 15			0.039 ± 0.002	300
EY9	1000	< 1	< 10	< 15			0.003 ± 0.002	
EY9	1000	< 1	< 10	420			0.20 ± 0.002	
EY9	1000	< 1	< 10	720			0.43 ± 0.002	
EY9 impregnated	1000	< 1	< 10	< 15			0.003 ± 0.002	
EY9 impregnated	1000	< 1	< 10	76			0.027 ± 0.002	
EY9 impregnated	1000	< 1	< 10	167			0.11 ± 0.002	
EY9 impregnated	1000	< 1	< 10	315			0.26 ± 0.002	
EY9 impregnated	1000	< 1	< 10	545			0.51 ± 0.002	
Pile Grade A	1000	< 1	< 10	< 15			0.003 ± 0.002	
Pile Grade A	1000	< 1	< 10	75			0.023 ± 0.002	
Pile Grade A	1000	< 1	< 10	238			0.117 ± 0.002	
Pile Grade A	1000	< 1	< 10	508			0.234 ± 0.002	
Pile Grade A	900	< 1	< 10	< 15			0.003 ± 0.002	
Pile Grade A	900	< 1	< 10	103			0.011 ± 0.002	
Pile Grade A	900	< 1	< 10	250			0.034 ± 0.002	
Pile Grade A	900	< 1	< 10	363			0.052 ± 0.002	
Pile Grade A	900	< 1	< 10	654			0.096 ± 0.002	
Pile Grade A	900	< 1	< 10	955			0.11 ± 0.002	
Pile Grade A	1000	< 1	< 10	< 15			0.003 ± 0.002	
Pile Grade A	1000	< 1	250	< 15			0.014 ± 0.002	
Pile Grade A	1000	< 1	500	< 15			0.024 ± 0.002	
EY9	1000	< 1	< 10	< 15			< 0.001	
EY9	1000	< 1	260	< 15			0.047 ± 0.002	
EY9	1000	< 1	530	< 15			0.136 ± 0.002	
Pile Grade A	900	< 1	< 10	< 15			< 0.002	
Pile Grade A	900	< 1	270	< 15			0.004 ± 0.002	
Pile Grade A	900	< 1	500	< 15			0.009 ± 0.002	
Pile Grade A	1000	< 1	500	< 15	250	—	0.018 ± 0.002	
Pile Grade A	1000	< 1	500	< 15	500	—	0.014 ± 0.002	
Pile Grade A	1000	< 1	500	< 15	5000	—	0.004 ± 0.002	
Pile Grade A	1000	< 1	< 10	300	—	300	0.067 ± 0.002	
Pile Grade A	1000	< 1	< 10	300	—	750	0.044 ± 0.002	
Pile Grade A	1000	< 1	< 10	300	—	1500	0.021 ± 0.002	
Pile Grade A	1000	< 1	< 10	300	—	2100	0.013 ± 0.002	
Pile Grade A	1000	< 1	< 10	300	—	3000	0.007 ± 0.002	

3. Results

A visual examination of the specimens indicated that most of the attack took place at the geometric surface, although the pores of the Pile Grade A specimens were slightly enlarged.

The weight loss-time graphs were linear for a given set of experimental conditions and the reaction rates obtained with the various gas compositions are summarised in table 1. The relations between reaction rate and impurity concentration for water vapour and carbon dioxide together with the effects of hydrogen and carbon monoxide are shown in figs. 1–4.

Although the attack by carbon dioxide and water vapour was independent of flowrate, the
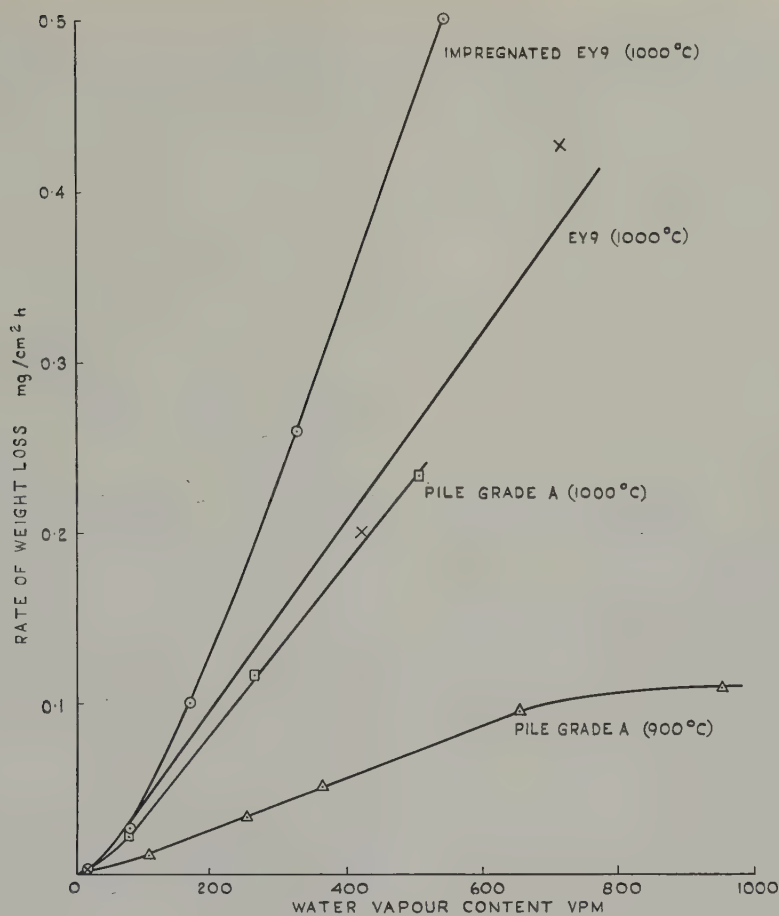
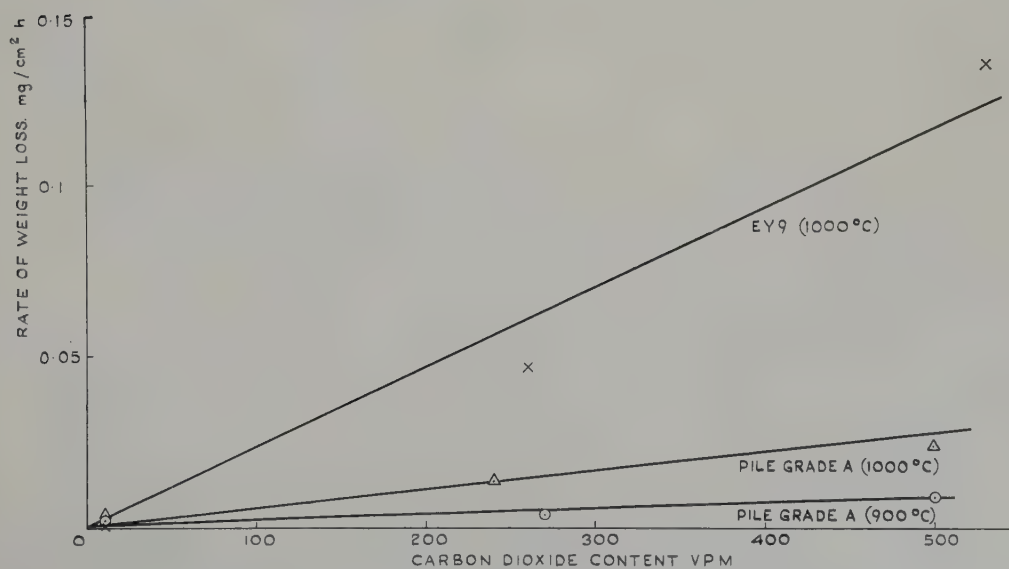Fig. 1. Attack of graphite in argon containing water vapour.

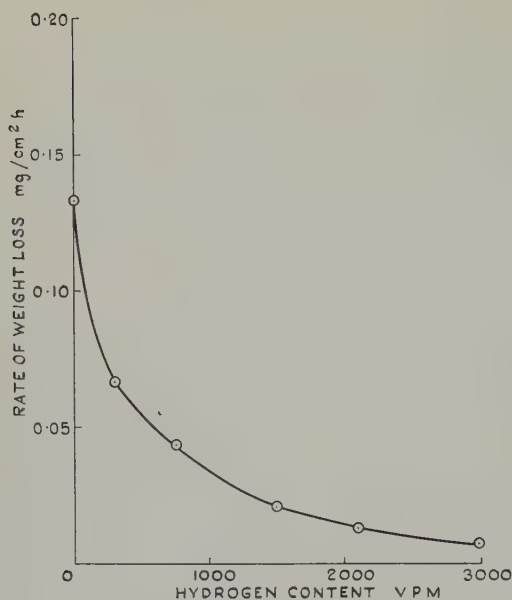Fig. 2. Attack of graphite in argon containing carbon dioxide.

Fig. 3.   Effect of hydrogen on attack of Pile Grade A by 300 vpm water vapour at 1000° C.
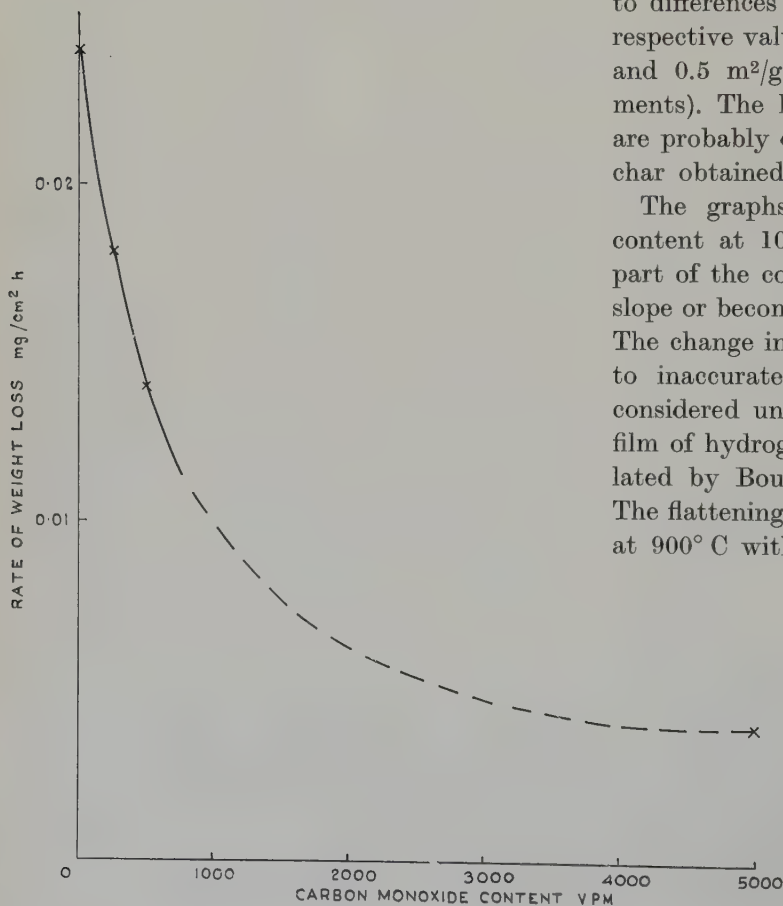
rates for gas containing 5–10 vpm oxygen varied with flowrate and corresponded to all or a large proportion of the impurity reacting, and were therefore controlled by the oxygen supply.

4.   Discussion

All the results are consistent with theory and previous work in so far as the reactivity of the impurities decreased in the order oxygen, water vapour, carbon dioxide, and the rates increased with temperature and the partial pressure of the oxidising gas, whilst hydrogen and carbon monoxide inhibited the attack.

The reactivity of the different graphites decreased in the order: impregnated EY9, EY9 and Pile Grade A. From considerations of the methods of manufacture, the difference between EY9 and Pile Grade A is most likely due to impurities in the EY9, although it could be explained by differences in surface roughness due to differences in the internal surface area, the respective values of the internal area being 3–5 and 0.5 m²/g (according to B.E.T. measurements). The high rates for impregnated EY9 are probably due to the reactive nature of the char obtained from furfuryl alcohol.

The graphs of rate versus water vapour content at 1000° C are linear for the greater part of the concentration range but change in slope or become curved in the range 0–70 vpm. The change in slope or curvature could be due to inaccurate gas analysis although this is considered unlikely; it is best explained by a film of hydrogen atoms, similar to that postulated by Boulangier [3]), inhibiting the attack. The flattening off of the graph for Pile Grade A at 900° C with high water vapour contents is

Fig. 4.   Effect of carbon monoxide on attack of Pile Grade A by 500 vpm carbon dioxide at 1000° C.

indicative of a zero order reaction and penetration into the pores.

With carbon dioxide at 900–1000° C the rate appears to be directly proportional to partial pressure although the results cannot be considered sufficiently accurate to prove that a fractional order relationship does not hold.

A comparison between the rates of attack in the present and previous work may be made if it is assumed that the reactions are first order and little affected by the inert gas. The partial pressures in the experiments of Duval, Boulangier, etc. correspond to an impurity concentration of 5–10 vpm in a carrier gas at one atmosphere pressure and therefore if the rates for water vapour and carbon dioxide are linearly extrapolated through the origin a comparison may be made for the higher impurity concentrations used in the present work. An examination of table 2 reveals no outstanding discrepancy between the various sets of data.

The theoretical reasoning leading to eq. (4) predicts that the reciprocal of the reaction rate should be proportional to the partial pressure of the reducing gas. The accuracy of the results for the CO_2–CO additions is not sufficiently good to prove the relationship but an indication of the validity of eq.(4) may be obtained for the H_2O–H_2 additions. The reciprocal of the rate for 300 vpm water vapour is plotted against

the hydrogen concentration in fig. 5; the graph is not linear but curved upwards indicating that hydrogen has a greater effect than theory predicts. It can be shown that with the exception of the rate for 300 vpm hydrogen the results satisfy an equation of the form:

$$\frac{1}{\text{rate}} = A p_r^{1.53} + C$$
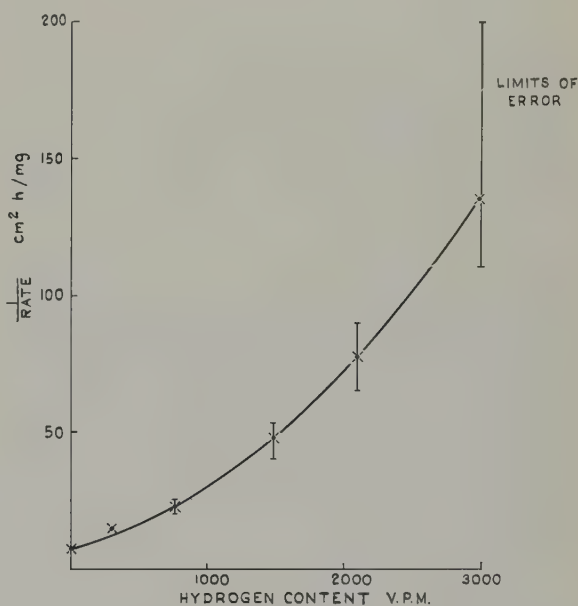
where A and C are constants.

Fig. 5. Effect of hydrogen on the reciprocal of the reaction rate for the attack of Pile Grade A by 300 vpm water vapour at 1000° C.

TABLE 2

Comparison of rates at 1000° C

Work	Impurity	Rate of attack		Rate corresponding to 100 vpm mg/cm² h
		weight loss mg/cm² h	impurity content vpm	
Boulangier [3])	CO_2	8×10^{-5}	10	8×10^{-4}
Strickland–Constable [4])	CO_2	$\approx 1.1 \times 10^{-4}$	10	$\approx 1.1 \times 10^{-3}$
Pile Grade A	CO_2	—	—	4×10^{-3}
Boulangier [3])	H_2O	4×10^{-4}	10	4×10^{-3}
Strickland–Constable [4])	H_2O	$\approx 8 \times 10^{-3}$	10	$\approx 8 \times 10^{-2}$
Blyholder [6])	H_2O	5×10^{-2}	100	5×10^{-1}
Pile Grade A	H_2O	—	—	2×10^{-2}
Duval [2])	O_2	0.77	10	
Pile Grade A	O_2	$\geqslant 0.06$	5–10	

The greater dependence on the partial pressure of hydrogen is consistent with the adsorption of hydrogen atoms on active sites and the replacement of reaction (1) by

$$C_H + H_2O \longleftrightarrow C_O + \tfrac{3}{2} H_2,$$

where C_H is a reaction site possessing a hydrogen atom. It is therefore in accord with the results for water vapour alone and the work of Boulangier [3]).

It follows that eq. (4) may still be valid for CO_2–CO additions as the reaction rate appeared to be directly proportional to concentration over the whole range 0–500 vpm for carbon dioxide alone (fig. 2) and Boulangier found the efficiency of collision (F) independent of the partial pressure of carbon dioxide.

These out of pile results provide a sound basis on which to conduct in pile experiments and indicate the relationships between gas composition and attack of graphite in a high temperature gas cooled reactor. They should be directly applicable to a zero energy assembly but can only be used tentatively for a power reactor, as irradiation may activate the impurities.

5. Conclusions

The reactivity of the gaseous impurities which may be present in a high temperature gas cooled reactor decreases in the order oxygen, water vapour, carbon dioxide. The reaction rates increase with temperature up to 1000° C and with the partial pressure of the oxidising gas, whilst hydrogen and carbon monoxide inhibit the attack.

The relationships between the reaction rates and the partial pressures of water vapour, carbon dioxide, hydrogen and carbon monoxide are in good agreement with theory, previous work and the supposition that hydrogen atoms are adsorbed on graphite in contact with hydrogen and water vapour.

References

[1]) Sabri Ergun, J. Phys. Chem. **60** (1956) 480
[2]) X. Duval, Ann. de Chimie **10** (1955) 903
[3]) F. Boulangier, Thesis, Université de Nancy (July 1956)
[4]) R. F. Strickland–Constable, Trans. Faraday Soc. **43** (1949) 769
[5]) G. Blyholder *et al.*, J. Phys. Chem. **61** (1957) 682
[6]) G. Blyholder and H. Eyring, J. Phys. Chem. **63** (1959) 693

AN EXPERIMENTAL DETERMINATION OF THE CHARACTERISTIC TEMPERATURE
FOR PuO₂ †, ††

R. B. ROOF Jr.

Los Alamos Scientific Laboratory, University of California, Los Alamos, New Mexico, USA

Received 15 October 1959

The characteristic temperature for PuO_2 has been determined by experimentally measuring the reduction in intensity of X-ray diffraction spectra from a specimen as the specimen temperature is increased. In order to evaluate the technique employed, the characteristic temperature of aluminium was also determined.

For aluminium, a characteristic temperature of 393° K was obtained, which agrees very well with the value of 390° K obtained from specific heat measurements. The characteristic temperature of PuO_2 was found to be 415° K.

———

La température caractéristique de PuO_2 a été déterminée en mesurant expérimentalement l'abaissement d'intensité du spectre de diffraction aux rayons X en fonction de l'élévation de température pour un échantillon donné.

Parallèlement la température caractéristique de l'aluminium a aussi été déterminée afin de pouvoir

apprécier les techniques employées. Par cette méthode, on obtient une température caractéristique de 393° K pour l'aluminium ce qui concorde bien avec la valeur de 390° K obtenue par la mesure de la chaleur spécifique. On a trouvé une température caractéristique de 415° K pour PuO_2.

———

Es wurde die charakteristische Temperatur von PuO_2 bestimmt, indem bei steigender Probentemperatur die Abnahme der Intensität von Röntgenbeugungsbildern gemessen wurde. Um die angewendeten Untersuchungsmethoden zu überprüfen, wurde zusätzlich noch die charakteristische Temperatur von Aluminium ermittelt.

Die für Aluminium festgestellte charakteristische Temperatur von 393° K stimmt sehr gut mit dem Wert von 390° K überein, welcher bei Messungen der spezifischen Wärme gewonnen wurde. Die charakteristische Temperatur von PuO_2 ergab sich zu 415° K.

1. Introduction

When discussing the thermal properties of crystal lattices it is convenient to use the Debye–Waller theory for correlating various thermal data. According to this theory the thermal properties of a crystal lattice are associated with a single parameter, i.e. a characteristic temperature, Θ, which, when substituted into the appropriate formulas, allows the specific heat of different substances to be correlated with a common curve.

This paper is concerned with the determination of the characteristic temperature for PuO_2 through measuring the reduction in intensity of X-ray diffraction spectra from a

specimen as the specimen temperature is increased. In order to evaluate the techniques employed, the characteristic temperature of aluminium was also determined.

2. Theory

In the following discussion let the temperature T_1 be greater than the temperature T_2. Then it follows for B, a quantity related to the average lattice vibration, that B_1 is greater than B_2. The intensity, I, of an X-ray reflection is related to B in the following manner

$$I \sim \exp\left(-2B \sin^2 \theta / \lambda^2\right) \qquad (1)$$

where θ is the Bragg angle of diffraction and

---

† Work done under the auspices of the U. S. Atomic Energy Commission.
†† A portion of this paper was presented at the 17th Pittsburgh Diffraction Conference, November, 1959.

λ is the wavelength of the X-rays employed. By taking, for a given reflection, the ratio of the intensities at two different temperatures, eq. (2) is obtained:

$$I_2/I_1 = a \exp \left(2(B_1 - B_2) \sin^2 \theta/\lambda^2 \right). \qquad (2)$$

According to the Debye–Waller theory the quantity B is related to the characteristic temperature, Θ, by

$$B = 6h^2 T(\phi(x) + \tfrac{1}{4}x)/mk\Theta^2 \qquad (3)$$

where

$h =$ Planck's constant, 6.6252×10^{-27} erg sec,
$m =$ average mass of a lattice point, g,
$k =$ Boltzmann's constant,
$\qquad\qquad 1.3804 \times 10^{-16}$ erg deg^{-1},
$T =$ absolute temperature, °K,
$x = \Theta/T$, and
$\phi(x) =$ Debye function.

Assuming that Θ does not change in the temperature interval T_2 to T_1 then from eq. (3) if follows that

$$\Theta^2 = \left\{ \frac{6h^2[T_1(\phi\tfrac{1}{4}x_1 + \tfrac{1}{4}x) - T_2(\phi\tfrac{1}{4}x_2 + \tfrac{1}{4}x_2)]}{mk(B_1 - B_2)} \right\}. \quad (4)$$

Thus, the value of $(B_1 - B_2)$, obtained from experimentally determined intensity ratios according to eq. (2), when inserted in eq. (4) allows the characteristic temperature of a substance to be calculated.

In the Debye–Waller theory it is assumed that the volume of the crystal remains constant as the temperature changes. In actual practice the pressure remains constant and the volume changes as a result of thermal expansion. Consequently, if Θ is plotted as a function of the average temperature of the temperature interval T_2 to T_1, a curve is obtained which exhibits negative curvature as the average temperature increases. In order to obtain a single parameter for the material, the true characteristic temperature, a correction must be applied to eliminate this high temperature curvature.

This correction for high temperature curvature is made in the following manner. Again,

let T_1 be greater than T_2, but also restrict T_1 and T_2 to values in the neighbourhood of, or greater than Θ. In this region the value of the function $(\phi(x) + \tfrac{1}{4}x)$ of eq. (3) does not differ appreciably from 1.00 and, therefore, to the first approximation this function may be neglected. Then from eq. (3)

$$B_1 = 6h^2 T_1/mk\Theta_1^2 \qquad (5)$$

and

$$B_2 = 6h^2 T_2/mk\Theta_2^2. \qquad (6)$$

Paskin [1], using thermodynamic reasoning, has derived the expression

$$\Theta_1/\Theta_2 = (V_2/V_1)^\gamma \qquad (7)$$

where V is the volume of the crystal at the appropriate temperature and γ is the Grüneisen constant, which is equal to $V\beta/C_v k$ where V is volume; β, the coefficient of volume expansion; C_v, specific heat at constant volume; and k, the compressibility. By substituting eq. (7) in eq. (5), eq. (8) is obtained.

$$B_1 = \frac{6h^2 T_1}{mk\Theta_2^2} \left(\frac{V_1}{V_2} \right)^{2\gamma}. \qquad (8)$$

By subtracting eq. (6) from eq. (8) and rearranging, eq. (9) is obtained.

$$\Theta_2^2 = \left\{ \frac{6h^2[T_1(V_1/V_2)^{2\gamma} - T_2]}{mk(B_1 - B_2)} \right\}. \qquad (9)$$

A comparison of eq. (4) (Debye) with eq. (9) (Paskin) shows that these two equations for computing a characteristic temperature of a material are similar. The Paskin equation, however, takes into consideration the thermal expansion of the crystal and thus provides for a more practical experimental determination of the characteristic temperature.

3. Experimental Procedure

The experimental samples consisted of pressed and sintered disks approximately 0.5 in. in dia. by 0.030 in. thick. The samples were placed in a tantalum holder which in turn was inserted into a high temperature, high vacuum furnace mounted on a General Electric XRD-3 X-ray diffractometer. A more complete description of

this furnace and vacuum system is available elsewhere [2]). Cu Kα X-rays were used and the intensity data were obtained by means of a standard General Electric SPG No. 2 Detector utilizing an argon-filled proportional counter tube. Pulse height analysis was used to discriminate against unwanted radiation.

Because of the normal day-to-day random variations in X-ray tube output, counter tube efficiency, electronic stability, etc., the intensity data gathered at various temperatures and inserted in eq. (2) may not always result in a value of 1.00 for the quantity a. Since a has no effect on the desired experimental quantity $B_1 - B_2$, its value may be adjusted as a computational convenience. Consequently, the raw intensity data obtained at various temperatures have been normalized to the data obtained at the highest temperature reached by a given specimen. The normalized data are given in the Tables in the following section.

The intensity ratios obtained at various temperatures were least-squares fitted to eq. (2) by utilizing an iterative procedure [3]) on an IBM 704 computer. This procedure allows the quantity $(B_1 - B_2)$ of eq. (2) and its standard deviation to be calculated simultaneously.

4. Experimental Results

4.1. ALUMINIUM

The experimental data for aluminium are given in table 1.

TABLE 1

Relative integrated intensities for aluminium
(Normalized to 318° C)

hkl	18° C	136° C	212° C	318° C
111	2967	2896	2815	2705
200	1502	1451	1401	1334
220	866	804	758	701
311	908	808	747	667
222	241	216	195	171
400	72	62	55	46
331	337	282	242	197
420	379	304	262	211
422	416	328	272	208

Average limit of error on intensity measurements ± 2.0 %.

The values of $(B_1 - B_2)$ given in table 2 were obtained by substituting intensity ratios determined from the data of table 1 into eq. (2).

TABLE 2

Experimental values of $(B_1 - B_2)$ for aluminium

Temperature interval (°C)	$(B_1 - B_2) \times 10^{-16}$ cm^2
18–136	0.3618 ± 0.0169
136–212	0.2463 ± 0.0089
212–318	0.3603 ± 0.0103

The characteristic temperature, Θ, determined from the values of $(B_1 - B_2)$ of table 2, when substituted into the Debye (eq. (4)) or Paskin (eq. (9)) equations is given in table 3.

TABLE 3

Characteristic temperature, Θ, for aluminium as determined from the Debye and Paskin equations

Temperature interval (° C)	Debye (° K)	Temperature (° C)	Paskin (° K)
18–136	367 ± 18	18	393 ± 20
136–212	358 ± 10	136	394 ± 10
212–318	351 ± 11	212	393 ± 13

For use in Paskin's equation, the volumes were determined by cubing the lattice constants. The lattice constant was determined as a function of temperature by noting the Bragg angle of the 422 reflection while intensity measurements were being taken. The Grüneisen constant for aluminium is 2.17, taken from the work of Slater [4]). The value of 393° K thus obtained for the characteristic temperature of aluminium agrees very well with the value of 390° K obtained from specific heat measurements [5]).

4.2. PLUTONIUM DIOXIDE

The experimental intensity data for PuO$_2$ are given in table 4.

The values of $(B_1 - B_2)$ are given in table 5 and were obtained by substituting into eq. (2) the intensity ratios determined from the data of table 4.

The characteristic temperature, Θ, determined from the values of $(B_1 - B_2)$ of table 5 when

substituted into the Debye (eq. (4)) or Paskin (eq. (9)) equations, is given in table 6.

TABLE 4

Relative integrated intensities for PuO_2
(normalized to 617° C)

hkl	16° C	196° C	342° C	474° C	617° C
200	1048	1039	1030	1024	1013
311	1102	1072	1050	1024	1000
400	214	206	200	194	187
420	—	330	—	306	292
333	525	491	464	442	410
531	—	498	—	437	408
620	440	400	371	345	315
622	470	425	389	358	323

Average limit or error on intensity measurements ± 1.8 %.

TABLE 5

Experimental values of $(B_1—B_2)$ for PuO_2

Temperature interval (°C)	$(B_1—B_2) \times 10^{-16}$ cm^2
16–196	0.1351 ± 0.0039
196–342	0.1148 ± 0.0046
343–474	0.1090 ± 0.0025
474–617	0.1302 ± 0.0113

For use in Paskin's equation the volumes were determined by cubing the lattice constant. The lattice constant was determined as a

TABLE 6

Characteristic temperature, Θ, for PuO_2 as determined from the Debye and Paskin equations

Temperature interval (° C)	Debye (° K)	Temperature (° C)	Paskin (° K)
16–196	403 ± 8	16	414 ± 9
196–342	397 ± 11	196	416 ± 11
342–474	388 ± 6	342	416 ± 7
474–617	376 ± 14	474	414 ± 13

function of temperature by noting the Bragg angle of the 622 reflection while intensity measurements were being taken. The Grüneisen constant for PuO_2 is empirically 2.6, this value being required in order to remove the high temperature curvature of the Debye characteristic temperature. The characteristic temperature of PuO_2 was thus found to be 415° K.

References

[1] A. Paskin, Acta Cryst. 10 (1957) 667
[2] R. O. Elliott, thesis, University of California (1958)
[3] R. H. Moore and R. K. Zeigler, Proceedings of the American Nuclear Society, Winter Meeting (Detroit, Dec. 10, 1958)
[4] J. C. Slater, Introduction to Chemical Physics (McGraw-Hill, New York, 1939)
[5] R. W. James, The Optical Principles of the Diffraction of X-rays (G. Bell and Sons Ltd., London, 1948)

STRAHLUNGSWACHSTUM VON α-URAN ALS ERGEBNIS KORRELATIVER STOSSPROZESSE

ULRICH GONSER

Institut für Reaktorwerkstoffe der Gesellschaft zur Förderung der kernphysikalischen Forschung, Aachen, Deutsche Bundesrepublik

Das Modell der korrelativen Stossprozesse eignet sich für die Deutung des Strahlungswachstums von α-Uran und der damit in Verbindung stehenden Erscheinungen. In der Umgebung eines durch Spaltung hervorgerufenen Störbereiches (Fission Spike) treten in den 3 kristallographischen Hauptrichtungen folgende Prozesse bevorzugt auf:

[100] — Fokusonen;
[010] — Dynamische Crowdions;
[001] — Hohe Dichte an Frenkelpaaren.

Der bei höheren Temperaturen beobachtete Übergang vom anisotropen Strahlungswachstum zur isotropen Strahlungsschwellung ergibt sich aus der Defokussierung der korrelativen Stossprozesse.

Die Korngrössenabhängigkeit und die Möglichkeiten der Verminderung des Strahlungswachstums werden diskutiert. Auf die bisher entwickelten Modelle (Spike und Diffusion) wird hingewiesen.

The correlated collision model is apt for the interpretation of the irradiation-induced growth of α-uranium, and phenomena associated therewith. In the neighbourhood of a fission spike the following processes occur preferentially in the three principal crystallographic directions:

[100] — focusons;
[010] — dynamic crowdions;
[001] — high concentration of Frenkel pairs.

The transition from anisotropic growth to isotropic swelling under irradiation, as observed at elevated temperatures, is a consequence of the loss of focusing of the correlated collisions.

The grain size dependence of irradiation-induced growth, and the possibility of reducing it, are discussed. The existing models of growth (spike and diffusion models) are considered.

Le modèle des processus de choc corrélatifs se prête bien à l'explication de la croissance sous irradiation de l'uranium α et des phénomènes qui s'y rattachent. Au voisinage d'un domaine perturbé préférentiellement par une fission (pointe de fission), les processus suivants prennent naissance préférentiellement suivant les 3 directions cristallographiques:

[100] — Focusons;
[010] — Crowdions dynamiques;
[001] — Densité élevée de paires de Frenkel.

Le passage observé, aux plus hautes températures de la croissance sous irradiation, au gonflement isotrope sous irradiation provient de la défocalisation des processus de choc corrélatifs.

La relation entre croissance et dimensions des grains ainsi que les possibilités de diminuer la croissance sous irradiation sont discutées, ainsi que les modèles développés jusqu'ici (pointe de fission, diffusion).

1. Einleitung

Uran, der wichtigste Brennstoff der heutigen Reaktoren, erfährt unter Bestrahlung vielseitige Änderungen seiner mechanischen und physikalischen Eigenschaften. Die auffallendste Erscheinung ist seine Forminstabilität, welche sich in Längen-, Oberflächen- und Dichteänderungen deutlich ausdrückt. Die unmittelbare Bedeutung dieser Forminstabilität für die Reaktorentwicklung und -technik waren in den letzten Jahren Anlass für umfassende Forschungsarbeiten auf diesem Gebiete in allen beteiligten Ländern, besonders in den USA, in England und in Russland. Anlässlich der beiden Genfer Konferenzen zur friedlichen Ausnutzung der Atomenergie (1955 und 1958) sind die Ergebnisse zusammenfassend vorgetragen worden.

2. Forminstabilität des α-Urans

Bei Bestrahlung von Uranproben lassen sich 3 Erscheinungen der Forminstabilität unterscheiden:

2.1. STRAHLUNGSWACHSTUM (GROWTH)

Turkalo [1]) und Paine und Kittel [2]) zeigten, dass Einkristalle von α-Uran eine Ausdehnung in [010]-Richtung und eine Schrumpfung in [100]-Richtung erfahren. In [001]-Richtung tritt kaum eine Längenänderung ein. In polykristallinem Uran entspricht das Strahlungswachstum der vorhandenen Textur. Für kleine Längenänderungen ist das Strahlungswachstum proportional der "Verbrennung" (burn-up). Als sein Mass wird eine Wachstumsgrösse G_i definiert

$$G_i = \frac{\left[\dfrac{\Delta e}{e}\right]_{[010]}}{\dfrac{\text{Spaltprozesse}}{\text{Anzahl der Uranatome}}}.$$

Sie hängt sehr von der Textur und der Temperatur bei der Bestrahlung ab. Die Ergebnisse von Paine und Kittel [2]) für α-Uraneinkristalle sind in Tabelle 1 wiedergegeben.

TABELLE 1
(nach Paine und Kittel [2]))

Richtung	Strahlungswachstumskoeffizient G_i	Thermischer Ausdehnungskoeffizient α (25–125° C)
[100]	— 420 ± 20	+ 21,7 × 10⁻⁶
[010]	+ 420 ± 20	— 1,5 × 10⁻⁶
[001]	0 ± 20	+ 23,2 × 10⁻⁶

2.2. STRAHLUNGSSCHWELLUNG (SWELLING)

Bei höheren Bestrahlungstemperaturen (oberhalb 400° C) tritt an die Stelle des anisotropen Strahlungswachstums eine isotrope Ausdehnung, die nicht nur auf die α-Phase des Urans beschränkt bleibt. Sie ist weitgehend unabhängig von der Vorgeschichte der Proben. Unter dem Mikroskop erkennt man eine Porenbildung. Der Gitterparameter bleibt jedoch annähernd unverändert.

2.3. STRAHLUNGSRUNZELN (WRINKLING)

An Oberflächen grobkristalliner, ursprünglich glatter Proben zeigen sich nach Bestrahlung Runzeln. Ihre Bildung hängt deutlich erkennbar mit der Kornstruktur der Proben zusammen. Die Runzeln wird man daher als eine Folgeerscheinung des Strahlungswachstums ansehen können. Einige Körner rufen durch ihre bevorzugte Lage an der Oberfläche stärkere Wachstumserscheinungen hervor als andere, die in ihrem Wachstum gehemmt sind.

3. Korrelative Stossprozesse (Correlated Collisions)

Die experimentellen und theoretischen Arbeiten über die Strahlenschädigung (Radiation Damage) in Festkörpern führten zu der Vorstellung, dass ein Atom aus seinem Gitterplatz herausgestossen wird, wenn bei dem Stoss eine Mindestenergie (Threshold Displacement Energy; $E_d \approx 25$ eV) übertragen wird. Erhält das primär herausgeschlagene Atom (Primary Knock-on) bei dem Stossprozess eine hohe Energie, so können kaskadenartig sekundäre, tertiäre usw. Atome aus dem Gitterverband gelöst werden. Im Energiebereich von etwa 10⁴ eV liegt nach den Arbeiten von Brinkman [3]) für viele Materialien die Stossfolge in der Grössenordnung der atomaren Abstände. Die resultierenden Bereiche hoher Unordnung (Displacement Spike) sind mit dem Schmelzzustand verglichen worden. Silsbee [4]) wies zuerst darauf hin, dass durch die Anordnung der Atome im Gitter die Stossprozesse in korrelativer Weise in bestimmten Richtungen erfolgen. Nach seinen Vorstellungen wird deutlich, dass nicht allein die mittlere freie Weglänge der primär herausgestossenen Atome den Schädigungsbereich charakterisiert, sondern dass korrelative Stossprozesse die Störung aus dem Zentralbereich weit in das Gitter hineintragen. Thompson [5]) zeigte, dass bei Protonen-Bestrahlung von Goldfolien eine Emission von Goldatomen in Richtung dicht-gepackter Reihen erfolgt. Dieses Experiment muss als eine Verifizierung des Modells von Silsbee angesehen werden. Durch neuere Arbeiten von Leibfried [6])

und Vineyard [7]) werden diese Ideen erweitert und verfeinert.

Nach Leibfried sind bei den weitreichenden Effekten der korrelativen Stossprozesse zwei Möglichkeiten für das Gitter zu unterscheiden:

1) Fokussierende Stossprozesse (Focusing Collisions)

Sie werden dadurch charakterisiert, dass lediglich Energie übertragen wird, aber kein Transport von Zwischengitteratomen erfolgt. Für diese Art von Stossprozessen schlägt Leibfried den Namen "Fokusonen" (Focusons) vor.

2) Crowdion-Stossprozesse (Crowdion Collisions)

Ein Crowdion entsteht dadurch, dass eine Atomreihe auf kurzer Strecke ein Atom mehr aufnimmt, als der idealen Gitterbesetzung entspricht. Als "dynamisches Crowdion" wandert diese Struktur längs ihrer Gittergeraden. Als "statisches Crowdion" ist diese Struktur wahrscheinlich nicht beständig; vielmehr geht das damit gekoppelte anisotrope Verschiebungsfeld in das Kubisch-symmetrische eines Zwischengitteratoms über. Das Crowdion stellt demnach einen kurzlebigen Gitterfehler dar.

Bei der Behandlung der korrelativen Stossprozesse wird das steile Potential zwischen zwei Atomen im Gitter durch ein hartes Kugel-Potential ersetzt, wobei der Radius der als starr zu betrachtenden Kugeln ($\frac{1}{2}R$) mit abnehmender kinetischer Energie E des bewegten Atoms anwächst.

Fokussierende Stösse sind nach Abb. 1 † dann zu erwarten, wenn $R > \frac{1}{2}D_F$ ist. D_F ist der Abstand zweier Atome in Richtung dichtgepackter Atomreihen. Der Stosspunkt P_F liegt näher an der Gleichgewichtslage des stossenden Atoms. Dadurch wird bei jedem Stoss der Winkel zur dicht-gepackten Atomreihe kleiner,

† Es soll darauf hingewiesen werden, dass in der Darstellung die Atome mit doppeltem harten Kugelradius gezeichnet wurden. Dadurch werden die Stossverhältnisse anschaulich, besonders die Unterscheidung von Fokuson und Crowdion.
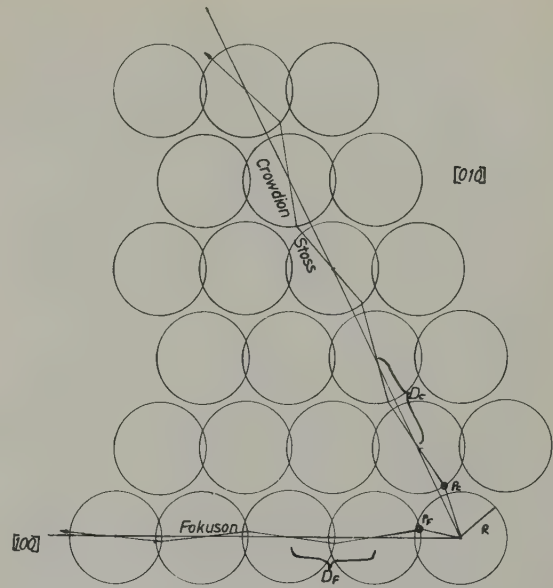

Abb. 1. a-b-Ebene des α-Urans mit Darstellung von Crowdion Stoss und Fokuson.

und es tritt eine Fokussierung in diese Richtung ein. Da R eine Funktion von E ist, sollte sich nach dieser Vorstellung eine maximale Energie E_F für das Einsetzen der Fokussierungs-Stösse angeben lassen. In diesem Falle wäre $R = \frac{1}{2}D$, so dass sich die Kugeln in der Darstellung der Abb. 1 gerade berühren. Durch Fokusonen kann eine erhebliche Energieübertragung über 100 Atomabstände eintreten. Im Kristallgitter wird jedoch die Energie durch Anregung thermischer Schwingungen dissipiert, ohne dass Gitterfehlstellen gebildet werden. Werden jedoch gewisse schon vorhandene Gitterfehlstellen (Versetzung, Korngrenze, Zwillungsgrenze usw.) von einem Fokuson getroffen, so kann das letzte Atom, das keinen direkten Stosspartner dieser Reihe mehr vorfindet, aus dem Gitterverband auf einen Zwischengitterplatz herausgestossen werden, sofern nur auf dieses Atom eine ausreichende Schwellenenergie (Threshold Displacement Energy) übertragen wird.

Crowdion-Stossprozesse sind dann zu erwarten, wenn der Stosspunkt P_C näher an der Gleichgewichtslage des angestossenen Atoms dieser Gitterreihe liegt.

In Abb. 1 sind auch die Verhältnisse für den Fall des Crowdions dargestellt. Im Gegensatz

zum Fokuson tritt in diesem Fall ein Platz-
wechsel der Atome ein. Vernachlässigt man die
Abhängigkeit des Radius R von der Energie E
des stossenden Atoms, so wird der Winkel bei
jedem Stoss grösser, bis das crowdionbildende
Zwischengitteratom aus der Kristallreihe hinaus-
gestossen wird oder mangels Energie in dieser
Atomreihe als Zwischengitteratom "hängen"
bleibt.

4. Korrelative Stossprozesse im α-Uran

Die Anwendung des Silsbee–Leibfried-Modells
auf das α-Urangitter kann zu einer Deutung des
Strahlungswachstums und der damit in Ver-
bindung stehenden Erscheinungen dienen.

Zunächst sei näher auf die bis 668° C
beständige orthorhombische Struktur des α-
Urans eingegangen. In der Einheitszelle treten
dabei folgende Atomabstände auf, wie aus Abb. 2
entnommen werden kann:

1.　2,762 Å zweimal　　(A–B)
2.　2,852 Å zweimal　　(C–D)
3.　3,261 Å viermal　　(B–C)
4.　3,322 Å viermal　　(A–C).

Man erkennt ferner aus der Abbildung, dass in
der c-Richtung, [001] keine dicht-gepackte
Reihe von Atomen existiert, wenngleich kleine
Atomabstände vorkommen. Dagegen liegen in
der a–b-Ebene dicht-gepackte Atomreihen mit
Atomabständen von 2,852 Å und 3,261 Å vor.
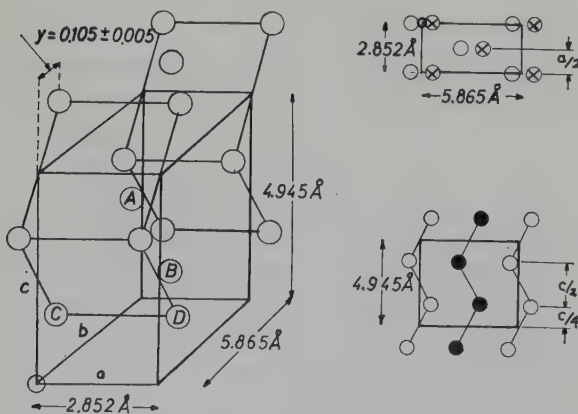Die Struktur dieser Gitterebene ist in Abb. 1

Abb. 2.　Die Struktur des α-Urans (nach Wilkinson
und Murphy [8]).

bei der Abhandlung der korrelativen Stoss-
prozesse oben schon verwandt worden. Die
Struktur des α-Urans kann als verzerrtes
hexagonales Gitter aufgefasst werden.

Bei der Spaltung (Fission) eines Uranatoms
werden etwa 10 Spaltungsprodukte (Spalt-
fragmente, Neutronen, β-Strahlung, γ-Strahlung
und Neutrinos) gebildet unter Freisetzung von
mehr als 10^8 Elektronen-Volt. Der grösste Teil
dieser Energie entfällt auf die Spaltfragmente,
die als Ursache für den Strahlungsschaden
angesehen werden müssen. Der Weg dieser
Fragmente ist durch Bereiche hoher Störung
ausgezeichnet, die allgemein Spikes genannt
werden (Thermal Spike, Displacement Spike).
Die Theorie der Spikes ist besonders von
Brinkman [9]) ausgearbeitet worden. Danach
können in einem Displacement-Spike des α-
Urangitters maximal etwa 60 000 eV umgesetzt
werden. Nach einem zugrunde gelegten Bild
werden aus einem Zentralbereich (verdünnte
Zone) Atome mit relativ hoher Energie in eine
verdichtete Zone hineingestossen. Die Zu-
sammenstösse mit den Atomen der Matrix sind
dabei zunächst voneinander unabhängig (R ist
klein). Stösse energieärmerer Atome ($\approx 10^2$ eV)
in Richtung dicht-gepackter Atomreihen werden
über korrelative Stossprozesse als dynamische
Crowdions oder Fokusonen über viele Atom-
abstände Energie ins Gitter hinein über-
tragen.

Die verschiedenen Gitter-Richtungen im α-
Uran sollen nun einzeln diskutiert werden.
Besonders interessieren die [100]-Richtung, in
der eine Schrumpfung unter Bestrahlung statt-
findet und die [010]-Richtung, in der Strah-
lungswachstum eintritt.

[100]-*Richtung:* In dieser Richtung liegt
eine Atomreihe mit Abständen von nur 2,852 Å
vor. Durch die äusserst dichte Besetzung dieser
Reihe ist diese Richtung für Fokusonen bevor-
zugt. Im idealen Gitter können diese keine
Fehlstellen hinterlassen. Treffen sie jedoch auf
eine Korngrenze, so kann die Energie aus-
reichen, um das letzte Atom der Reihe in das
benachbarte Korn hineinzustossen, wo es zu-
nächst einen Zwischengitterplatz einnimmt.

Einige dieser Zwischengitteratome werden bei erhöhter Temperatur durch Zwischengitter-diffusion der Korngrenze entfliehen und sich an einer anderen Korngrenze oder Versetzung ablagern. Die betrachtete Atomreihe hat also bei diesem Prozess ein Atom verloren.

[010]-*Richtung:* Diese Richtung ist durch das Strahlungswachstum ausgezeichnet. Aus Abb. 2 erkennt man, dass zwei dicht-gepackte Atomreihen [110] existieren, die mit der [010]-Richtung einen Winkel von etwa 26° ein-schliessen. Bei Atomabständen in diesen Reihen von 3,261 Å ist die Besetzung also aufgelockerter. Daher sind in diesen Richtungen Crowdions bevorzugt. Die Druckwelle der Verdichtungs-zone um einen Spike lässt Atome über dyna-mische Crowdions weit in das Gitter hinein-stossen. Die benachbarten Reihen wirken der Defokussierung der Crowdion-Stossprozesse ent-gegen. Der damit verbundene Atomtransport endet im idealen Gitter mit einem Zwischen-gitteratom. Trifft ein energiereiches Crowdion auf eine Korngrenze, so ist es in der Lage, das letzte Atom als Zwischengitteratom in das Nachbarkorn zu stossen. Die meisten Crowdions bleiben jedoch bevorzugt an der Korngrenze hängen und lagern das crowdion-bildende Zwischengitteratom an der Korngrenze ab, was zu einem Wachstum in dieser Richtung führt.

Für die beiden Atomreihen der a–b-Ebene des Urans kann die Schwellenenergie für Fokusonen, E_F, wie folgt abgeschätzt werden: Das Wechsel-wirkungspotential von Uranatomen soll durch die folgende Form [10]) gegeben sein

$$V(R) = A\mathrm{e}^{-R/a} \qquad (1)$$

mit den Konstanten $A = 8 \times 10^4$ eV und $a = 2,1 \times 10^{-9}$ cm. Wird der Radius entsprechend der Berührungsbedingung $(R = \frac{1}{2}D)$ eingesetzt, so erhält man mit der Beziehung $V(R) = \frac{1}{2}E$ [6])

$$E_F[100] = 180 \text{ eV}$$
$$E_F[110] = 67 \text{ eV}.$$

Danach können herausgestossene Atome mit einer Energie von weniger als 180 eV bei günstigem Auftreffen in [100]-Richtungen Fokusonen entwickeln. Entsprechendes gilt für die Atome mit 67 eV in [110]-Richtungen. Die Verschiedenheit der Schwellenenergien E_F für die Atomreihen ist das Merkmal dieses Wachs-tumsmodells. Energiereiche Atome im Bereich von 180–67 eV werden in [100]-Richtungen vorwiegend Fokusonen bilden, jedoch *nur* Crowdions in [110]-Richtungen.

[001]-*Richtung:* Im α-Uran sind keine dicht-gepackten Atomreihen in dieser Richtung vorhanden. Die energiereichen Stossteilchen (Knock-ons) der Verdichtungszone der Spikes können ihre Energie nicht mittels weitreichender korrelativer Stossprozesse abgeben. Daher werden sie nur in engumschriebenen Bereichen Atome aus ihren Gitterplätzen herausstossen. Dies führt schliesslich zu einer höheren Dichte von Zwischengitteratomen in der [001]-Rich-tung. Diese Verdichtungszone kann später unter Umständen in die entstandene ''Pore'' (cluster) zurückdiffundieren.

5. Das Modell der korrelativen Stossprozesse zur Erklärung verschiedener Erscheinungs-arten der Forminstabilität des α-Urans

Die Forminstabilität des α-Urans zeigt sich phänomenologisch auf verschiedene Weise. Ihre wichtigsten makroskopischen Erscheinungen lassen sich auf der Grundlage korrelativer Stossprozesse deuten.

5.1. RICHTUNGSABHÄNGIGKEIT DES STRAHLUNGSWACHSTUMS

Nach dem im letzten Abschnitt dargestellten qualitativen Modell treten in den verschiedenen Richtungen folgende Prozesse bevorzugt auf:

a) [100] Fokusonen – Energietransport – An der Korngrenze werden Atome in das Nachbarkorn gestossen.

b) [010] Crowdions – Transport von Zwischen-gitteratomen – Atome werden an der Korn-grenze abgelagert.

c) [001] Höhere Dichte an Zwischengitter-atomen und dadurch Abriegelung für weit-reichende Stossprozesse.

5.2. Abschätzung des Strahlungswachstums

Nach den Überlegungen von Leibfried ist die Zahl der gebildeten Crowdions mit einer Reichweite von n Atomabständen im kubisch-flächenzentrierten Gitter gegeben durch

$$C = 32F \frac{E_d}{E_F} \cdot \frac{1}{n^2}. \qquad (2)$$

F ist die Zahl der aus dem Gitterverband herausgestossenen Atome, die für einen Spaltprozess von Brooks [11]) mit 325 000 angegeben wird. Nimmt man an, dass für das Urangitter mit 12 nahen Nachbarn (Verwandschaft zum hexagonalen System!) die Zahl der Crowdions in ähnlicher Weise abgeschätzt werden kann und dass davon etwa 1/3 in die makroskopische Wachstumsrichtung stossen, so ergibt sich mit einer mittleren Reichweite von 30 Atomanständen für einen Spaltprozess

$$C_{[010]} \approx 1000.$$

Ein Strahlungswachstumskoeffizient, G_i, von einigen Hundert, wie in der Praxis beobachtet, wäre auf diese Weise verständlich.

5.3. Strahlungswachstum als Funktion der Korngrösse

Nach Beobachtungen verschiedener Forscher [2,12,13]) ist das Strahlungswachstum in polykristallinen Kristallen mit ausgeprägter Textur wesentlich stärker ausgebildet als in grobkristallinen Materialien oder Einkristallen. Diese Experimente lassen deutlich erkennen, dass die Korngrenzen eine bedeutende Rolle beim Wachstum spielen. Nach dem Modell der korrelativen Stossprozesse ist dieser Effekt auch zu erwarten. Die Ablagerung des crowdion-bildenden Zwischengitteratoms an Korngrenzen, Subkorngrenzen oder Zwillingsgrenzen wäre als primäre Stufe des Wachstums anzusehen. Danach würden alle gebildeten Crowdions aus der Randschicht mit der Breite von n Atomen eines Korns zum Wachstum beitragen. Das Strahlungswachstum sollte damit etwa umgekehrt proportional zum Kornradius sein. Genügend genaue experimentelle Ergebnisse liegen leider noch nicht vor, um diese Vermutung zu bestätigen.
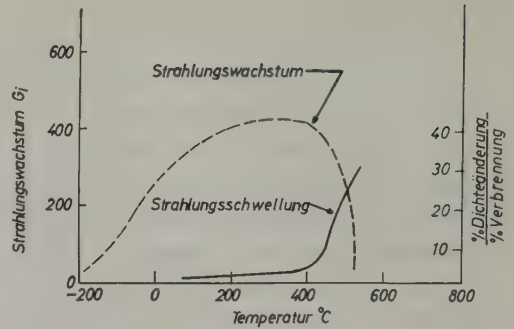

Abb. 3. Temperaturabhängigkeit von Strahlungswachstum und Strahlungsschwellung (nach Seigle und Castleman [17])).

5.4. Temperaturabhängigkeit des Strahlungswachstums

In Abb. 3 ist die Temperaturabhängigkeit des Strahlungswachstums dargestellt. Bei etwa 300° C wird ein Maximum beobachtet, während bei tiefen Temperaturen ($< 0°$ C) und hohen Temperaturen ($> 500°$ C) kaum noch Strahlungswachstum stattfindet.

Diese Erscheinungen können wie folgt gedeutet werden: Nach den beschriebenen Vorstellungen verlieren die Körner in der [100]-Richtung Atome, während neue in der [010]-Richtung angebaut werden. An den Korngrenzen entsteht ein Spannungsfeld. Der ansteigende Ast entspricht dann der thermisch aktivierten Relaxation der Korngrenzenbewegung.

Auffallend ist der Kurvenbereich oberhalb von 400° C, wo das anisotrope Strahlungswachstum von einer anderen Erscheinung — Strahlungsschwellung — abgelöst wird. Bei ansteigenden Temperaturen tritt durch die thermische Bewegung der Atome eine Defokussierung der korrelativen Stossprozesse in den dicht-gepackten Atomreihen ein. Die Reichweite der Fokusonen und Crowdions (n) nimmt ab. Dadurch werden Strahlungseffekte mehr auf die nähere Umgebung der Spikes verlagert. Die anisotrope Forminstabilität nimmt einen isotropen Charakter an.

5.5. Strahlungsschwellung (swelling)

Bei höheren Temperaturen kann die Energie

nicht mehr über weitreichende Stossprozesse in bevorzugten Richtungen in das Gitter hineingetragen werden. Dadurch wird die Energiedichte in den Störbereichen grösser. Die Störbereiche nehmen kugelförmige Gestalt an. Gefördert wird dieser Vorgang dadurch, dass das Gitter bei höheren Temperaturen der dichtgepackten hexagonalen Struktur ähnlicher wird (siehe Ausdehnungskoeffizienten verschiedener Gitterrichtungen in Tab. 1). Nach diesen Vorstellungen sollte das anisotrope Strahlungswachstum bei Temperaturen, wo die weitreichenden korrelativen Stossprozesse ausbleiben, durch einen isotropen Wachstumsmechanismus abgelöst werden, der als nicht mehr strukturabhängige Strahlungsschwellung beobachtet wird. Die elektronenmikroskopisch beobachteten Poren könnten ihren Ursprung in solchen Störbereichen haben. Das Anwachsen dieser Poren ist nach Greenwood, Foreman und Rimmer [14] durch einen thermisch aktivierten Diffusions-Mechanismus zu deuten. Besonders der Abbruch des Strahlungswachstums bei höheren Temperaturen und der gleichzeitige Übergang zur Strahlungsschwellung kann als Stütze dieses Modells angesehen werden.

5.6. Strahlungswachstum von Uran-legierungen

Das Strahlungswachstum ist vom technischen Standpunkt aus eine sehr unerwünschte Eigenschaft der Brennelemente. Man kann versuchen, das Wachstum durch Legierungsbildung zu vermindern. Gemäss dem Modell der korrelativen Stossprozesse können zwei "Rezepte" angegeben werden, um das Strahlungswachstum zu reduzieren:

a) Zusätze, die zu einer Herabsetzung der Anisotropie führen, bewirken, dass die auftretenden korrelativen Stossprozesse mehr isotropen Charakter annehmen und die Auszeichnung einer Wachstumsrichtung weniger in Erscheinung tritt. So bemerkten Konobeevsky und Mitarbeiter [15], dass durch Zugabe von Molybdän und Plutonium die Unterschiede zwischenatomarer Abstände kleiner werden, das Gitter also dem idealen hexagonalen System

zustrebt. Kittel und Paine [16] beobachten, dass das Strahlungswachstum von Uran mit diesen Legierungskomponenten tatsächlich merklich reduziert wird.

b) Durch Zusätze leichter Atome tritt bei den korrelativen Stossprozessen in einer dichtgepackten Reihe ein erheblicher Energieverlust ein, wie sich unmittelbar aus der Stossformel für die maximal übertragbare Energie ergibt

$$E = E_0 \frac{4 M_1 M_2}{(M_1 + M_2)^2} \qquad (3)$$

M_1 und M_2 sind die Massen der beiden Stosspartner. Die Reichweite der korrelativen Stossprozesse wird kleiner und die Anisotropie damit herabgedrückt.

6. Vergleich der korrelativen Stossprozesse mit anderen vorgeschlagenen Mechanismen zur Deutung der Forminstabilität

Eine Reihe von Mechanismen zur Deutung der Forminstabilität des α-Urans sind vorgeschlagen worden [17,18]. Sie können auf zwei Grundvorstellungen reduziert werden: Spikes und Diffusion.

6.1. Spikes

Diese Hypothese geht von der Vorstellung aus, dass die umgebende Matrix eines Spikes (Thermal Spike, Fission Spike) während der kurzen Aufheizung und Abkühlung plastische irreversible Verformung erfährt. Für die Anisotropie können nun entweder die Verschiedenheit der Ausdehnungskoeffizienten oder die Unterschiede in den plastischen Eigenschaften in den 3 Richtungen herangezogen werden. Die Spannungsrelaxation der Spike-Mechanismen kann durch Gleitung (Slip) oder durch Zwillingsbildung (Twinning) erfolgen. Gegen einen Spike-Mechanismus sprechen folgende Argumente:

a) Die räumliche Ausdehnung und die Lebensdauer eines Spikes sind zu kurz, um plastische Verformung hervorzurufen.

b) Die Korngrössenabhängigkeit ist schwerlich mit einem Spike-Mechanismus zu erklären.

6.2. Diffusion

Seigle und Opinsky [19] schlugen zur Erklärung des Strahlungswachstums vor, dass die unter Strahlung gebildeten Zwischengitteratome und Leerstellen (Frenkelpaare) anisotrop diffundieren. Nach dieser Theorie sollten Zwischengitteratome besonders in [010]-Richtung und Leerstellen in [100]-Richtung wandern, während die Diffusionsgeschwindigkeit in [001]-Richtung ungefähr für beide Fehlstellen gleich sein sollte. An den Korngrenzen bleibt die betreffende Fehlstelle hängen, was zu einer entsprechenden Ausdehnung oder Verkürzung des Kristalls führt.

Die Anisotropie der Wanderung von Zwischengitteratomen und Leerstellen haben die Diffusionstheorie und das hier vorgeschlagene Modell zur Erklärung des Strahlungswachstums des α-Urans in gewissem Sinne gemeinsam, jedoch liegt bei der Diffusion ein statistischer und thermisch aktivierter Prozess vor, während die Energie für die korrelativen Stossprozesse aus der Wechselwirkung von Strahlung und Materie und deren Folgeerscheinungen entnommen wird.

Experimentell sollte eine Verifizierung der korrelativen Stossprozesse dadurch möglich sein, dass die Emission von Uran-Atomen einer unter Spaltung stehenden Einkristallprobe in den verschiedenen Richtungen untersucht wird. In Richtungen mit ausgeprägter Längenänderung zeigen sich unter Umständen "Muster", die denen von Thompson [5] entsprechen. Bei höheren Temperaturen sollte beim Übergang von Strahlungswachstum $\rightarrow$ Strahlungsschwellung ($\approx 400°$ C) die anisotrope Emission zur einer isotropen werden.

Literatur

[1] A. M. Turkalo, Knolls Atomic Power Laboratory Report, KAPL-1044 (1954)

[2] S. H. Paine und J. H. Kittel, Erste Genfer Konferenz, 8/P/745 (1955)

[3] J. A. Brinkman, J. appl. Phys. 25 (1954) 961

[4] R. H. Silsbee, J. appl. Phys. 28 (1957) 1246

[5] M. W. Thompson, Phil. Mag. 4 (1959) 139

[6] G. Leibfried, J. appl. Phys. 30 (1959) 1388

[7] G. H. Vineyard, J. appl. Phys. 30 (1959) 1322

[8] W. D. Wilkinson und W. F. Murphy, Nuclear Reactor Metallurgy (Van Nostrand Co., New York, 1958) S. 41

[9] J. A. Brinkman, Am. J. Phys. 24 (1956) 246

[10] F. Seitz, und J. S. Koehler, Solid State physics 2 (New Academic Press Inc., New York, 1956) 305

[11] H. Brooks, Annual Review of Nuclear Science 6 (1956) 215

[12] R. Resnick und L. L. Seigle, 2. Nuclear Engineering and Science Conference, Philadelphia (1957) 57-NESC-63

[13] A. S. Zaimovsky, G. Y. Sergeev, V. V. Titova, B. M. Levitsky und Y. N. Sokursky, Zweite Genfer Konferenz, 5/P/2191 (1958)

[14] G. W. Greenwood, A. J. E. Foreman und D. E. Rimmer, AERE (Harwell), Report R-2863

[15] S. T. Konobeevsky et al., Zweite Genfer Konferenz, 15/P/2230 (1958)

[16] J. H. Kittel und S. H. Paine, Zweite Genfer Konferenz 5/P/1890 (1958)

[17] L. L. Seigle und L. S. Castleman, Zweite Genfer Konferenz 15/P/618 (1958)

[18] S. F. Pugh, Progress in Nuclear Energy (Pergamon Press, London, 1956), S. 652

[19] L. L. Seigle und A. J. Opinsky, Nucl. Sci. and Eng. 2 (1957) 38

AGEING AND HOT HARDNESS CHARACTERISTICS OF CERTAIN THORIUM ALLOYS

G. H. BANNISTER, R. C. BURNETT † and Miss J. R. MURRAY ††

UKAEA, *Metallurgy Division, Atomic Energy Research Establishment, Harwell, Didcot, Berks., UK*

Ageing experiments at 500°, 600° and 700° C on thorium-rich thorium-aluminium and thorium-uranium alloys are described, together with the results of similar tests at 600° C on five more complex thorium alloys; hot hardness tests at temperatures up to 800° C have been made on three samples of thorium and on several Th-Al, Th-U and Th-Zr alloys in the as-cast, solution treated and aged conditions.

Aluminium additions improved the hot hardness of thorium and the alloys showed considerable hardening due to precipitation of Th₂Al. The rate of ageing increased directly with aluminium content and with temperature while the maximum hardness for a given composition increased inversely with temperature. Little precipitation hardening was observed in thorium-uranium alloys containing up to 3 at % uranium and their hot hardness behaviour showed little significant improvement over unalloyed thorium. The results on thorium-zirconium alloys suggest that zirconium additions within the α-thorium solid solution range lead to solution hardening. In an alloy containing 22 at % zirconium, higher hot hardness values, up to 600° C, were obtained after solution annealing in the β (body-centred cubic) phase-field than after solution treatment in the (α + β) field.

Additions of aluminium and uranium in excess of the solubility limit restrict the grain growth of thorium at 1150° and 1200° C respectively.

Des expériences de vieillissement à 500°, 600° et 700° C sur des alliages Th-Al riches en thorium et des alliages Th-U sont décrites, en même temps que sont donnés les résultats d'essais analogues à 600° C sur 5 alliages de thorium plus complexes. Des essais de dureté à chaud à des températures jusqu'à 700° C ont été effectués sur trois échantillons de thorium et sur plusieurs alliages Th-Al, Th-U, et Th-Zr dans l'état coulé, homogénéisé en solution solide et vieilli.

Des additions d'aluminium améliorèrent la dureté à chaud du thorium et les alliages montraient un durcissement considérable dû à la précipitation de Th₂Al. La vitesse de vieillissement croissait proportionnellement à la teneur en aluminium et avec la température tandis que la dureté maximum pour une composition donnée croissait de façon inversement proportionelle à la température. Un faible durcissement par précipitation observé dans des alliages Th-U contenant jusqu'à 3 at % U et leur comportement à la dureté à chaud ne montrait pas une nette amélioration vis à vis du thorium non allié. Les résultats sur les alliages Th-Zr suggèrent que les additions de zirconium dans le domaine de la solution solide du thorium-α conduisent à un durcissement structural. Dans un alliage contenant 22 at % Zr, des valeurs de dureté à chaud plus élevées (jusqu'à 600° C) furent obtenus après recuit de mise en solution dans le domaine β (cubique centré) qu'après traitement de mise en solution dans le domaine (α + β).

Des additions d'aluminium et d'uranium au-delà de la limite de solubilité réduisent le grossissement de grain du thorium à 1150° et 1200° C respectivement.

Es wurden Aushärtungsversuche an thoriumreichen Thorium-Aluminium- und Thorium-Uran-Legierungen bei 500, 600 und 700° sowie an 5 komplizierter aufgebauten Legierungen bei 600° vorgenommen. Warmhärte-Prüfungen wurden bei Temperaturen bis 800° an drei Thorium-Proben und an verschiedenen Thorium-Aluminium, Thorium-Uran und Thorium-Zirkon-Legierungen durchgeführt. Die Proben befanden sich dabei in gegossenem, geglühtem oder ausgehärtetem Zustand.

Aluminium-Zusätze verbesserten die Warmhärte von Thorium. Diese Legierungen zeigten eine beträchtliche Härtezunahme infolge Ausscheidung von Th₂Al. Die Aushärtungsgeschwindigkeit stieg direkt mit dem Aluminiumgehalt und mit der Temperatur an, während die maximal erzielbaren Härtewerte mit steigender Temperatur abnahmen. Bei Thorium-Uran-Legierungen mit Gehalten bis zu 3 At % Uran

---

† Now at Atomic Energy Establishment, Winfrith, Dorset, UK.
†† Now at Department of Metallurgy, Imperial College of Science and Technology, London, S.W. 7.

wurde nur eine geringfügige Härtesteigerung durch Ausscheidung beobachtet. Auch die Warmhärte dieser Legierungen lag nur unwesentlich über der von unlegiertem Thorium. Die an Thorium-Zirkon-Legierungen gewonnenen Ergebnisse lassen vermuten, dass Zirkonzusätze innerhalb des Bereichs von α-Thorium zu einer Härtesteigerung infolge Mischkristallbildung führen. Bei einer Legierung mit 22 At % Zirkon

wurden nach einer Glühung im β-Bereich (kubisch raumzentriert) höhere Warmhärtewerte (bis zu 600°) gefunden, als nach einer Glühbehandlung im α + β-Bereich.

Überschritten die Aluminium- und Uran-Gehalte die entsprechenden Löslichkeitsgrenzen, so wurde das Kornwachstum von Thorium bei 1150 und 1200° abgeschwächt.

1. Introduction

The solubilities of aluminium and of uranium in thorium have previously been shown to be temperature dependent [1, 2]), and ageing experiments on these binary alloys are now described together with the results of similar tests on four ternary and one quaternary thorium-base alloy. The hot hardness testing of metals and alloys is a useful, but not unambiguous, method of assessing their strengths at elevated temperatures and their deformation characteristics during hot working; in addition, the results of such tests on an alloy may indicate a range of temperature in which good creep resistance might be expected. An evaluation of some of these properties has been made by hot hardness tests on three samples of thorium and several thorium-base alloys at temperatures up to 800° C.

2. Materials and Specimen Preparation

Two grades of thorium were employed: (a) production bar material having a total thorium content of 99.5–99.6 wt % and containing 400–700 ppm carbon, 3000–4000 ppm oxygen and total metallic impurities of less than 300 ppm; (b) electrolytic thorium with a carbon content of 100–150 ppm and oxygen of 2000–3000 ppm, metallic impurities being again less than 300 ppm. High purity aluminium, magnesium-reduced uranium billet (with a carbon content of approximately 300 ppm), iodide titanium and iodide zirconium were used as the alloying materials.

All the alloys were prepared by arc-melting in a zirconium-gettered argon atmosphere; specimens for ageing tests were cast into a 9 mm dia. mould while those for hot hardness testing were cast into cylinders 12 mm dia × 12 mm
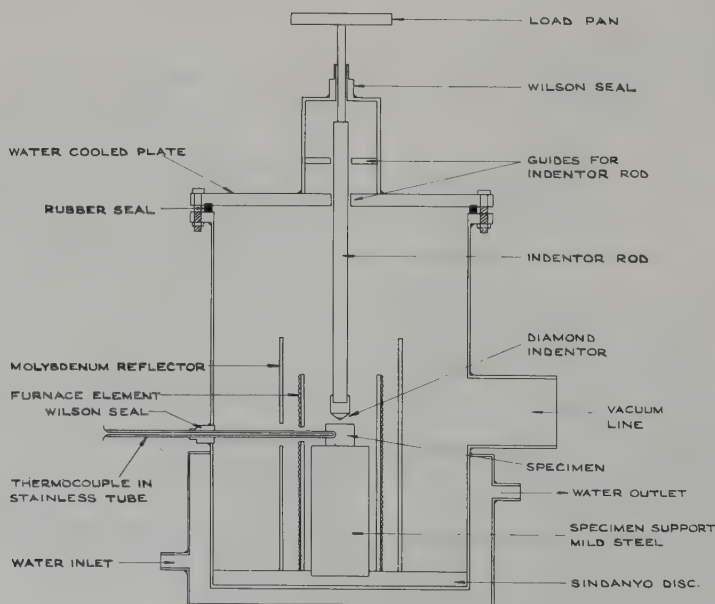

Fig. 1.   Vacuum hot hardness rig.

long or "buttons" 25 mm in diameter. For solution treatment they were wrapped in tantalum foil, sealed in evacuated silica capsules, annealed at 900°–1200° C (depending on the material) and quenched by breaking the capsule under water.

3. Ageing Tests

For ageing treatments of up to 67 h the alloys were placed in a vertical, continuously evacuated silica tube and were heated by an external furnace which was interchangeable with a bucket of cold water for cooling. For longer annealing times, specimens were sealed in evacuated silica capsules, placed in a furnace and cooled by removal and immersion in a bucket of cold water without breaking the silica.

The hardness of the aged materials was determined using a standard Vickers pyramid hardness tester with a 10 kg load; all results are the average of at least three values.

4. Hot Hardness Test

The hot hardness apparatus, shown in fig. 1, consisted essentially of a water cooled copper chamber evacuated by a rotary backing pump and an oil diffusion pump. The sample to be tested was sited on a platform in the bottom of the chamber and surrounded by a wire wound resistance furnace and tantalum reflector. Movement of the specimen was made by a stainless steel tube positioned in a small hole in the edge of the specimen and worked through a Wilson seal in the side of the chamber. A thermocouple was placed in the tube for direct reading of the specimen temperature and hardness impressions were made with a 136° pyramidal diamond loaded by a rod and scale pan outside the tank, the rod operated through a Wilson seal in a top plate of the chamber which was water cooled. The impressions were measured with an eyepiece micrometer after removing the specimen from the apparatus.

A load of 5 kg was used from room temperature to 800° C. Two indentations were made at room temperature and from 100° C–800° C at intervals of 100° C. The spacing between

each indentation was 2–3 times the diagonal of the impression and the load was applied for 30 seconds; results on any one specimen at any temperature were reproducible to $\pm$ 5 VPN. The heating time to the test temperature was approximately ten minutes and the sample was held at temperature for an equal time before the indentation was made.

5. Metallographic Examination

Standard methods of metallographic preparation were employed and grain sizes were revealed by ionic bombardment in an argon atmosphere [3]). All specimens were examined when testing was completed, and in addition the binary thorium-aluminium and thorium-uranium alloys prepared from production thorium were examined at intervals during the ageing tests.

6. Ageing Results

Hardness values are plotted against log time in figs. 2–7 and the details are described below. After solution treatment, alloys prepared from production bar thorium were about 5 VPN harder than corresponding specimens made from electrolytic material.

6.1. THORIUM-ALUMINIUM: (figs. 2–4)

All the thorium-aluminium alloys showed marked precipitation hardening behaviour. The hardness in the solution-treated condition increased with aluminium content and there was little difference between the ageing results obtained on 1 at % aluminium alloys prepared from the two types of thorium. The rate of ageing increased directly with aluminium content and with temperature in the range 500–700° C, while the maximum hardness for a given composition increased inversely with temperature. At 300° C age-hardening had not begun after 1000 h. Over-ageing occurred rapidly at 700° C for each composition but at 500° C no significant drop in hardness of the 1 or 2 at % aluminium alloys had occurred 1000 h. The maximum hardness obtained was
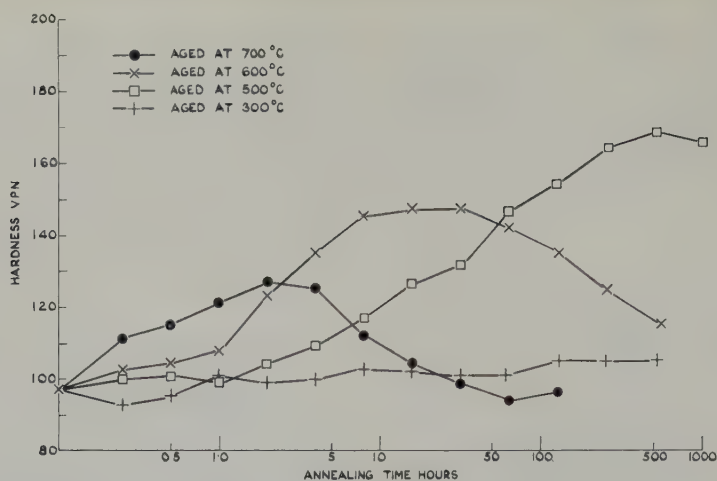
Fig. 2.   Ageing curves for thorium/1 at % aluminium, prepared from electrolytic thorium.
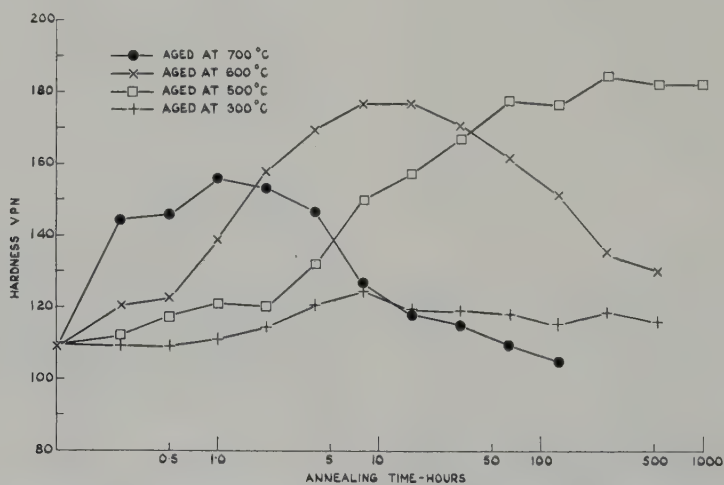

Fig. 3.   Ageing curves for thorium/2 at % aluminium, prepared from production thorium.
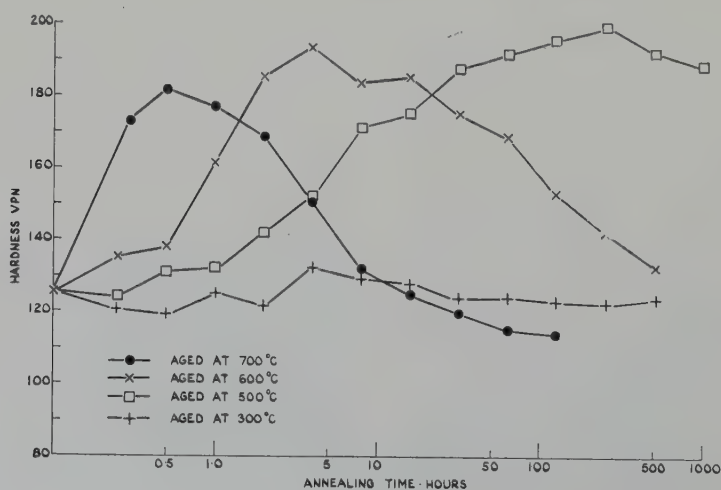

Fig. 4.   Ageing curves for thorium/5 at % aluminium, prepared from production thorium.
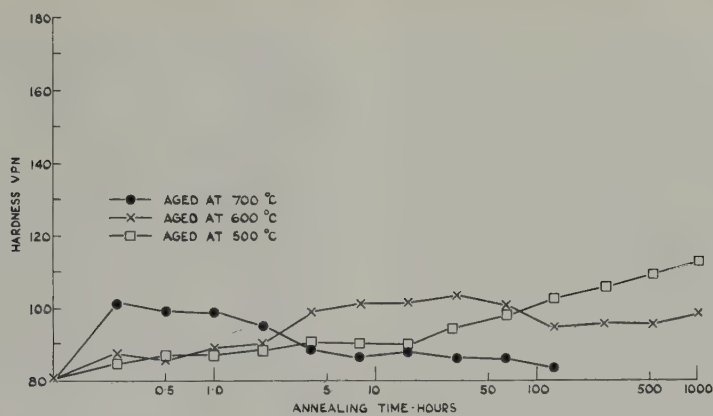
Fig. 5.   Ageing curves for thorium/2 at % uranium, prepared from electrolytic thorium.
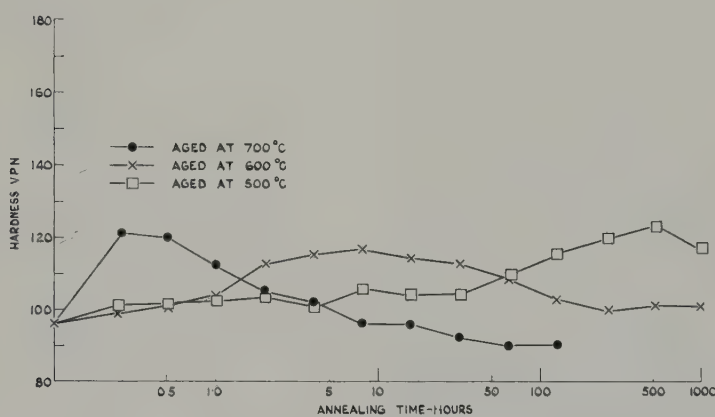

Fig. 6.   Ageing curves for thorium/3 at % uranium, prepared from production thorium.
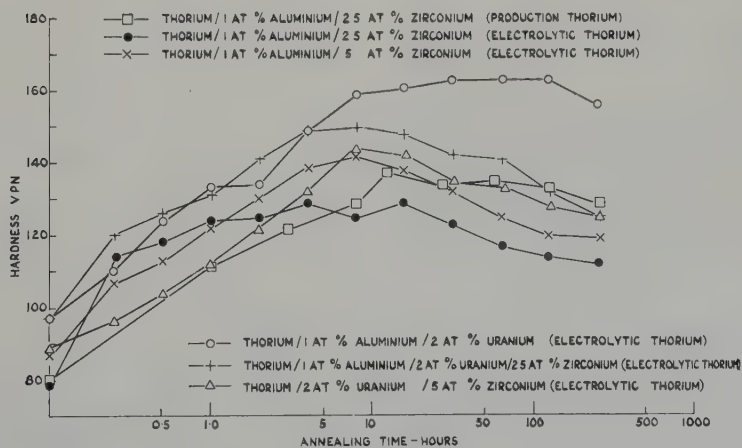

Fig. 7.   600° C Ageing curves for complex thorium-base alloys.

199 VPN with 5 at % aluminium after 264 h at 500° C.

Grain sizes of approximately 3 mm and 0.3 mm were observed with 1.0 and 2.0 at % aluminium respectively. Since unalloyed thorium also has a grain size of approximately 3 mm after similar thermal treatment and the solubility of aluminium in thorium at 1300° C is 0.85 at %, it appears that 1.0 at % aluminium is sufficiently close to the solubility limit to have little effect on grain growth.

6.2. Thorium-uranium: (figs. 5 and 6)

These alloys showed only a slight increase of hardness on ageing, the hardness in the solution treated condition increasing with the amount of alloying element. There was no significant difference between the results obtained on 2 at % uranium alloys prepared from the two types of thorium. The rate of ageing varied with temperature but did not alter with composition; overageing had begun after $\frac{1}{4}$ h at 700° C but at 500° C annealing times approaching 1000 h were required before peak hardness was exceeded. The hardness increase did not alter with composition or ageing temperature and maximum hardness values were 112 and 123 VPN for 2 at % and 3 at % uranium respectively. Metallographic examination showed that uranium in excess of the solubility limit reduces grain growth at 1200° C.

6.3. Complex alloys: (fig. 7)

The hardness of all the complex alloys increased on ageing at 600° C. They each aged at the same rate for the first 8 hours and softening occurred slowly with further annealing of all except the thorium-aluminium-uranium alloy; this gave the highest peak hardness of 163 VPN and had a hardness of 156 VPN after 256 hours.

7. Hot Hardness Results

The variation of hardness of thorium and thorium alloys with temperature is shown in figs. 8–11 and the more important features are discussed below.

7.1. Thorium (fig. 8)

The initial higher hardness of the production thorium in the "as-received" condition is probably associated with the light reduction by swaging given to this material after sintering and the lower hardness of electrolytic thorium below 500° C, to its lower carbon content. All three materials show a tendency to a hardness plateau in the temperature range 200–400° C, the effect being most pronounced in the "as-received" production bar. Figs. 9 and 10 give an indication of the distribution of the oxide inclusions in the arc-melted samples of production and electrolytic thorium, and these are also typical of alloys prepared from these materials; the corresponding grain sizes of the two types of unalloyed thorium, after testing, were 30 μ and 80 μ respectively.

7.2. Alloys prepared from production thorium (fig. 11)

These results, obtained by R. C. Burnett and S. F. Pugh, have been included here since they have not been reported previously. There is little difference between the hot-hardness values for the thorium-zirconium, thorium-zirconium-uranium and thorium-zirconium-titanium alloys
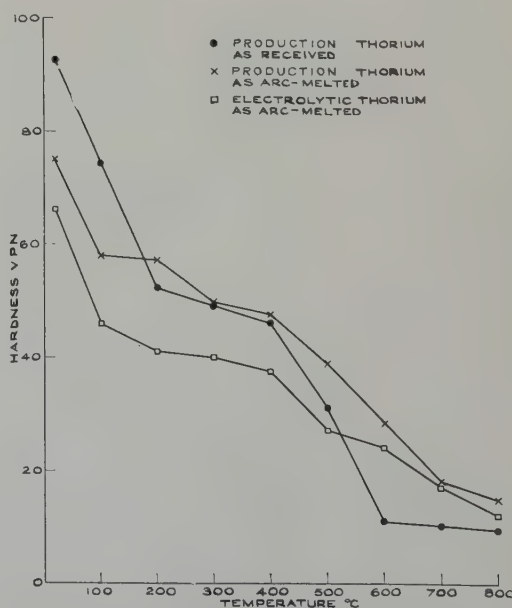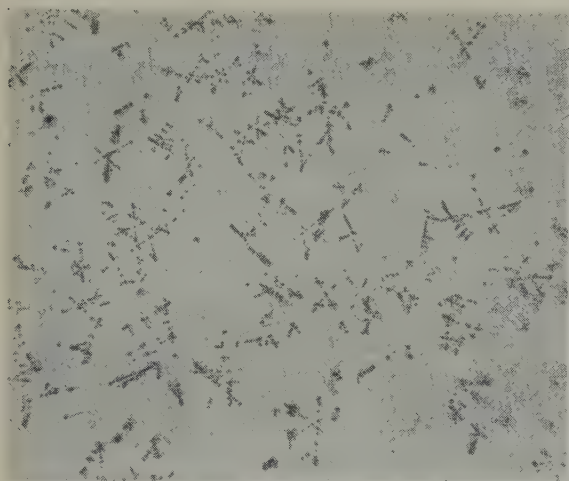

Fig. 8.   Hot hardness curves for thorium.

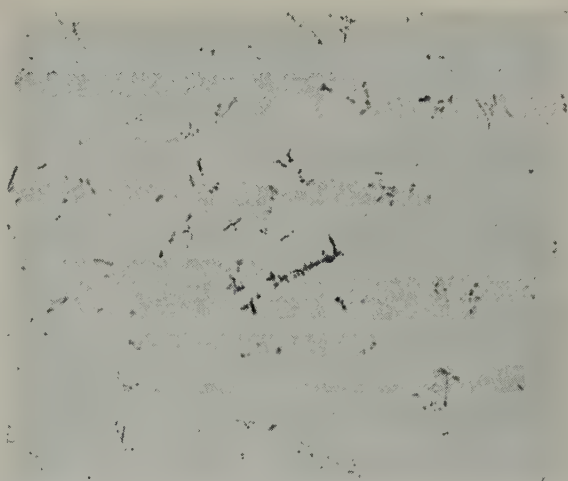Fig. 9. Arc-melted production thorium. Mechanical polish. ThO$_2$ dendrites dark. × 150.

Fig. 10. Arc-melted electrolytic thorium. Mechanical polish. ThO$_2$ dendrites dark. × 150.
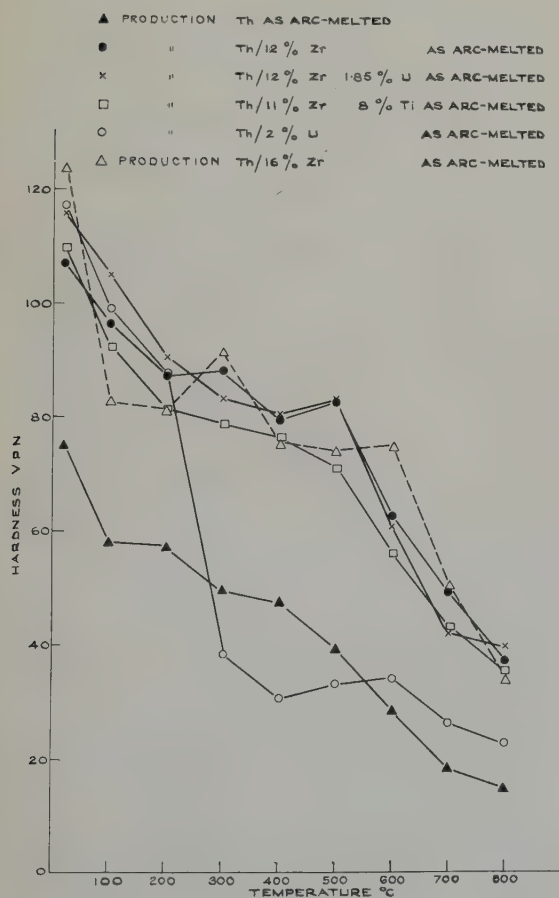

Fig. 11. Hot hardness curves for alloys made with production thorium.

tested in the arc-melted condition; all showed a tendency to a hardness plateau in the range 200°–500° C, (with 16 at % zirconium the plateau extends to 600° C) and all were significantly harder than unalloyed thorium over the whole range of temperature. The reason for the drop in hardness of the thorium-uranium alloy between 200° C and 300° C is not clear; much of the uranium was present as a discontinuous grain boundary network and in view of the long annealing times required to redistribute uranium in thorium below 800° C [2]) no such changes would be expected to occur during hardness testing.

7.3. ALLOYS PREPARED FROM ELECTROLYTIC THORIUM

These were all examined in the following conditions: (a) as-cast (b) as solution treated, and (c) as solution treated and aged for seven days at 600° C.

(i) *Thorium-zirconium*: (figs. 12–14). Each of the three alloys was harder than unalloyed thorium in all conditions and below 600° C was softer after solution-annealing than as-melted. The as-melted hardness/temperature relations for alloys of 12 at % zirconium prepared from electrolytic (fig. 13) and from production thorium (fig. 11) showed no signifi-
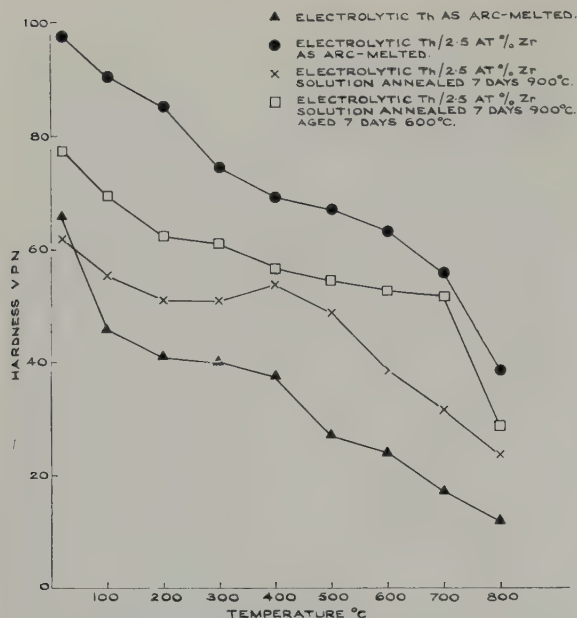
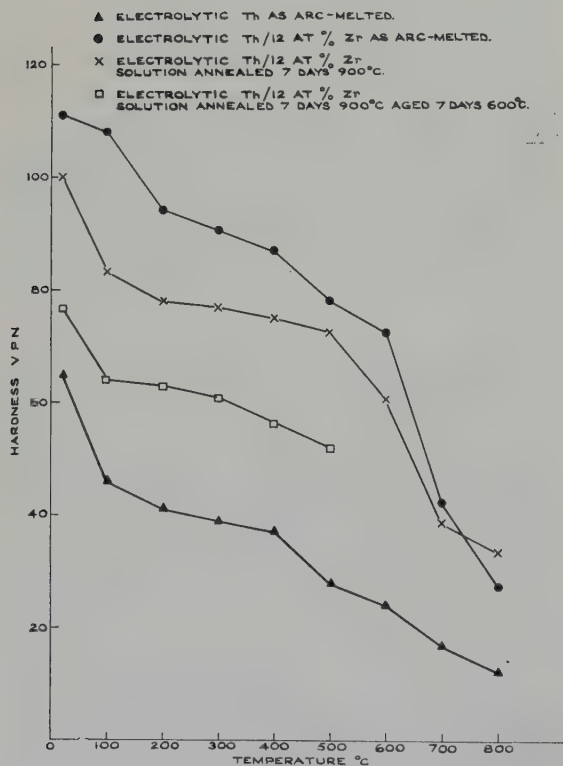Fig. 12.   Hot hardness curves for thorium/2.5 at %
zirconium.

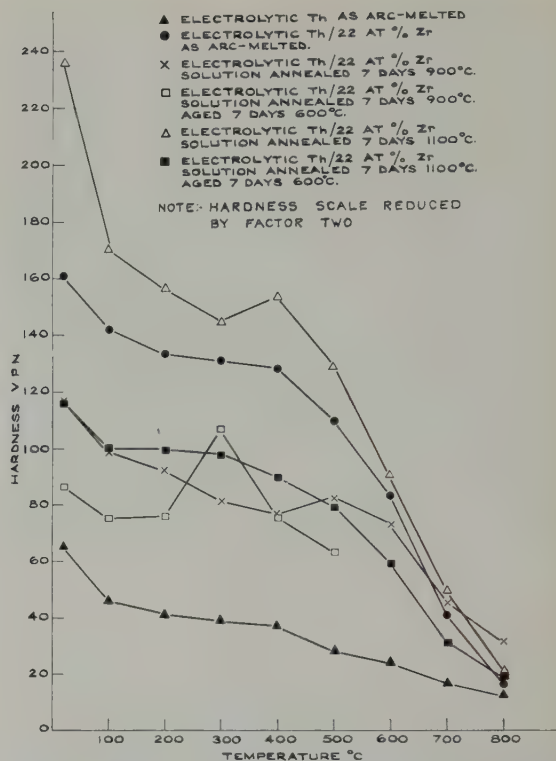Fig. 13.   Hot hardness curves for thorium/12 at %
zirconium.

Fig. 14.   Hot hardness curves for thorium/22 at %
zirconium.

cant differences in spite of the different carbon
contents of the materials. After solution treating
at 900° C, the 2.5 and 12 at % zirconium alloys
showed a tendency to a hardness plateau in the
temperature range 100°–500° C; with 22 at %
zirconium this range was increased to 100°–
600° C.

Solution treatment of the 22 at % zirconium
alloy in the body centred cubic (β) phase field
at 1100° C produced a marked increase in hard-
ness at temperatures up to 600° C but on
subsequent ageing at 600° C the hardness
dropped appreciably although it remained $2\frac{1}{2}$
times higher than that of unalloyed thorium. This
composition is the minimum zirconium addition
to enable β solution treatment at 1100° C; at
900° C all compositions fall in the ($\alpha + \beta$)field.

(ii)   *Thorium-aluminium* : (figs. 15–17). Below
700° C, in the as-cast condition, there was a
considerable increase in the hot hardness with
aluminium content. This might be related to the
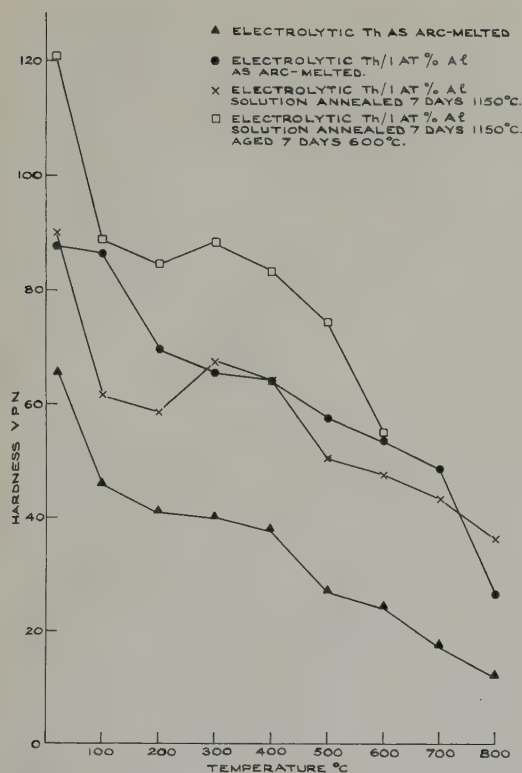amount of Th-Th$_2$Al eutectic present in the

Fig. 15.   Hot hardness curves for thorium/1 at %
aluminium.

grain boundaries since the solubility of alu-
minium in thorium is less than 1 at % at
1300° C [1]). After solution treating there was no
significant hardness differences between the
three compositions, possibly because the Th_2Al
in the eutectic had started to "ball-up" and
each alloy contained aluminium in excess of the
solubility limit. After ageing for seven days at
600° C the 1 and 5 at % alloys had higher hot
hardness values than in the solution treated
condition at all temperatures tested. Both alloys
showed evidence of a strain-ageing peak at
300°–400° C and by analogy with steel [4])
might have particularly good creep properties
at 250°–350° and be significantly better than
unalloyed thorium up to 500° C. Metallographic
examination showed that considerable grain
growth had occurred during solution treatment
of each alloy and grain sizes of the 1, 5 and 8
at % aluminium alloys after testing were
approximately 2 mm, 0.5 mm and 0.25 mm

respectively. With 1 at % aluminium there
were a few particles of Th_2Al which had not
been in solution at 1150° C and a fine precipitate
of Th_2Al was observed in the grain boundaries
and also within the grains. Less fine precipitate
was present in the 5 and 8 at % alloys possibly
because of the initial presence of many Th_2Al
particles which could act as nuclei for subse-
quent precipitation.

(iii) *Thorium-uranium :* (fig. 18). The alloy
containing 2 at % uranium was slightly harder
than that containing 3 at % uranium in the
as-cast condition. The reason for this is not
clear but might be due to a different amount of
superheat and hence cooling rate in the two
melts. The hot-hardness results for both
materials were similar after solution treating
and after ageing; in each case the aged curve
was lower. The curves for the 3 at % uranium
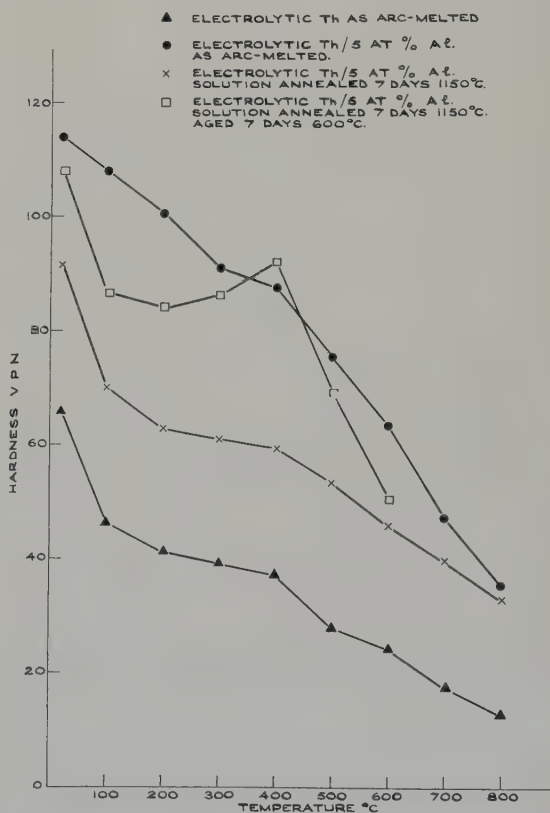alloy are given here as typical.

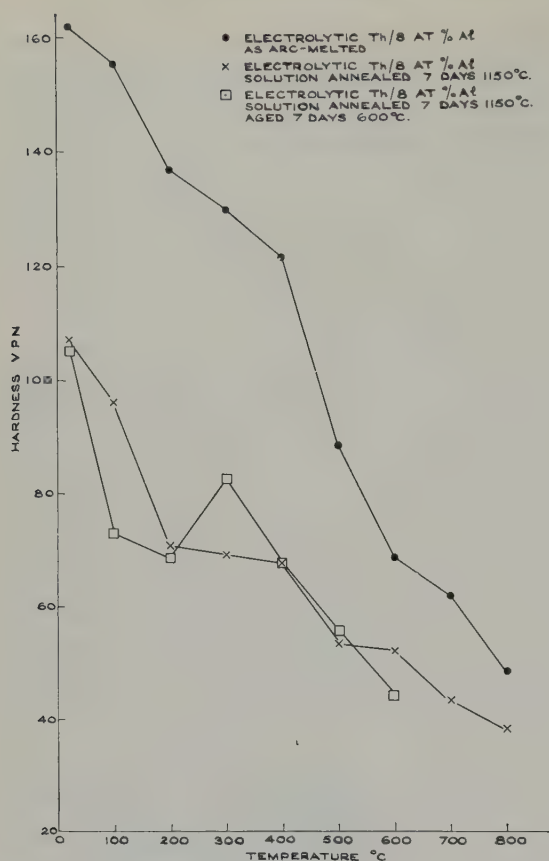Fig. 16.   Hot hardness curves for thorium/5 at %
aluminium.

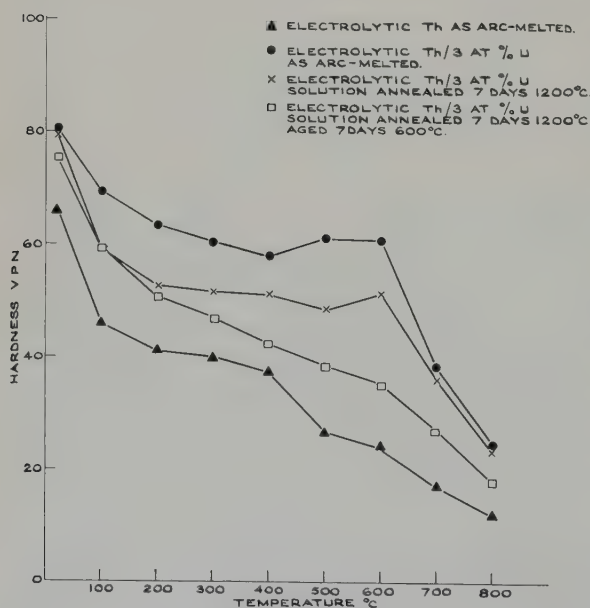Fig. 17.   Hot hardness curves for thorium/8 at %
aluminium.

Fig. 18.   Hot hardness curves for thorium/3 at %
uranium.

Grain sizes determined after the completion of testing were approximately 1 mm and 0.1 mm respectively for the 2 at % and 3 at % alloys; precipitation occurred in the grain boundaries and within the grains of both alloys. With 3 at % uranium, the excess uranium present during solution treatment was associated with the grain boundaries, and with both 2 and 3 at % uranium the boundaries showed some association with ThO_2 particles.

8. Discussion

Alloys of thorium and uranium exhibit a considerably smaller hardness increase on ageing than those of thorium and aluminium although the change in solubility with temperature is greater for the former. In thorium-uranium alloys the precipitate is β-uranium at 700° C and α-uranium below 660° C; neither modification can form coherently on the α-thorium matrix and a considerable degree of misfit must occur. The precipitating phase in thorium-aluminium alloys is Th_2Al. Since α-thorium, like aluminium, is face-centred-cubic at the ageing temperature and Th_2Al is isostructural with $CuAl_2$, there is a possibility that precipitation in thorium-aluminium alloys is multi-stage, as is the case with aluminium-rich alloys in the aluminium-copper system; if it were so, then one stage might be the formation of a coherent precipitate with consequent increase in hardness. It was not possible to determine categorically if there was an initial small hardness peak in the present series of alloys; a slight increase was observed at 300°, 500° and 600° C before the main hardening began but this was only slightly greater than the experimental error. In thorium-aluminium alloys, grain boundary precipitation was first detected metallographically after ageing for $2\frac{1}{2}$ h at 600° C, i.e. when the hardness had just started to increase.

Except for the thorium-aluminium-uranium alloys, all the ternaries showed evidence of slight grain-boundary liquation after solution treatment at 1200° C and therefore, assuming maximum solubility at the eutectic tempera-

ture, the amount of alloying elements in solid solution was less than this maximum. Since the constitution of none of the complex alloys has been studied over the relevant range of composition, the eutectic temperatures are not known nor is it possible to predict the nature of the precipitating phases.

No attempt has been made to determine the effect of the rate of cooling from 1200° C on the subsequent ageing behaviour of any of these alloys. In aluminium-rich aluminium-copper alloys Prakash and Entwistle [5] have shown that slower rates of cooling from the solution anneal lead to failure to retain vacancies and hence a lower hardening rate. The effect of grain size on the rate of ageing has not been investigated; the complex alloy which overaged least rapidly had the coarsest grain size, but it is not known whether the slower rate of overageing was due to the coarse grain size or to the nature of the material.

Since alloys which show appreciable ageing at the upper temperatures of hot hardness testing would give a hot hardness result which was a function of thermal history, the conditions of solution treatment, of ageing and of hot hardness testing were standardised in order that the hardness results might give a useful comparison between different materials. An ageing treatment of seven days at 600° C prior to hot hardness testing was deliberately chosen so as to overage the alloys, in an attempt to use the hot hardness tests to assess the possible long-term creep behaviour of these materials at lower temperatures.

The hardness results after solution treatment at 900° C suggest that zirconium additions within the α-thorium solid solution range lead to solution hardening, while the similar hardness of alloys after ageing at 600° C indicates that no capacity for age-hardening remains after this treatment. (The solid solubility of zirconium in thorium at 900° C and 600° C is 8.2 at % and < 5 at % respectively [6]).)

A few previous hot-hardness results are available on thorium and thorium alloys. Goldhoff, Ogden and Jaffee [7] examined a series of binary alloys, (all of which had been annealed 2 h at 850° C), at room temperature and at 300° C. Their values for unalloyed thorium at the two temperatures were intermediate between those obtained on production and electrolytic thorium in the present investigation; figures for a 1 at % aluminium alloy show rather greater temperature dependence than the present results on solution treatment material and no relation to the figures at 300° C on aged material, while their values for 1 at % zirconium are higher than the present results on 2.5 at % zirconium. Peterson, Russi and Nickelson [8] report the as-cast hardness of a 1 at % aluminium alloy as 84 VPN, which accords with 87 obtained here. The room temperature hardness of the thorium/3 at % uranium alloy showed little variation with heat treatment and was in agreement with Bentle's [9] figures for a commercial purity alloy of this composition after a variety of heat treatments.

Acknowledgements

References

[1]   J. R. Murray, J. Inst. Metals **87** (1958–9) 349

[2]   J. R. Murray, J. Inst. Metals **87** (1958–9) 94

[3]   D. Armstrong, P. E. Madsen and E. C. Sykes, J. Nucl. Mat. **1** (1959) 127

[4]   R. C. Burnett, AERE (Harwell) Report, M/M 98 (1955)

[5]   V. Prakash and K. M. Entwistle, J. Inst. Metals **87** (1958–9) 262

[6]   R. H. Johnson, Sheffield University, private communication

[7]   R. M. Goldhoff, H. R. Ogden and R. I. Jaffee, Battelle Memorial Institute Report, BMI 720 (1951)

[8]   D. T. Peterson, R. F. Russi and R. L. Nickelson, Amer. Soc. Mech. Eng. Preprint 102 (1955)

[9]   G. G. Bentle, North American Aviation Report, NAA-SR-2069 (1958)

THE DIFFUSION AND SOLUBILITY OF HYDROGEN IN THE ALPHA-PHASE OF ZIRCALOY-2

A. SAWATZKY

Research Metallurgy Branch, Atomic Energy of Canada Limited, Chalk River, Ontario, Canada

The diffusion of hydrogen in the alpha-phase of Zircaloy-2 was measured in the temperature range 260° to 560° C using the gradient technique. The diffusion coefficient was found to be

$$D = 2.17 \times 10^{-3} \exp\left(-8380/RT\right) \text{ cm}^2/\text{sec}.$$

The terminal solid solubility of hydrogen in Zircaloy-2 was determined in the temperature range 260° to 650° C using a modification of the gradient technique. The solubility is given by

$$C_0 = 8.50 \times 10^4 \exp\left(-7600/RT\right) \text{ ppm H}_2$$

by weight.

La diffusion de l'hydrogène dans la phase α du zircaloy-2 a été mesurée entre 260 et 560° C par la technique du gradient. Le coefficient de diffusion déterminé par cette méthode est

$$D = 2,17 \times 10^{-3} \exp\left(-8380/RT\right) \text{ cm}^2/\text{sec}.$$

La solubilité terminale dans l'état solide de l'hydro-gène dans le zircaloy-2 a été déterminée entre 260° et 650° C en utilisant une variante de la technique du gradient. La solubilité est donnée par

$$C_0 = 8,50 \times 10^4 \exp\left(-7600/RT\right) \text{ ppm de H}_2$$

en poids.

Die Diffusion von Wasserstoff in der α-Phase von Zirkaloy-2 wurde im Temperaturbereich von 260° bis 560° C unter Anwendung der Gradientenmethode untersucht. Der Diffusionskoeffizient wurde zu

$$D = 2,17 \times 10^{-3} \exp\left(-8380/RT\right) \text{ cm}^2/\text{sec}$$

ermittelt.

Die maximale Löslichkeit von Wasserstoff in Zirkaloy-2 wurde zwischen 260° und 650° C bestimmt, wobei eine abgewandelte Form der Gradientenmethode verwendet wurde. Die Löslichkeit wird in Gew.-ppm gegeben durch

$$C_0 = 8,50 \times 10^4 \exp\left(-7600/RT\right).$$

1. Introduction

Zircaloy-2 has the properties of low corrosion rate, reasonable strength up to at least 300° C and low neutron absorption, all of which make it desirable as a structural material in water cooled power reactors. One of its chief disadvantages, however, is a drastic reduction in impact strength brought by about the presence of the hydride phase [1]. A knowledge of the hydrogen distribution and the terminal solid solubility is therefore necessary to predict the useful life of Zircaloy in the reactor.

As the Zircaloy-2 pressure tubes in the NPD (Nuclear Power Demonstration) reactor will operate at 260° C it was necessary to know the diffusion rate and the solubility limit of hydrogen in the α-phase of Zircaloy-2 at this temperature. Schwartz and Mallett [2], Mallett and Albrecht [3], and Gulbransen and Andrews [4]

measured the terminal solid solubility of hydrogen in zirconium, but only Mallett and Albrecht made measurements at temperatures as low as 305° C. Extrapolation of these data to 260° C gave terminal solid solubilities of 75, 45 and 28 parts per million (ppm) by weight respectively. Since the last value is similar to the amount of hydrogen normally present in Zircaloy-2 tubing, it was important to establish the terminal solid solubility of hydrogen in Zircaloy-2 at 260° C.

Although the degassing method employed by Eborall and Ransley [6] for determining the diffusion of hydrogen in an Al-Mg alloy was tried, it was decided that the technique used by Mallett and Albrecht [3] for measuring the diffusion of hydrogen in zirconium would give more reliable results in the temperature range of interest. Essentially, the method consists of

determining the hydrogen distribution in a Zircaloy cylinder annealed in hydrogen for a predetermined time.

The diffusion experiment yielded values of terminal solid solubility, but more accurate results were obtained by a modification of this technique. A thin hydride film was formed on a Zircaloy cylinder by reaction with hydrogen and annealed for a time sufficient to homogenize the alpha phase. Hydrogen analysis then gave the terminal solid solubility directly.

2. Experimental Procedure

2.1. MATERIAL

The two sources of Zircaloy-2 with compositions given in table 1 were in the form of rods

TABLE 1

Analysis of the Zircaloy-2
Alloy analysis in wt percent

Element	Ingot FZ-644	Ingot K-28
Sn	1.36	1.51
Fe	0.13	0.15
Cr	0.10	0.10
Ni	0.05	0.05

Impurities in ppm by wt		
N	35	31
C	90	< 300
Si	77	30
Al	38	21
Hf	< 100	72
Cu	< 25	< 20
V	< 25	< 20
Mn	35	< 20
Mg	< 10	< 20
Pb	< 20	< 20
Mo	< 20	< 20
Co	< 10	< 20
W	< 21	< 20
B	< 0.3	< 0.2
Cd	< 0.2	< 0.5
O	< 1200	< 1400
H	45	32

swaged to 0.5 in. diameter. Micrographic examination showed that the FZ-644 batch was in the as-swaged conditions, whereas the K-28 material had been annealed in the alpha region.

2.2. APPARATUS

A schematic diagram of the apparatus is shown in fig. 1. Except for several modifications, it is the hot-extraction apparatus described by McGeary [5]).

The sample furnace consisted of nichrome ribbon wound on a Vycor tybe, and was capable of reaching temperatures up to 1100° C. The manual temperature control using a Variac produced variations of less than $\pm 1°$ C. The working zone of the furnace had a maximum temperature variation of 3° C over 1.5 inches. A chromel-alumel thermocouple made from National Bureau of Standards calibrated wire was placed against the bottom of the sample-tube and calibrated to read sample temperature. The error in specimen temperature was approximately $\pm 5°$ C.

Each of the two high-speed mercury diffusion pumps 1 and 2 had a large cold trap sealed to the high vacuum outlet. Pump No. 1, used to transfer the hydrogen from the sample tube into the analysis volume, attained a pressure of less than 0.01 microns with a back pressure of 1500 microns.

The total analysis volume consisted of the 1050-cc flask, the 2000-cc flask, the McLeod gauge, the tubing and the low vacuum side of pump No. 1. This volume was calibrated by introducing hydrogen into the analysis volume and measuring the pressure with the McLeod gauge. The 1050-cc flask, whose volume had been accurately determined before assembly, was then evacuated and the hydrogen contained in the rest of the volume expanded into it. By measuring the final pressure and applying the perfect gas law the total volume was calculated. Suitable combinations of the two flasks A and B (fig. 1) together with the associated tubing between diffusion pump No. 1 and the McLeod gauge enabled one to have four different analytical volumes.

The palladium valve used to introduce pure hydrogen into the system was a spiral of palladium tubing with a 0.064 cm wall, 0.32 cm diameter and 30 cm length. One end of this
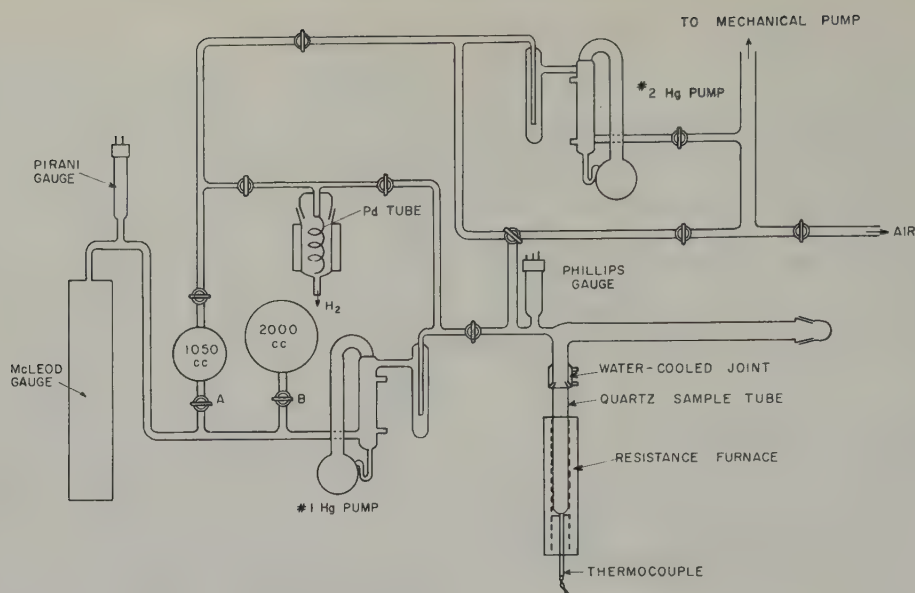
Fig. 1. Hot extraction apparatus for hydrogen analysis.

spiral was silver-soldered to the Kovar tip joined to a short length of glass tubing, and the other end was closed. With the palladium tube at 400° C a hydrogen pressure of 100 mm in the system could be attained in one hour.

2.3. THE DIFFUSION EXPERIMENT

A Zircaloy cylinder 1 cm in diameter and 3 cm long was degassed in vacuum for six hours at 830° C. A residual hydrogen concentration of 5 to 6 ppm by weight as determined from the equilibrium curves, remained in the specimen after this treatment. The sample was abraded with 600-A grit carbide paper and placed in the sample tube of the furnace. It was then heated in vacuo for 0.5 h at 830° C to remove any oxide film and brought to the diffusion temperature. Hydrogen, at a pressure of 200 mm was next introduced into the sample tube; this pressure was sufficient to maintain a hydride film on the specimen surface. The sample was kept at the diffusion temperature for a sufficient time to give a suitable hydrogen distribution, after which the furnace was quickly removed and the sample tube quenched in liquid nitrogen. Lengths equal to the diameter were removed from the end of each sample in order to eliminate effects due to the finite specimen length. The

remaining portion was machined into seven layers of equal weight. The outer layer containing the hydride was discarded and the remaining six analysed for hydrogen.

A plot of concentration versus radius when extrapolated to the sample surface gave the terminal solid solubility C_0. The diffusion coefficient was determined from the plot of $(C - C_1)/(C_0 - C_1)$ versus r/a where:

$C =$ Hydrogen concentration at radius r

$C_1 =$ Initial uniform hydrogen concentration

$C_0 =$ Surface concentration of hydrogen in the α-Zr phase

$a =$ radius of sample.

2.4. DETERMINATION OF THE TERMINAL SOLID SOLUBILITY

Since the terminal solid solubilities obtained by the above method are susceptible to fairly large errors due to extrapolation, a variation of this technique leading to more accurate results was also used.

The Zircaloy used in these measurements was cold-worked 40 % to eliminate possible effects due to differences in the microstructure of the two batches of material. The specimens were 2 cm in length and 0.5 cm in diameter except

for those treated at 260° C which were 0.4 cm in diameter.

Two samples, one from each batch, were placed together in the furnace and given the same degassing and oxide-removal treatment as the diffusion specimens. With the samples at the desired temperature, hydrogen at a pressure of 150 mm was introduced into the sample tube. After the samples had absorbed enough hydrogen to form a hydride skin approximately 0.005 cm thick, the pressure was reduced to a value [7] which was just sufficient to maintain the hydride film without causing further growth. The samples were held at the diffusion temperature for a time $t = a^2/D$ where D is the diffusion coefficient at operating temperature. This time was long enough to give a uniform hydrogen distribution in the alpha phase to within 1 %. Sample dimensions had been chosen to allow homogenization in reasonable times. After removal from the furnace a layer 1 mm thick was machined from the specimen surface to remove the hydride film, and the remaining portion analysed for hydrogen. The resultant concentration was the terminal solid solubility.

2.5. ANALYSIS OF THE DIFFUSION DATA

Since the technique used results in effectively radial diffusion, the diffusion equation becomes:

$$\frac{\partial c}{\partial t} = \frac{D}{r} \frac{\partial}{\partial r}\left(r \frac{\partial c}{\partial r}\right) \qquad (1)$$

where c – concentration

t – time

r – radius

D – diffusion coefficient.

This equation must be solved using the following boundary conditions:

1) $c = C_0$ at $r = a$ for $t \geqslant 0$

2) $c = C_1$ for $0 < r < a$ at $t = 0$.

As shown in Crank [8] the solution to eq. (1) is

$$\frac{C - C_1}{C_0 - C_1} = 1 - \frac{2}{a} \sum_{n=1}^{\infty} \exp\left(-D\alpha_n^2 t\right) \frac{J_0(r\alpha_n)}{J_1(a\alpha_n)} \qquad (2)$$

where $J_0(x)$ and $J_1(x)$ are first-kind Bessel

functions of zero and first order respectively, and the α_n's are the positive roots of $J_0(a\alpha_n) = 0$. The solution to eq. (2) can be written in terms of the two dimensionless parameters Dt/a^2 and r/a. Curves showing $(C-C_1)/(C_0-C_1)$ as a function of r/a for different values of Dt/a^2 may be found in Crank's book.

In practice the experimental values of $(C-C_1)/(C_0-C_1)$ are plotted against r/a and compared with the theoretical curves. A value for Dt/a^2 is thus obtained and, since t and a are known, D can be calculated. The experimental conditions are chosen so that a thin hydride film is formed on the sample. The hydrogen concentration in the Zircaloy that is in equilibrium with the hydride, namely the terminal solid solubility, is then C_0 in the above equation.

3. Results and Discussions

3.1. DIFFUSION COEFFICIENTS

The diffusion of hydrogen in the alpha-phase of Zircaloy-2 was investigated in the range 260° to 560° C. The plot of $(C-C_1)/(C_0-C_1)$ against r/a for 358° C, which is typical of the curves obtained, is shown in fig. 2. The points are the experimental values and the line is the best theoretical fit from which D was determined. Scatter for small values of $(C-C_1)/(C_0-C_1)$ as observed in most of the curves is to be expected since the relative error increases as C approaches C_1.

TABLE 2

Diffusion of hydrogen in Zircaloy-2

Temp. (° C)	Time (min)	Batch No.	$D \times 10^6$ (cm²/sec⁻¹)	C_0 (ppm by wt) uncorr.	C_0 (ppm by wt) corr.
261	150	K-28	0.80	75	71
315	90	K-28	1.70	115	105
358	60	K-28	2.94	300	280
408	30	FZ-644	4.71	180	145
458	15	FZ-644	5.49	490	450
515	15	K-28	10.3	800	700
560	15	K-28	15.8	—	—

The diffusion coefficients obtained at the various temperatures are tabulated in table 2. The values of C_0 obtained by extrapolating the

concentration curves to the sample surfaces are also given.

The assumption is usually made [3]) that the hydride film is negligibly thin. Using the data of Gulbransen and Andrew [9]) for the diffusion of hydrogen in zirconium hydride, the hydride thickness was determined, and a value for C_0 found by extrapolating the concentration curve only to the hydride boundary. As shown in table 2 the correction was appreciable. These corrected values fell reasonably close to the C_0's obtained by the second method used, except for the point at 408° C. The uneven hydriding of this specimen may explain the very low value for C_0. A corrected D was obtained using the corrected C_0 and assuming the average specimen radius to be midway between the specimen surface and the hydride boundary. The correction here was found to be negligible as shown in fig. 2.

The logarithm of D versus $1/T$ is plotted in fig. 3. A least-squares fit of the experimental data gives an activation energy $Q = 8380 \pm 400$ cal/mole and a diffusion coefficient

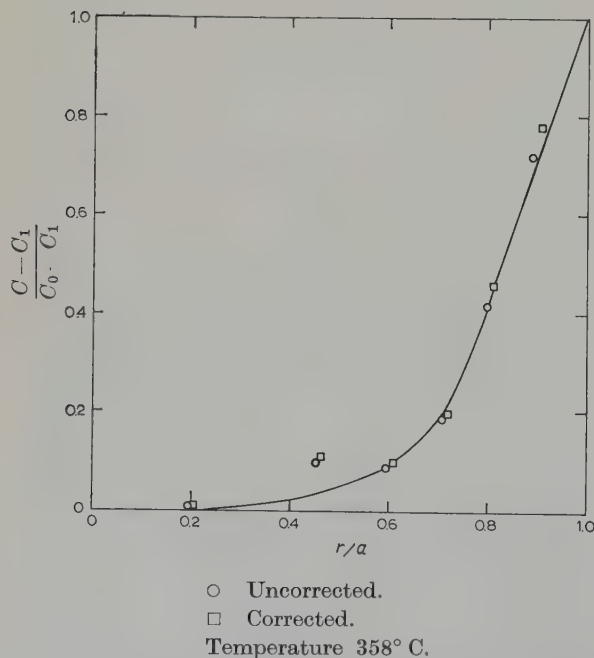$$D = 2.7 \times 10^{-3} \exp(-8380/RT) \text{ cm}^2/\text{sec}.$$

○   Uncorrected.
□   Corrected.
Temperature 358° C.

Fig. 2.   Normalized hydrogen concentration against radius.

○   Present work.
△   Schwartz and Mallett.
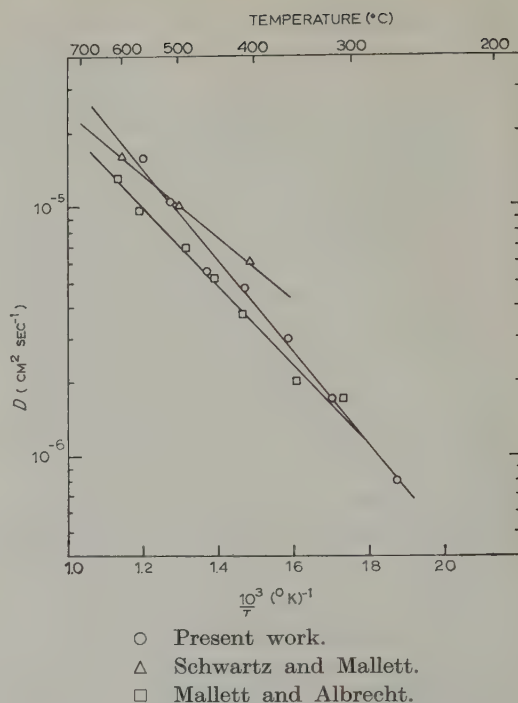□   Mallett and Albrecht.

Fig. 3.   Comparison of diffusivities.

In the same figure the present data are compared with those of Schwartz and Mallett [2]) and Mallett and Albrecht [3]) for the diffusion of hydrogen in zirconium. Although the diffusivities at any one temperature are quite similar in the three cases, the activation energy obtained in the present investigation (8380 cal/mole) is somewhat higher than those of either Schwartz and Mallett (5700 cal/mole) or Mallett and Albrecht (7060 cal/mole). It should be noted that Schwartz and Mallett's result is based on only three measurements. The two different activation energies obtained for hydrogen diffusion in zirconium are possibly due to different amounts of impurities such as oxygen or nitrogen in the zirconium used. Zircaloy-2 contains the four alloying elements shown in table 1, which undoubtedly contribute to the difference in activation energy between hydrogen diffusion in zirconium and Zircaloy-2.

3.2.   TERMINAL SOLID SOLUBILITIES

Terminal solid solubilities were measured in the range 260° to 650° C by the second method described earlier. Table 3 lists the solubilities

TABLE 3

Terminal solid solubilities for H in Zircaloy-2

Temp. (°C)	Time (hours)	C_0 (ppm by wt)		C_0 (average)
		FZ-644	K-28	
257	20	79	81	
257	18	76	50	71
300	11	93	95	
300	11		87	
300	12	99	101	95
356	11	212	218	
356	13	189	191	203
406	4	273	268	270
460	3.5	478	468	
457	7	480	465	473
500	4	635	640	638
560	4	888	886	887
600	2	3075		3075
650	2	3200	3170	3185

obtained for the two batches of Zircaloy tested. In general the reproducibility is quite good, and it was also found that the terminal solid solubility for the two materials is essentially the same.

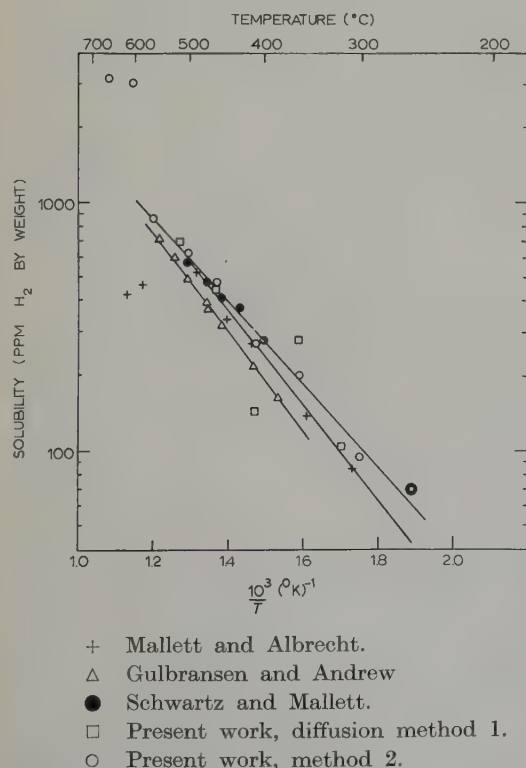The logarithm of C_0 versus $1/T$ is plotted in

+   Mallett and Albrecht.
△   Gulbransen and Andrew
●   Schwartz and Mallett.
□   Present work, diffusion method 1.
○   Present work, method 2.

Fig. 4. Comparison of terminal solid solubilities.

fig. 4. A least-squares fit of the experimental data yields

$\Delta_H = 7600 \pm 200$ cal/mole and

$C_0 = 8.50 \times 10^4 \exp(-7600/RT)$ ppm H_2 by weight.

Δ_H represents the difference in partial molar heats of solution of hydrogen in the δ(hydride) and α phases. The least-squares value of the solubility at 260° C is 64 ppm whereas the average of four determinations at 257° C is 71 ppm.

In fig. 4, the solubility of hydrogen in Zircaloy-2 found in the present investigation is compared with the published values for the solubility of hydrogen in zirconium. The data of Schwartz and Mallett [2], Mallett and Albrecht [3] and Gulbransen and Andrew [4] extrapolated to 260° C lead to terminal solid solubilities of 75, 45 and 28 ppm H_2 by weight respectively. Although the present solubility of hydrogen in Zircaloy-2 (64 ppm) agrees best with that of Schwartz and Mallett, the latter covered only the temperature range 400° to 500° C making extrapolation to 260° C rather unreliable. However, on the basis of probable errors in the hydrogen analyses and temperatures, the present solubilities are accurate to within ± 10 %.

It will be seen that at 600° C and 650° C the results fall off the straight line shown in fig. 4. Metallographic examination of these two samples showed that they had been annealed in the beta region. This shows that the α-phase was not in equilibrium with the δ-phase at these temperatures, in agreement with the equilibrium diagram of Ells and McQuillan [7].

On the basis of this diagram, in a diffusion experiment carried out between 560° to 850° C, one should get a hydride (δ-phase) layer on the specimen surface, followed by a layer of β (bcc) phase, the rest of the specimen being α (hcp) phase. If the annealing was carried out for a long time, the α-phase region would gradually give away to the β-phase. The specimens corresponding to the points at 600° C and 650° C in fig. 4 were annealed for two hours, which left the major portion of these specimens

in the β-phase, thus accounting for the observed higher hydrogen concentrations. In contrast, the two samples at 600° C and 650° C studied by Mallett and Albrecht were annealed for approximately five minutes. The major portion of their samples would be in the α-region, giving values of C_0 nearly equal to the terminal solubility at 560° C. As seen in fig. 4, their values for C_0 at temperatures above 560° C are slightly lower than expected according to Ells and McQuillan.

4. Conclusions

The diffusion coefficient of hydrogen in Zircaloy-2 is

$$D = 2.17 \times 10^{-3} \exp(-8380/RT) \text{ cm}^2/\text{sec}.$$

The terminal solid solubility of hydrogen in Zircaloy-2 is

$$C_0 = 8.50 \times 10^4 \exp(-7600/RT) \text{ ppm } H_2$$

by weight.

Acknowledgements

References

[1] W. L. Mudge, Jr., Zirconium and Zirconium Alloys (American Society for Metals, Cleveland, 1953)
[2] C. M. Schwartz and M. W. Mallett, Trans. A.S.M. **46** (1954) 640
[3] M. W. Mallett and W. M. Albrecht, Jour. Electrochem. Soc. **104** (1957) 142
[4] E. A. Gulbransen and K. F. Andrew, Trans. AIME **203** (1955) 136
[5] R. K. McGeary, Zirconium and Zirconium Alloys (American Society for Metals, Cleveland, 1953)
[6] R. Eborall and C. E. Ransley, Journ. Inst. Metals **71** (1945) 525
[7] C. E. Ells and A. D. McQuillan, Journ. Inst. Metals **85** (1956) 89
[8] J. Crank, Mathematics of Diffusion (Oxford, 1956) p. 66
[9] E. A. Gulbransen and K. F. Andrew, J. Electrochem. Soc. **101** (1954) 560

ETUDE AUX NEUTRONS DE LA TEXTURE CRISTALLINE DE BARREAUX D'URANIUM

Mme J. LANIESSE †, P. MERIEL †† et M. ENGLANDER †

Centre d'Etudes Nucléaires de Saclay, Gif-sur-Yvette (S & O), France

L'étude des textures par diffraction de neutrons a été appliquée à un élément de barreau d'uranium filé en phase α à 600° C. Dans le cas de détermination de texture par diffraction de rayons X, pour les corps absorbants, la couche intéressée par le faisceau est faible : il est donc nécessaire de faire les analyses sur un grand nombre de coupes pour obtenir un résultat statistique. Les neutrons étant peu absorbés par la plupart des substances de poids atomique élevé, il est possible d'obtenir en une seule série d'essais une image statistique correcte de la texture. L'échantillon est un cylindre de 5 cm³ environ dont l'axe, perpendiculaire à la direction de filage, coïncide avec celui d'un faisceau de neutrons monochromatiques ($\lambda = 1,143$ Å). Le détecteur de neutrons est un compteur BF₃ qui décrit dans un plan horizontal un cercle centré sur l'échantillon. Un spectre de diffraction effectué sur un élément de barre d'uranium filé en phase α et traité en phase β a montré que cet échantillon ne présentait qu'une faible orientation préférentielle. Par contre, sur l'échantillon brut de filage il apparaît une texture marquée [110] dans la direction de filage. Les résultats obtenus sont en accord avec ceux déterminés par diffraction de rayons X par différents auteurs sur des barres d'uranium filées en phase α ou laminées en phase α.

The method of studying textures by neutron diffraction has been applied to uranium bar extruded in the α range at 600° C. When textures are determined by X-ray diffraction, the thickness of metal through which the X-ray beam can pass is slight in the case of absorbent materials; it is therefore necessary to carry out analyses on a large number of sections to obtain a statistically significant result. Since neutrons are not strongly absorbed by most substances of high atomic weight, it is possible by means of a single series of experiments to obtain a good statistical image of the texture. The specimen is a cylinder of about 5 cm³, the axis of which, normal to the direction of drawing, coincides with the axis of a beam of monochromatic neutrons ($\lambda = 1.143$ Å). The neutron detector is a BF₃ counter which describes a circle in a horizontal plane, centred on the specimen. The diffraction spectrum obtained from a piece of uranium bar, extruded in the α-range and treated in the β-range, has shown that this specimen has only a weak degree of preferred orientation, whereas an as extruded specimen shows a marked [110] texture in the direction of extrusion. The results obtained are in agreement with those determined by X-ray diffraction by various authors with uranium bars extruded or rolled in the α-range.

An einer Probe aus einem Uranstab, der bei 600° C in der α-Phase durch Strangpressen hergestellt wurde, ist eine Texturuntersuchung durch Neutronenbeugung vorgenommen worden. Führt man Texturbestimmungen mit Röntgenstrahlen durch, so ist für absorbierende Körper die von dem Strahlenbündel erfasste Schicht sehr dünn: daher ist es notwendig, die Untersuchungen an zahlreichen Schnitten vorzunehmen, um ein statistisches Ergebnis zu erhalten. Da dem gegenüber Neutronen von den meisten Elementen mit höherem Atomgewicht nur wenig absorbiert werden, kann man in einer einzigen Versuchsreihe ein richtiges statistisches Bild von der Textur erhalten. Die verwendete Probe ist ein Zylinder von etwa 5 cm³ Volumen, dessen Achse senkrecht zur Strangpressrichtung steht und mit der Achse des Bündels monochromatischer Neutronen ($\lambda = 1,143$ Å) zusammenfällt. Als Neutronenindikator diente ein BF₃-Zähler, der in horizontaler Ebene einen Kreis mit der Probe als Mittelpunkt beschrieb. Aus dem Beugungsspektrum einer Probe, die aus dem durch Strangpressen in der α-Phase hergestellten und in der β-Phase wärmebehandelten Uranstab stammte, war zu entnehmen, dass eine solche Probe nur eine schwache Orientierung aufweist. Dagegen zeigt sich bei einer Probe, die direkt nach dem Strangpressen entnommen wird, eine ausgeprägte [110]-Textur in Strangpressrichtung. Die erhaltenen Befunde stimmen überein mit Ergebnissen aus Röntgenbeugungsmessungen, welche von verschiedenen Autoren an stranggepressten oder gewalzten Uranstäben vorgenommen worden sind.

† Service de Technologie.
†† Service de Physique des Solides et Résonance Magnétique.

1.   Barreaux bruts de filage en phase α

La déformation de barreaux d'uranium sous irradiation est conditionnée, toutes choses égales par ailleurs, par deux facteurs essentiels: la grosseur des grains et leur orientation.

De nombreuses expériences ont montré que, pour limiter les déformations, il était nécessaire (mais non suffisant) d'avoir des barreaux formés d'agrégats polycristallins à la fois homogènes et exempts d'orientations préférentielles.

On est conduit pour se rapprocher de ces conditions à déformer l'uranium en phase α, à le soumettre ensuite à des traitements thermiques en phase β, qui éliminent les orientations préférentielles dues à la déformation, puis en phase α, qui provoquent l'affinage par recristallisation et éliminent les contraintes résiduelles.

Les résultats ont montré que les déformations sous irradiation de barreaux ainsi traités étaient effectivement nettement inférieures à celles de barreaux d'uranium coulés ou filés en phase α ou γ sans recuit, sans être toutefois entièrement éliminées.

Il reste probablement après traitements thermiques un résidu d'orientations préférentielles complexes, d'où l'intérêt d'étudier l'évolution de la texture des barreaux d'uranium au cours des différents traitements thermiques.

L'étude des orientations préférentielles dans un échantillon polycristallin s'effectue commodément au moyen des rayons X, dans la mesure où l'échantillon n'est pas trop absorbant. Dans le cas contraire, différents procédés fort ingénieux ont été mis en œuvre [1–6]. Ils présentent tous cependant les inconvénients suivants:

a) le faisceau n'intéresse qu'une faible couche superficielle de l'échantillon,

b) il en résulte que le nombre des microcristaux diffusants est faible, d'autant plus faible que le grain est plus gros, et qu'on doit souvent répéter les analyses sur différentes coupes de l'échantillon pour obtenir une image statistique correcte de la texture.

A ce point de vue, les neutrons présentent l'avantage, par rapport aux rayons X, d'être peu absorbés, sauf cas exceptionnels, par les substances constituées d'atomes de poids atomique élevé. L'étude d'une texture cristalline au moyen des neutrons présente alors les avantages suivants:

a) Tous les cristallites d'un échantillon massif dont le volume peut atteindre plusieurs cm³ participent à la diffusion.

b) On peut donc obtenir en une seule série d'essais une image correcte de la texture, la statistique portant sur un nombre de grains suffisant.

La méthode a déjà été mise en œuvre pour étudier l'influence du recuit sur la texture cristalline de fils métalliques [7]. Au moyen du spectromètre à neutrons de la pile EL 3 de Saclay, nous avons étudié la texture cristalline d'une barre d'uranium brute de filage en phase α. Cette barre a été obtenue par filage à 600° C d'une billette de 90 mm de diamètre, le diamètre final étant 27,8 mm.

2.   Dispositif expérimental

L'échantillon est un cylindre découpé dans la barre de manière que son axe soit perpendiculaire à l'axe de filage de la barre (fig. 1). Sur une face plane du cylindre, la direction de filage a été repérée. Ce cylindre a 19 mm de hauteur et
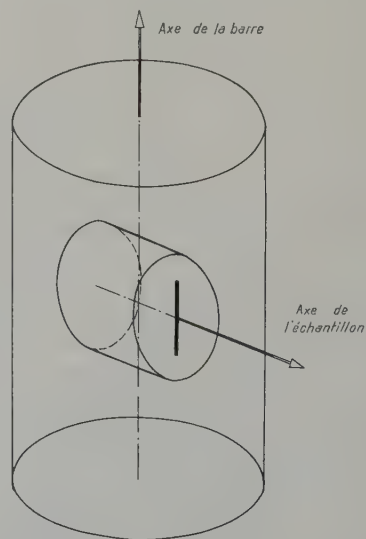

Fig. 1.   Schéma du mode de prélèvement de l'échantillon dans la barre filée.

de diamètre (volume 5,4 cm³). Le diamètre moyen des grains étant de l'ordre de 100 μ, l'échantillon en contient quelques millions. Il est placé dans un faisceau monochromatique de neutrons ($\lambda = 1,143$ Å), l'axe du cylindre coïncidant avec celui du faisceau (fig. 2). Si l'on pouvait placer en P normalement à l'axe du faisceau (fig. 2) une plaque sensible aux neutrons, celle-ci enregistrerait une série d'anneaux de Debye-Scherrer de densité non uniforme. En fait, le détecteur de neutrons dont on dispose est un compteur à BF₃ qui décrit dans le plan horizontal un cercle centré sur l'échantillon. On réalise néanmoins l'équivalent du dispositif de la plaque sensible en laissant fixe le compteur au maximum d'intensité de la réflexion de Bragg étudiée, et en enregistrant les variations d'intensité quand on fait tourner l'échantillon autour de son axe, c'est à dire quand on fait défiler devant le compteur les génératrices du cône de Debye-Scherrer correspondant à la réflexion étudiée.
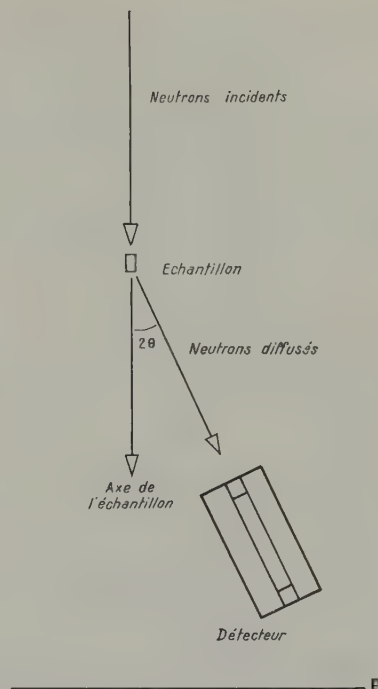
3. Résultats

Un spectre de diffraction ordinaire a tout d'abord été réalisé au moyen d'un échantillon ayant subi 4 traitements β suivis d'un traitement α. Nous nous sommes ensuite assurés que l'échantillon ne donnait qu'une faible orien-

Fig. 2.   Principe du dispositif expérimental.

tation préférentielle. Ce spectre (fig. 3) montre que les raies intéressantes à étudier sont les raies nettement séparées (111), (112), (131) assez intenses, et éventuellement (020), (022) et (130). Le paquet de raies (110), (021), (002) ne peut malheureusement donner d'indication bien
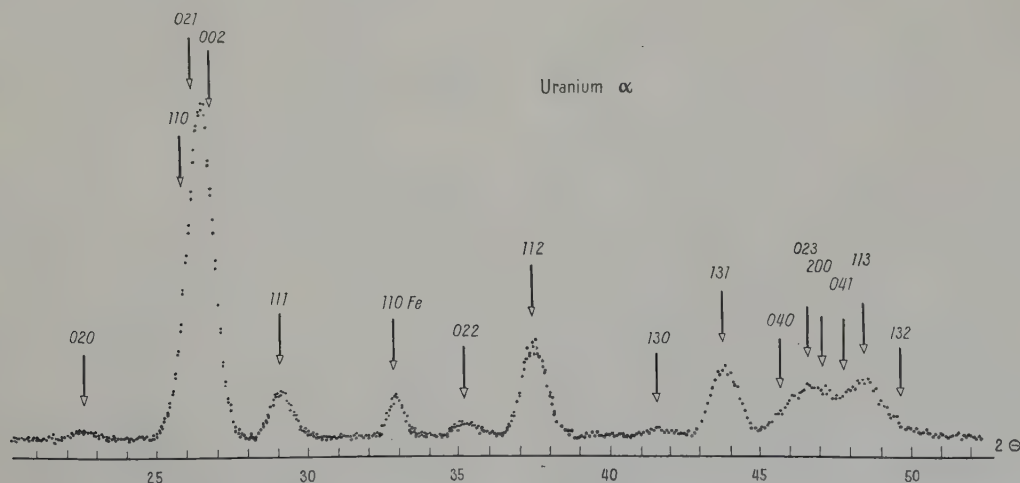

Fig. 3.   Spectre d'un échantillon d'uranium filé traité ne présentant qu'une faible orientation préférentielle.
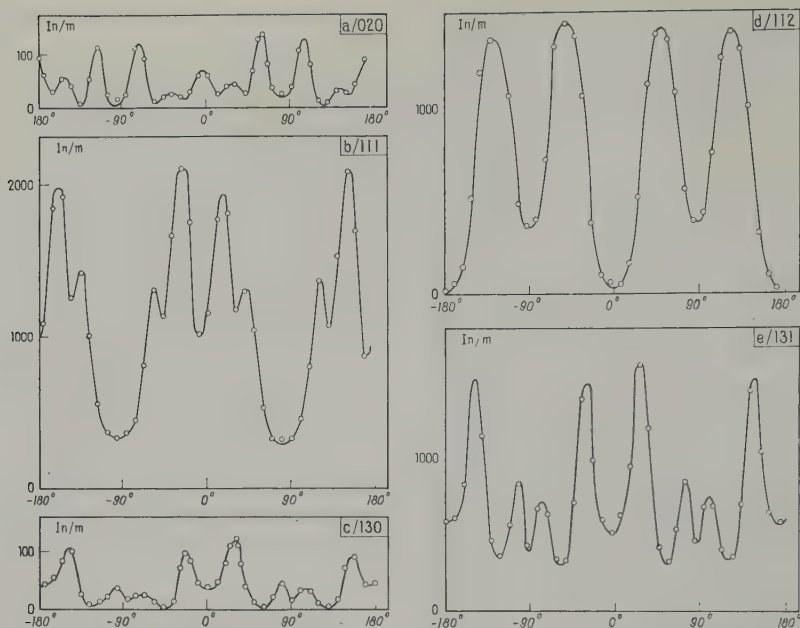
Fig. 4. Variation d'intensité des cinq raies étudiées a: (020), b: (111), c: (130), d: (112), e: (131) en fonction de l'angle de la direction de l'axe de fibre avec la verticale.

précise. Nous nous en sommes néanmoins servis en fin d'étude pour confirmer les résultats obtenus.
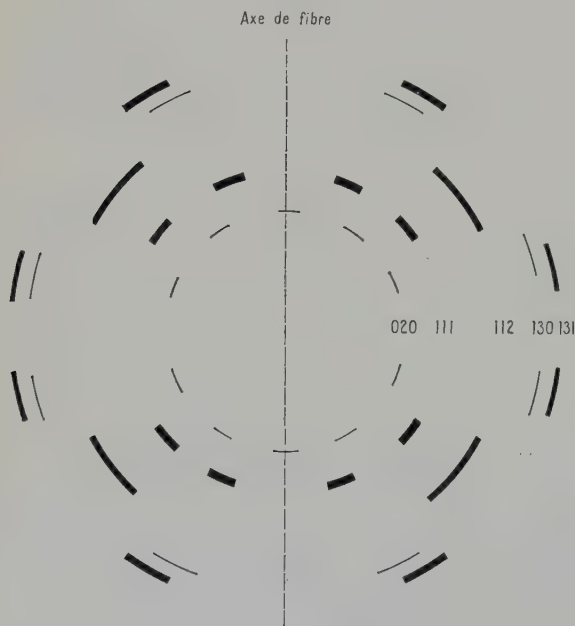

Fig. 5. Diagramme qu'aurait enregistré une plaque sensible aux neutrons, placée normalement au faisceau incident en P fig. 2.

La figure 4 représente la variation d'intensité des cinq raies étudiées en fonction de l'angle fait par la direction de l'axe de fibre avec la verticale. La figure 5 donne une image des résultats qu'aurait enregistrés une plaque placée en P (fig. 2). La construction d'Ewald (fig. 6) montre que l'angle φ_{hkl} entre la direction FF' de l'axe de fibre et le rayon qui joint le centre du cliché au centre d'une tache T de l'anneau (hkl) est relié à l'angle φ_{0hkl} entre l'axe de fibre et le vecteur $\overrightarrow{OM}_{hkl}$ du réseau réciproque ayant donné naissance à la tache T par la relation:

$$\cos \varphi_{0hkl} = \cos \varphi_{hkl} \cdot \cos \theta_{hkl}.$$

En ne considérant d'abord que les maxima les plus intenses des réflexions étudiées, on obtient les résultats du tableau 1. Connaissant les

TABLEAU 1

hkl	φ_{hkl}	θ_{hkl}	φ_{0hkl}
020	67°	11° 13'	67,5°
111	22°	14° 30'	26°
112	52°	18° 39'	54,5°
130	26,5°	20° 52'	33°
131	30,5°	21° 50'	37°
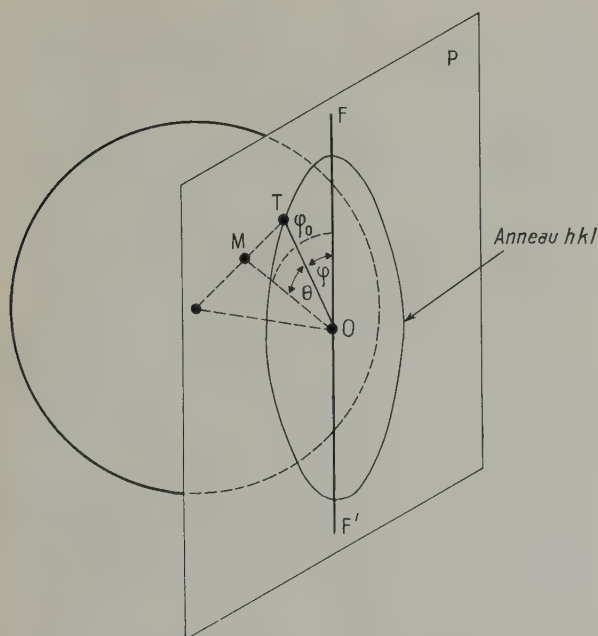
Fig. 6. Construction d'Ewald.

angles φ_{0hkl} des vecteurs $\overrightarrow{OM}_{hkl}$ du réseau réciproque avec la direction de l'axe de fibre, cette direction est, dans ce réseau, celle de la génératrice commune à tous les cônes d'axes $\overrightarrow{OM}_{hkl}$ d'origine O et de demi-angles au sommet φ_{0hkl}. La figure 7 représente la projection stéréographique de cette construction, le pôle de projection étant le nœud (110). On voit que la direction de l'axe de fibre est très voisine de la direction [110] du réseau réciproque.
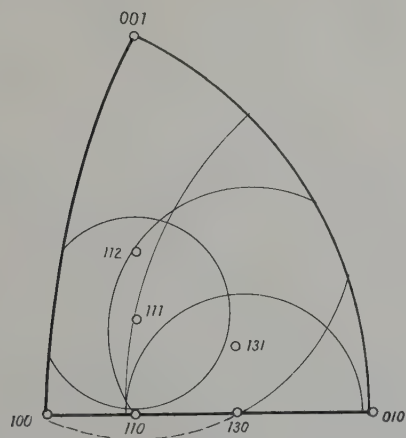

Fig. 7. Projection stéréographique en prenant le noeud (110) comme pôle de projection.

On peut alors calculer les angles φ_{0hkl} que fait la direction [110] du réseau réciproque avec les différentes directions $\overrightarrow{OM}_{hkl}$ de la forme $\{hkl\}$ et vérifier que les maxima secondaires des anneaux de Debye-Scherrer qui n'ont pas encore été pris en compte correspondent bien à ces nouveaux angles. Le tableau 2 donne le

TABLEAU 2

hkl	φ_{0hkl}calc	φ_{0hkl}exp
020		11°
		34°
	64°	67,5°
111	27,5°	26°
	57°	52°
112	46°	54,5°
	64,5°	
130	29,5°	33°
	81,5°	76,5°
131	34°	37°
	82°	78°

résultat obtenu. La proximité des deux angles φ_0 calculés pour les réflexions de la forme $\{112\}$ explique en particulier la largeur des pics trouvés dans le cas de la réflexion (112) (fig. 4d), et pourquoi le cercle (112) de la figure 7 ne passe pas par le point d'intersection des quatre autres. Seuls les maxima secondaires de la réflexion faible (020) ne s'expliquent pas par l'existence d'un axe de fibre dirigé suivant [110]. Par contre, on peut, avec cette hypothèse, calculer les angles auxquels il faut placer l'échantillon pour obtenir les maxima d'intensité des raies (110), (021), (002) (0, 68, 90 degrés respectivement). La figure 8 donne les formes du paquet des trois raies pour ces angles, le spectre étant obtenu en couplage $\theta/2\theta$. On voit que pour chacun de ces angles, seule la raie correspondante apparaît, les deux autres ayant pratiquement disparu. En outre, comme on pouvait le prévoir, le maximum de la réflexion (110) est particulièrement intense.
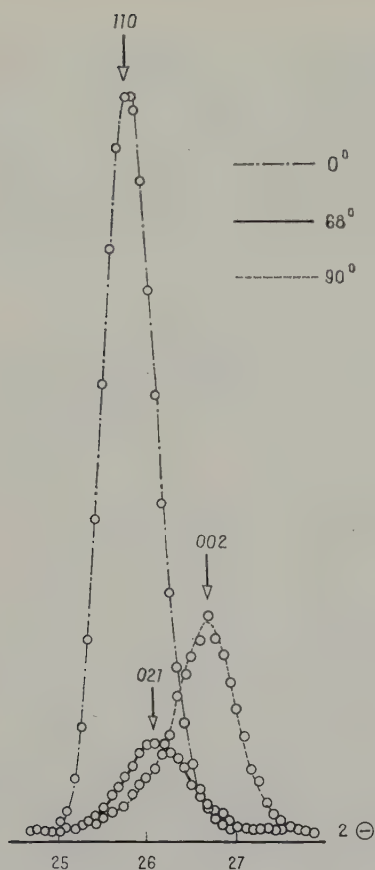
Fig. 8. Forme des trois raies (110), (002) et (021) pour les valeurs 0°, 68° et 90° des angles auxquels il faut placer respectivement l'échantillon pour obtenir les maxima d'intensité de raie.

4. Conclusion

Jetter et McHargue [8]) ont étudié aux rayons X la texture de barres d'uranium obtenues par filage à 500° C. Leurs résultats, représentés en figures de pôles inverses montrent l'existence de deux directions privilégiées, l'une voisine de [110] du réseau réciproque, l'autre de [010]. D'après leurs résultats, la proportion de cristaux appartenant à la texture [110] croit au profit de l'autre quand le rapport de réduction par extrusion augmente. En accord avec une étude de Calnan et Clews [9]), Harris [10]) étudie la texture de barres d'uranium laminées et montre que le même phénomène se produit quand le rapport de réduction par laminage et la température à laquelle s'effectue le laminage augmentent. La barre ayant été filée à 600° C avec un rapport de réduction de 10,5, le fait que nous n'ayons pas décelé de texture suivant [010] est compatible avec ces résultats.

Bibliographie

[1]) L. G. Schulz, J. Appl. Phys. **20** (1949) 1030

[2]) A. N. Holden, Rev. Sci. Instr. **24** (1953) 10

[3]) L. K. Jetter et B. S. Borie, J. Appl. Phys. **24** (1953) 532

[4]) W. P. Chernock *et al.*, Rev. Sci. Instr. **24** (1953) 925

[5]) M. H. Mueller et H. W. Knott, Rev. Sci. Instr. **25** (1954) 1115

[6]) A. Winogradski, Rev. Métall. **51** (1954) 597; C. R. Acad. Sci. **240** (1955) 2235

[7]) R. A. Swalin et A. H. Geisler, Trans. AIME **206** (1956) 1259

[8]) L. K. Jetter, C. J. McHargues et R. O. Williams, J. Appl. Phys. **27** (1956) 368

[9]) E. A. Calnan et C. J. B. Clews, Phil. Mag. **43** (1952) 93

[10]) G. B. Harris, Phil. Mag. **43** (1952) 113

DÉTERMINATION DU POUVOIR THERMO-ÉLECTRIQUE DE L'URANIUM ET DU PLUTONIUM

P. COSTA

Service de Radiométallurgie, Centre d'Etudes Nucléaires de Fontenay-aux-Roses (Seine), France

Les pouvoirs thermo-électriques de l'uranium et du plutonium ont été mesurés par une méthode différentielle. En accord avec les mesures précédentes de Waldron et Lee, on a trouvé pour le plutonium un pouvoir thermo-électrique élevé pour la phase α ainsi que les phases β et γ, faible pour les phases de haute température δ et ε, surtout δ. Ce dernier résultat exclut l'explication du coefficient de dilatation négatif en phase δ avancée par Varley. Les variations observées du pouvoir thermo-électrique avec la température sont un peu différentes de celles rapportées par Waldron et Lee.

The thermoelectric power of uranium and plutonium have been measured by a differential method. In agreement with previous measurements by Waldron and Lee, a high value of thermoelectric power has been found for the α and β phases of plutonium, and a low value for the δ and ε phases, particularly the δ. This last result rules out Varley's explanation for the negative thermal expansion coefficient of the β phase. The observed variation of the thermoelectric power with temperature is slightly different from that reported by Waldron and Lee.

Die thermoelektrische Kraft des Urans und des Plutoniums wurden mittels einer differentiellen Methode gemessen. In Einklang mit den früheren Messungen von Waldron und Lee wurde eine hohe Thermokraft für die α und β Phasen des Plutoniums gefunden, und eine niedrige für die δ und ε Phasen, besonders die erstere. Dieses Ergebnis schliesst Varleys Erklärung des negativen Ausdehnungskoeffizienten von δ-Plutonium aus. Der Temperaturgang der Thermokraft war etwas anders als der von Waldron und Lee berichtete.

1. Introduction

On sait que dans l'approximation des bandes le pouvoir thermo-électrique est directement lié à la dérivée en fonction de l'énergie du nombre d'électrons au voisinage du niveau de Fermi.

Dans un travail récent [1]), Varley propose une explication du coefficient de dilatation négatif observé pour le Plutonium en phase δ, explication qui implique une dérivée fortement positive du nombre d'électrons en fonction de l'énergie, au niveau de Fermi.

Il était intéressant de confronter cette hypothèse avec l'expérience. Comme nous disposions de peu de métal, nous avons utilisé le montage décrit plus loin que nous a suggéré Crussard. Waldron et Lee ont publié à la Conférence de Genève [2]) une série de résultats sur le pouvoir thermo-électrique du Plutonium pur que nous comparons aux nôtres.

2. Principe de la mesure et dispositif expérimental

Etant donné les quantités de métal dont nous disposions, nous avons été conduits à adopter pour nos expériences le montage suivant [3]) schématisé sur la figure 1.

Le fil F dont on veut mesurer le pouvoir thermo-électrique, long d'une dizaine de centimètres, est soudé à chacune de ses extrémités à 2 fils de 2 métaux étalons M_1 et M_2. Les quatre extrémités libres de ces fils sont à leur tour soudées à des fils de cuivre, ces quatre dernières
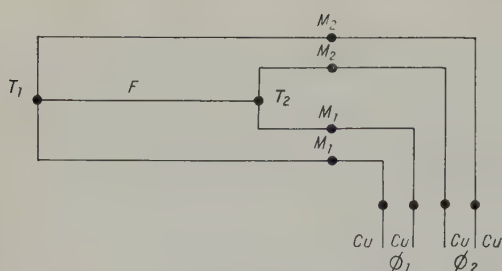
Fig. 1. Schéma des connexions.

soudures étant maintenues à la température constante de 0° C dans un vase Dewar contenant un mélange d'eau et de glace.

L'ensemble du montage est placé dans un four de telle façon que les deux extrémités du fil F soient à des températures différentes.

On enregistre en continu, sur deux potentiomètres les différences de potentiel ϕ_1 et ϕ_2 aux bornes des circuits M_1FM_1 et M_2FM_2.

$$\phi_1 = \int_{T_a}^{T} (S_{M_1} - S_F)\,dT, \qquad \phi_2 = \int_{T_a}^{T_b} (S_{M_2} - S_F)\,dT$$

(T_a et T_b étant les températures des deux extrémités du fil).

Si l'on admet des variations linéaires du pouvoir thermo-électrique S dans les intervalles de température considérés, ceci peut s'écrire :

$$\phi_1 = (T_b - T_a)(S_{M_1} - S_F), \quad \phi_2 = (T_b - T_a)(S_{M_2} - S_F)$$

$$\boxed{S_F = S_{M_2} + (S_{M_1} - S_{M_2}) \frac{\phi_1}{\phi_1 - \phi_2}.}$$

3. Détail du montage

L'ensemble du montage décrit plus haut est placé dans un bloc de cuivre démontable dont une moitié a été représentée sur la figure 2. Il a pour rôle de régulariser le gradient entre les deux extrémités du fil. Les fils sont isolés et protégés par des gaines de zircone pure frittée.

L'ensemble de cet équipage est maintenu dans l'axe d'un tube laboratoire horizontal en silice, qui constitue l'enceinte à vide. Le four est mobile par rapport au tube, ce qui permet le cas échéant de modifier la différence $(T_a - T_b)$ et de faire en sorte qu'elle soit de l'ordre de 30°.

Les soudures ont été faites sur une machine à souder par points qui a été montée dans la même boîte à gants que le four.

Les conditions expérimentales de montage en boîte à gants nous ont obligés à couper nos fils étalons; aux jonctions complémentaires ainsi créées entre les parties fixes des fils et celles qui sont soudées sur l'échantillon, les contacts sont assurés par serrage.

Nous avons vérifié que ces jonctions créent, dans un circuit constitué par un métal unique, entre deux soudures froides à 0° C une différence de potentiel thermo-électrique qui reste constamment inférieure à 10^{-2} millivolt et qui ne subit aucune variation brutale.

Nous avons utilisé comme métaux étalons le chromel et l'alumel d'une part, le platine et l'alliage platine-rhodium à 10 % d'autre part. C'est pour améliorer la sensibilité de la méthode (qui est comme nous allons le voir fonction des étalons choisis) et pour éviter les diffusions à l'état solide que nous avons été conduits à adopter les premiers pour l'uranium sur lequel nous avons fait une série d'expériences préliminaires, les seconds pour le plutonium.

Il nous a fallu procéder à un étalonnage préalable de l'alumel par rapport au platine pour avoir son pouvoir thermo-électrique.

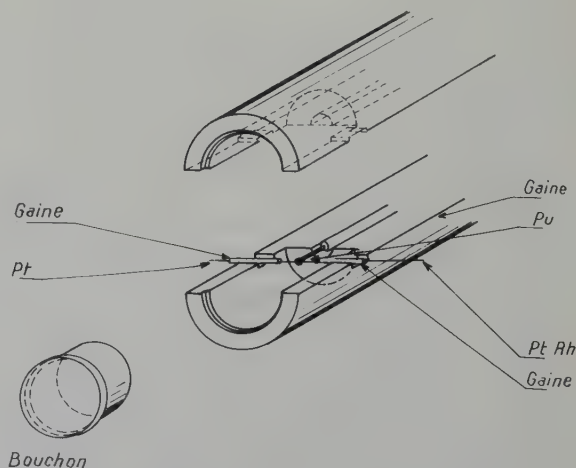Les valeurs du pouvoir thermo-électrique absolu du platine que nous avons adoptées sont celles données par Borelius [4]).

Fig. 2. Détail du montage.

4. Sensibilité de la méthode

L'inconvénient de cette méthode réside évidemment dans le nombre important des jonctions, ce qui accumule les sources d'erreur. En outre, il est clair qu'une hétérogénéité même faible de l'échantillon peut provoquer une erreur importante si le fil présente un point chaud dont la température est notablement supérieure à celle de son extrémité chaude.

C'est pour éviter cet inconvénient que nous avons placé l'échantillon dans un bloc de cuivre.

Elle présente par contre l'avantage de donner directement l'indication physique intéressante, c'est-à-dire le pouvoir thermo-électrique.

Il est évident que les conditions optima de sensibilité sont réunies lorsque le pouvoir thermo-électrique de l'échantillon est intermédiaire entre ceux des deux métaux étalons. Il est alors indépendant du choix des étalons. Par contre si $|S_F - S_{M_1}| \gg |S_{M_1} - S_{M_2}|$, la sensibilité de la mesure devient, toutes choses égales par ailleurs, très mauvaise. On a en effet, si l'on admet sur chaque mesure ϕ_1 et ϕ_2 une erreur η indépendante de la mesure :

$$\Delta S = \frac{\eta}{T_a - T_b} \times \frac{|S_{M_1} - S_{M_2}| + |S_{M_2} - S_F|}{|S_{M_1} - S_{M_2}|}. \quad (2)$$

L'uranium a un pouvoir thermo-électrique fort et positif. Platine et platine rhodié ont, par contre, des pouvoirs thermo-électriques voisins et négatifs : nous leur avons préféré l'alumel et le chromel dont les pouvoirs thermo-électriques encadrent jusqu'à 600° C celui de l'uranium.

5. Mesures

5.1. URANIUM

Nous avons fait d'une part sur un même échantillon une série de mesures en phase α sans dépasser la température de transformation (665°) et d'autre part plusieurs cycles de mesures avec passage en phase γ. Dans ces dernières expériences, la diffusion des composés du chromel et de l'alumel dans l'uranium étant importante, nous avons, après chaque essai coupé à chaque extrémité les zones de soudure.

Les résultats, portés sur la figure 3, sont légèrement différents au chauffage et au refroidissement et se situent de part et d'autre des valeurs données par Dahl et Van Dusen [5]).

Cette différence est sans doute due à une hétérogénéité du métal, même faible, associée à un gradient de température variable d'une extrémité à l'autre. Il est à noter que le fil était constitué de très gros cristaux. Elle disparaît en phase γ; on ne l'observe pas non plus lorsque l'on remplace l'uranium par un métal de structure cubique, le platine par example. Elle est sans doute due au fait que le pouvoir thermo-électrique de l'uranium α doit être anisotrope.

5.2. PLUTONIUM

Pour le plutonium, les données de Waldron et Lee montraient que l'on pouvait espérer une précision raisonnable en adoptant le platine et le platine rhodié comme métaux de référence, surtout en phase δ et en phase ε. En outre une diffusion importante était à craindre en-dessous de 320° avec l'alumel et le chromel; nous ne pouvions d'autant moins l'admettre qu'il nous a fallu opérer sur un fil plus court.

Le fil qui nous a servi d'échantillon provenait d'un lingot de métal de haute pureté que nous avions filé sous la forme d'un fil de 1 mm de diamètre. Ce métal présentait globalement moins de 250 ppm d'impuretés au cours d'un dosage initial.

Nous avons fait en tout quatre cycles de mesures, les deux premiers de 20 à 600° C, le troisième de 20 à 316° de façon à pouvoir faire des mesures de refroidissement en phases γ et β,
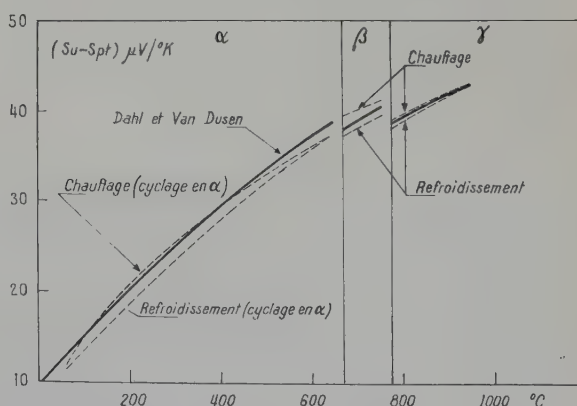

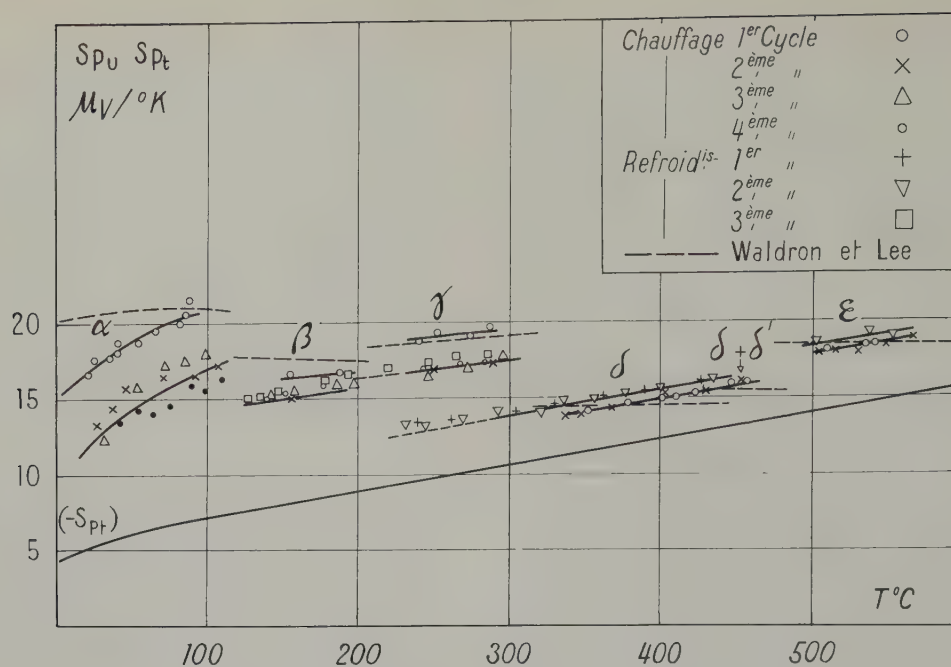Fig. 3. Pouvoir thermo-électrique de l'uranium.

Fig. 4. Pouvoir thermo-électrique du plutonium.

le quatrième à nouveau avec passage en δ. De même que pour l'uranium, nous avons, entre le premier et le deuxième essai, refait les soudures après avoir éliminé à chaque extrémité du fil environ 3 mm de métal.

Les résultats sont reproduits sur la figure 4.

Nous avons trouvé pour toutes les phases, sauf α où le pouvoir thermo-électrique est assez élevé, des pouvoirs thermo-électriques faibles, décroissant faiblement lorsque la température augmente.

Nous pouvons en outre penser raisonnablement que nous commettons sur nos mesures une erreur inférieure à 0,5 ou 1 μV par degré K. En effet, si nous revenons à la formule (2), dans le cas le plus défavorable (plutonium α)

$$\frac{(S_{Pt} - S_{Pu}) + (S_{PtRh} - S_{Pu})}{S_{Pt} - S_{PtRh}}$$

est de l'ordre de 4, $(T_a - T_b)$ de l'ordre de 30 à 40°, η d'environ 10 μV. Cette dernière valeur correspond à l'écart entre nos mesures et celles de Dahl et Van Dusen (figure 2). Elle est de toutes façons d'un ordre de grandeur raisonnable pour un circuit différentiel MFM.

Cette erreur (0,5 à 1 μV/° K) ne doit d'ailleurs varier que faiblement en fonction du temps,

comme le montre la dispersion faible de nos résultats au cours d'un même essai.

Il faut noter que nous avons obtenu des résultats différents entre le premier essai et les suivants en phases α, β, γ qui sont anisotropes. Les mesures sont par contre très reproductibles en phases δ et ε.

Ceci est sans doute à relier à la possibilité d'une texture qui aurait varié au cours des cycles ou peut-être à la diffusion éventuelle du platine qui a donné des effets plus sensibles dans les phases de basse température à structures complexes, propres au plutonium.

Dans l'ensemble, les valeurs, trouvées au premier essai pour chaque phase dans son domaine d'existence sont en bon accord avec celles de Waldron et Lee. Nous avons toutefois observé une loi de variation du pouvoir thermo-électrique en fonction de la température légèrement différente, surtout en phase α.

Notons enfin que nous avons observé au refroidissement, en dessous de 280° C, une légère inflexion de la courbe en phase δ, qui est à relier au changement de pente observé dans les courbes dilatométriques. On attribue ce phénomène à un début de transformation $\delta \rightarrow \gamma$ [6]).

6. Interprétation des résultats pour le plutonium

A température T, supérieure à l'ambiante, et lorsque les électrons de conductibilité sont justiciables de l'approximation des bandes, on sait que le pouvoir thermo-électrique S est lié à la conductibilité électrique σ_0 par la relation [7]):

$$S = -\frac{\pi^2}{3}\frac{k^2 T}{e}\left[\frac{\mathrm{d}\log\sigma_0(E)}{\mathrm{d}E}\right]_{E=E_F} \qquad (3)$$

k étant la constante de Boltzmann, e la charge électronique; et E_F l'énergie au niveau de Fermi.

Les fortes valeurs de la susceptibilité de Pauli du métal montrent qu'il possède une bande étroite à forte densité d'états (E_F) au niveau de Fermi. La conductibilité est limitée alors par les transitions des électrons de conductibilité vers les états vides de cette bande étroite. Dans les métaux de transition usuels, ces transitions seraient dues aux diffusions par les phonons. On aurait, au dessus de l'ambiante [7])

$$\frac{1}{\sigma_0} = f(E)\,T\,n_1(E) \qquad (4)$$

où la fonction f varie lentement avec l'énergie E. D'où:

$$S \simeq \frac{\pi^2}{3}\frac{k^2 T}{e}\frac{\mathrm{d}m_1}{n_1\,\mathrm{d}E_M}. \qquad (5)$$

On sait que contrairement à l'équation (4) la résistivité du plutonium n'est pas du tout proportionnelle à la température absolue T: au dessus de 100° K elle varie peu avec T et cela dans toutes les phases [8]). Ceci suggère que, dans toutes les phases, la diffusion par phonons est faible et qu'une diffusion par des moments atomiques localisés prédomine. Ces moments seraient désorientés au-dessus de 100° K en phase α, ainsi que dans les domaines de stabilité des autres phases. Un comportement analogue de la résistivité est observé dans certains autres métaux (manganèse, métaux des terres rares, etc.[9])). Aux températures bien supérieures à celles où des moments atomiques cessent d'être couplés, la fréquence de choc $1/\tau$ devient indépendante de la température. Elle est proportionnelle à la vitesse des électrons de conductibilité et à $n_1(E)$.

D'où:

$$\frac{1}{\sigma_0} \propto \frac{1}{\tau N_{\text{eff}}} \propto \frac{v(E)\,n_1(E)}{N_{\text{eff}}(E)}. \qquad (6)$$

Le nombre effectif N_{eff} d'électrons de conductibilité et leur vitesse v varient peu avec l'énergie; on retrouve donc une formule très voisine de (5). Pour des électrons libres d'énergie minima E_0 par exemple,

$$N_{\text{eff}}\frac{1}{V} \propto (E-E_0),$$

et on a:

$$S = \frac{\pi^2}{3}\frac{k^2 T}{e}\left(\frac{\mathrm{d}n_1}{n_1\,\mathrm{d}E_M} - \frac{1}{E_M-E_0}\right). \qquad (7)$$

Pour un nombre raisonnable d'électrons de conductibilité par atome, leur énergie (E_n-E_0) sera une fraction appréciable d'unité atomique.

Les équations (5) et (7) sont alors pratiquement équivalentes. Elles donnent pour $\frac{\mathrm{d}n_1}{n_1\,\mathrm{d}E_M}$ les valeurs assez faibles portées au tableau suivant:

T (° K)	325	435	535	635	800
Phase	α	β	γ	δ	ε
$S(\mu V/° K)$	12,5	8,2	9,2	2,6	3,8
$\dfrac{\mathrm{d}n_1}{n_1\,\mathrm{d}E_M}$ (V_A)	40	19	19,5	4,3	5

Ces valeurs sont positives, comme dans l'uranium [10]), mais environ trois fois plus faibles. Elles sont donc probablement trop faibles pour que la théorie de Varley s'applique au Pu.

D'autre part, dans chaque phase, sauf peut-être α, S n'est pas proportionnel à T. Les valeurs de $\frac{\mathrm{d}n_1}{n_1\,\mathrm{d}E_M}$ déduites des opérations précédentes varient donc un peu dans chaque phase avec la température. Cet effet est peut-être lié à une forte courbure de $n_1(E)$ au voisinage du niveau de Fermi. Une telle courbure expliquerait également les faibles variations avec la température observées pour la résistivité et la susceptibilité.

7. Conclusion

Même si l'on tient compte des hypothèses que suggère le comportement électronique anormal du plutonium, les valeurs que nous avons trouvées pour le pouvoir thermo-électrique du plutonium restent trop faibles pour pouvoir, semble-t-il, s'accorder avec la théorie de Varley. Waldron et Lee étaient d'ailleurs parvenus à la même conclusion dans leur communication de Genève.

On se serait de toutes façons attendu à un pouvoir thermo-électrique particulièrement élevé en phase δ. Il semble donc que les raisons véritables du comportement anormal du plutonium δ restent à trouver.

Bibliographie

[1] J. H. O. Varley, Proc. Roy. Soc. **237** (1956) 413

[2] H. B. Waldron and J. Lee, 2ème Conférence de Genève (1958) 15/P/71

[3] G. Borelius, Handbuch der Metallphysik, Band I, Erster Teil (Leipzig, 1935) p. 386

[4] G. Borelius, Handbuch der Metallphysik, Band I, Erster Teil (Leipzig, 1935) p. 398

[5] A. I. Dahl et M. S. van Dusen, J. Res. Nat. Bur. of Standards **39** (1947) 53

[6] R. Pascard, Communication privée

[7] N. F. Mott and H. Jones, Properties of Metals and Alloys (Oxford, Clarendon Press, 1936)

[8] T. A. Sandenaw and R. B. Gibney, J. Phys. Chem. of Solids **6** (1958) 81

[9] P. G. de Gennes et J. Friedel, J. Phys. Chem. of Solids **4** (1957) 71

[10] J. Friedel, J. Phys. Chem. of Solids **1** (1956) 175

THE URANIUM-MOLYBDENUM EQUILIBRIUM DIAGRAM BELOW 900° C

AUSTIN E. DWIGHT

Argonne National Laboratory, Lemont, Illinois, USA

The U-Mo equilibrium diagram has been determined up to 19 wt % Mo and below 900° C. The eutectoid transformation $\beta \rightleftharpoons \alpha + \gamma$ has been located at $639 \pm 5°$ C. The limit of the $\beta + \gamma$ field has been placed at 4.5 wt % Mo at the eutectoid temperature. The γ phase undergoes a eutectoid transformation at 10.5 wt % Mo and $565 \pm 5°$ C, to $\alpha + \delta$. The tetragonal structure of the δ phase was confirmed, with $c_0 = 9.854$ Å, $a_0 = 3.427$ Å, $c/a = 2.876$. It is probable that δ phase is formed by a congruent transformation, rather than by a peritectoid as reported by earlier workers.

Le diagramme d'équilibre U-Mo a été déterminé jusqu'à une teneur en Mo en poids de 19 % et une température inférieure à 900° C. La transformation eutectoïde $\beta \rightleftharpoons (\alpha + \gamma)$ a été située à $639 \pm 5°$ C. La limite du champ $(\beta + \gamma)$ a été situé à 4,5 % en poids de Mo à la température du palier eutectoïde. La phase γ subit une transformation eutectoïde en $(\alpha + \delta)$ pour 10,5 % en poids de Mo et $565° \pm 5°$ C. La structure tétragonale de la phase δ a été confirmée avec les paramètres suivants: $c_0 = 9,854$ Å, $a_0 = 3,427$ Å, $c/a = 2.876$. Il est probable que la phase δ est formée par une transformation congruente plutôt que péritectoïde comme d'autres chercheurs l'ont proposé antérieurement.

Das U-Mo Gleichgewichtsdiagramm wurde bis zu 19 Gew % Mo und bis zu 900° C ermittelt. Die eutektoide Umwandlung $\beta \rightleftharpoons \alpha + \gamma$ liegt demnach bei $639 \pm 5°$ C. Bei der eutektoiden Temperatur reicht das $\beta + \gamma$-Feld bis zu 4,5 Gew % Mo. Die γ-Phase unterliegt bei $565 \pm 5°$ C einer eutektoiden Umwandlung bei 10,5 Gew % Mo in $\alpha + \delta$. Die tetragonale Struktur der δ-Phase konnte bestätigt werden, mit $c_0 = 9,854$ Å, $a_0 = 3,427$ Å und $c/a = 2,876$. Wahrscheinlich wird die δ-Phase kongruent und nicht, wie früher berichtet wurde, durch peritektoide Umwandlung gebildet.

1. Introduction

The U-Mo phase diagram has been the subject of several earlier investigations. Those prior to 1958 were summarized by F. A. Rough and A. A. Bauer [1] and were also reviewed by A. J. Carrea et al.[2]). The diagram of S. T. Konobeevsky et al.[3]) appeared in 1958 and differs in several respects from the earlier work, notably in that the latter authors show the δ (U_2Mo) phase to be formed by a congruent transformation from the γ phase, rather than the peritectoid transformation reported by earlier workers.

2. Experimental Technique

In the present investigation alloy buttons were arc melted, using a tungsten electrode and water cooled copper hearth, from high purity electrolytic uranium described by Blumenthal and Noland [4]) and commercial purity molybdenum. The buttons were in most cases sealed in a zirconium alloy sandwich and hot rolled at 900° C. The resulting slabs were homogenized in the γ range and cut up for X-ray, metallographic and chemical analysis specimens. All alloys were chemically analyzed except a few, which were intended exclusively for use in 2 phase regions. Specimens for X-ray diffraction were small needles, roughly 0.4 cm long and 0.08 cm in diameter. These were wrapped in Mo foil, sealed in evacuated Vycor capsules for heat treatment, and water quenched. Metallographic specimens were processed in the same manner.

All X-ray diffraction work was done at room temperature using Debye–Scherrer cameras. X-

ray needles were cleaned electrolytically in an acetic-perchloric acid bath. Since high precision was necessary to determine the lattice para-meter of the retained gamma phase, the Nelson–Riley extrapolation was applied. Metallographic specimens were etched electro-lytically in a bath of phosphoric acid, ethylene glycol and ethyl alcohol.

3. The Phase Diagram

Fig. 1 shows the graph of lattice parameter in Å vs. composition in at % Mo. A straight line having the equation $a_0 = 3.4808 - 0.00314$ at %

end of the graph, a distinct inflection is apparent corresponding to the $\gamma/(\gamma + Mo)$ phase boundary.

The phase diagram resulting from this investigation is shown in figs. 2 and 3. The points shown represent 73 of the 269 compo-sitions and temperatures investigated. Lines AE and AD were determined by metallographic examination of specimens which were quenched from transformation temperatures above and below the line. This technique, known as the method of temperature brackets, is preferred in the high uranium end of the diagram (up to 6 wt % Mo) because equilibrium is readily
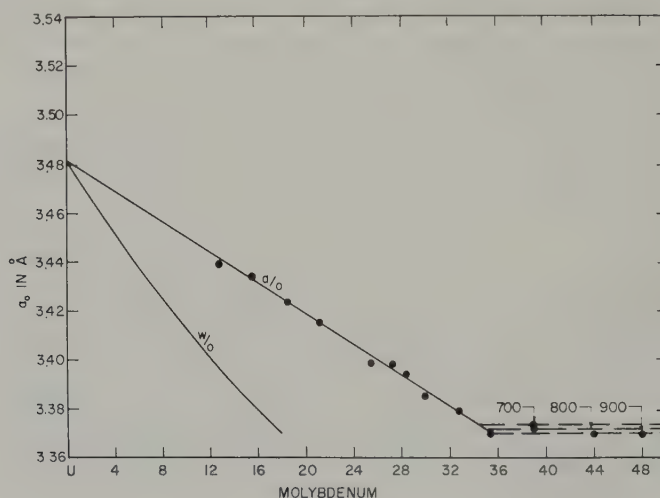

Fig. 1. Lattice parameter curve for U-Mo system, measured at room temperature on specimens quenched from the γ range.

Mo may be fitted to the data points by the method of least squares. The intercept of this line on the ordinate, 3.4808 Å, is the extra-polated room temperature lattice parameter for γ-U, subject to the assumption that the lattice parameter curve remains straight in the high U end where γ cannot be retained for room temperature measurement †. At the high Mo

† The lowest Mo content in fig. 1 is 12.7 at % Mo. A careful examination of the diffraction pattern reveals that the structure of this alloy is retained γ, which is in agreement with the data reported by Ivanov and Badajeva [11]) who retained γ in an alloy of 13 at % Mo, but found a tetragonal phase in a 12 at % Mo alloy. In work at Harwell, Hills et al.[12]) inferred by metallographic examination that a tetra-

attained in times ranging up to 4 days, and because a small amount of β in γ or γ in β is easily detected. Extrapolation of line AE back to pure U gives the value 775° C for the β to γ transformation in close agreement with the value 774.8 ± 1.6° C reported by Blumenthal [5]). Figs. 4a and 4b show the microstructure of a 3 wt % Mo alloy quenched from 665° C in the $\beta + \gamma$ field to consist of β particles distributed in

gonal phase is formed by quenching a 15 at % Mo alloy. In the present investigation, as well as in the work by Ivanov and Badajeva, it is indicated that a b.c. cubic γ is retained in the 15 at % Mo alloy. This apparent discrepancy may be due to a difference in quenching rate.
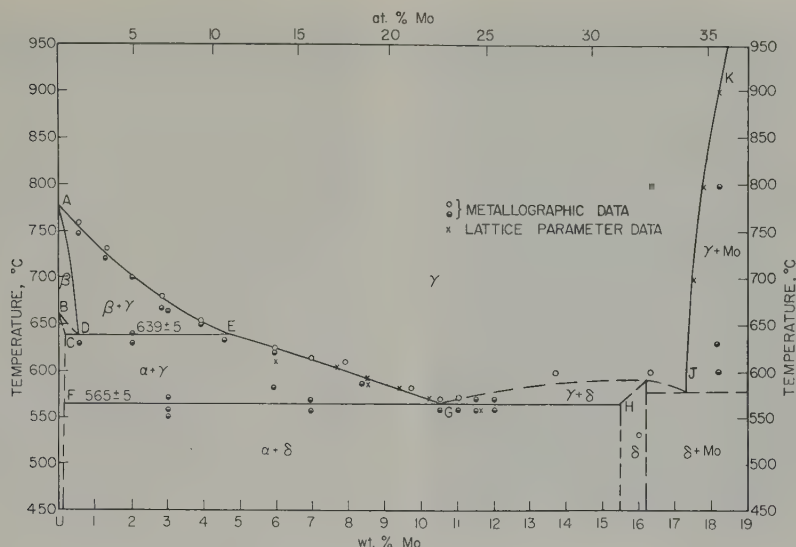
Fig. 2.   U-Mo equilibrium diagram to 19 wt % Mo.

an α' matrix (γ matrix at 665° C). The β particles characteristically form along the γ grain boundaries. The α' phase, also called martensitic α and strained α, appears in at least eight uranium-base systems. It forms on quenching from the gamma phase when there is sufficient solute to suppress the normal $\gamma \rightarrow \beta \rightarrow \alpha$ sequence but insufficient solute to permit retention of metastable γ to room temperature. In the present investigation, the lower limit of Mo content necessary for martensitic α formation is placed at 2 wt %. A 2 wt % Mo specimen quenched from 696° C exhibited a mixture of martensitic α and the Widman-

statten α which is obtained at lower Mo contents. The maximum Mo content permissible for martensitic α formation lies between 4.5 and 5.5 wt %. The formation of the α' phase has been studied by Harding and Waldron [6]).

The eutectoid horizontal CDE was located at $639 \pm 5°$ on the basis of both metallographic and X-ray diffraction data. X-ray diffraction needle specimens and metallographic specimens were capsulated together, given a 1 hour soak in the gamma range, then transferred quickly to a furnace set at a predetermined temperature. As a typical example, specimens of U + 1.33 wt % Mo alloy were held for 3 days at 645° C, water quenched, and examined as soon as possible after quenching. The diffraction film exhibited the pattern characteristic of β uranium, and the microstructure showed γ particles in a β matrix, fig. 5. Successively lower temperatures were used until specimens quenched from 633° C exhibited only an α diffraction pattern. To guard against the possibility of error due to supercooling of β, a refinement of the bracketing method was used. Specimens of a 0.56 wt % Mo alloy were heat treated at 625° C to produce an $\alpha + \gamma$ structure, shown in fig. 6a. Other specimens were heat treated at 645° C to produce a β or $\beta + \gamma$ structure, shown in fig. 6b. Pairs of specimens were then capsulated
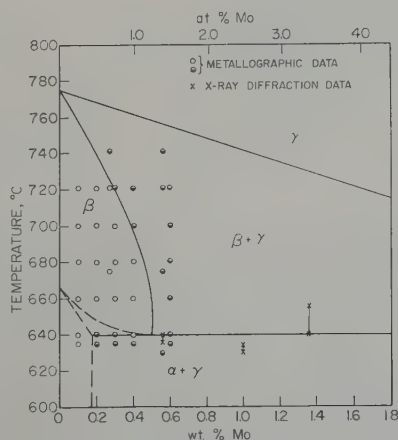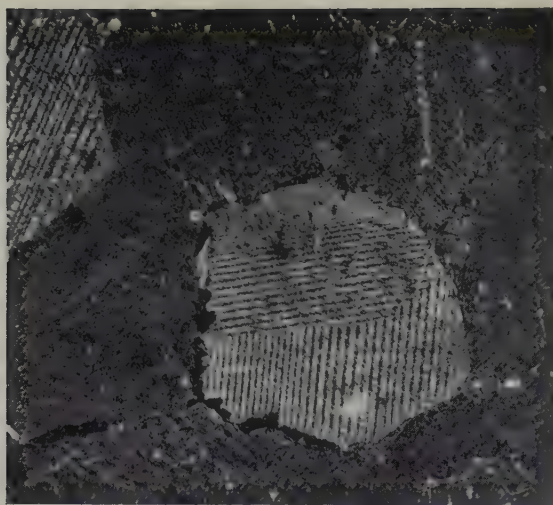

Fig. 3.   U-Mo equilibrium diagram to 1.8 wt % Mo.

Fig. 4a. Retained β network around Martensitic α, in U + 3 wt % Mo alloy after quenching from 665° C. At 665° C structure was $\beta + \gamma$. Polarised light. Etchant: phosphoric acid. 200 ×.
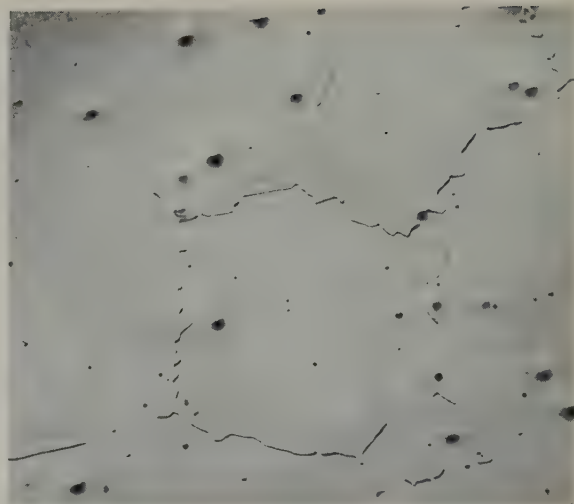
Fig. 4b. Retained β network around Martensitic α, as above but bright field illumination. Etchant: phosphoric acid. 200 ×.
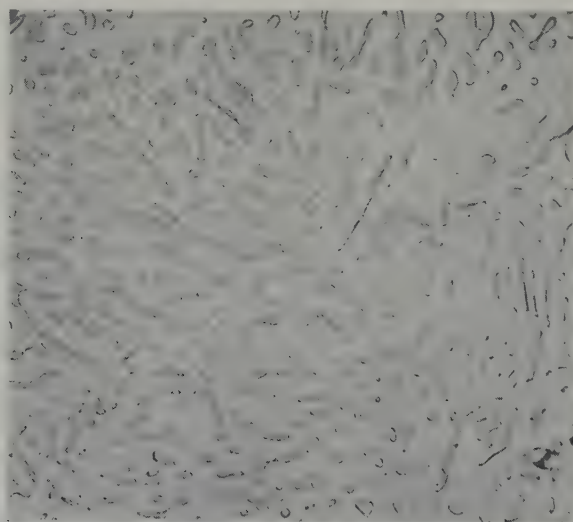

Fig. 5. α' (formerly γ) particles in β matrix after quenching a 1.33 wt % Mo + U alloy from 645° C. Bright field. Etchant: phosphoric acid. 400 ×.

together for heat treatment at 635 and 645° C. It was found that a prior $\alpha + \gamma$ structure transformed to β at 645° C and a prior β structure transformed to $\alpha + \gamma$ at 635° C. The equilibrium transformation temperature was thereby bracketed between these two temperatures. An evaluation of all the pertinent data showed 639° C to be the most probable temperature.

The $\gamma/(\gamma + \alpha)$ line, EG in fig. 2, was studied intensively. Up to 6 wt % Mo, the line can be readily determined by the method of temperature brackets. For example, an alloy containing 5.93 wt % Mo with a prior $\alpha + \gamma$ structure transformed to γ at 625° C, but the same alloy previously quenched from the γ range transformed to an $\alpha + \gamma$ structure at 621° C. For Mo

Fig. 6a. γ particles in α matrix after quenching a U + 0.56 wt % Mo alloy from 625° C. Bright field. Etchant: phosphoric acid. 400 ×.
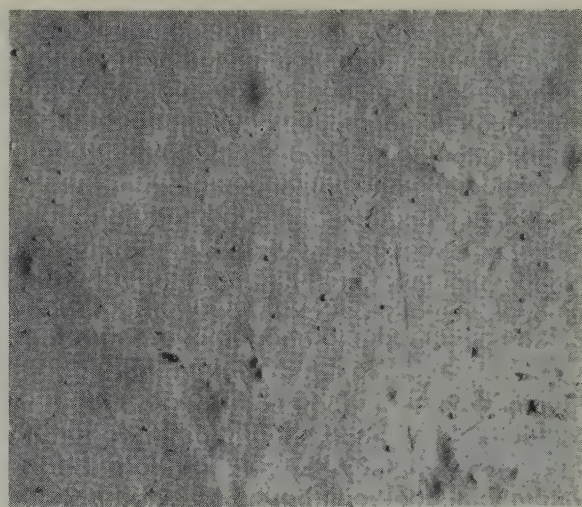

Fig. 6b. Retained β structure after quenching a U + 0.56 wt % Mo alloy from 645° C. Bright field. Etchant: phosphoric acid. 400 ×.

contents higher than 6 wt % the transformation times necessary to reach equilibrium became excessively long, and the method of lattice parameters was used instead. In the latter method, X-ray needles and metallographic controls were transformed in the α + γ region. The lattice parameters of the γ phase were measured as accurately as possible, and from fig. 1 was obtained the corresponding composition of the γ phase. One advantage of this method over that of temperature brackets is that of saving time. A 10 wt % Mo alloy for example would require at least two months at 570° C to obtain metallographic evidence of transformation, but a 6 wt % Mo X-ray specimen can be transformed to α + γ at 570° C in less than two weeks. Further, the lattice parameter of the γ in the α + γ alloy gives a derived composition directly on the γ/(α + γ) line rather than a point lying above or below the line.

An interesting feature of the α + γ field is the occurrence within it of a lamellar α + γ structure formed by rejection of α from a supersaturated γ solid solution when the rejection occurs at a temperature that is approximately 15° C or more below the solvus line. An example is shown in fig. 7, shown by X-ray diffraction to be an α + γ structure. The dark lamellae were identified

as α by the observation that they darken on standing in air; the white matrix is unaffected at room temperature. The range of the lamellar structure is from 5 to 8 wt % Mo, and 571° C to 605° C. Strangely, the lamellar structure is not found when the rejection of α occurs immediately below the (α + γ)/γ line; here the structure consists of spherical α particles in a γ matrix. It is believed that the lamellar α + γ
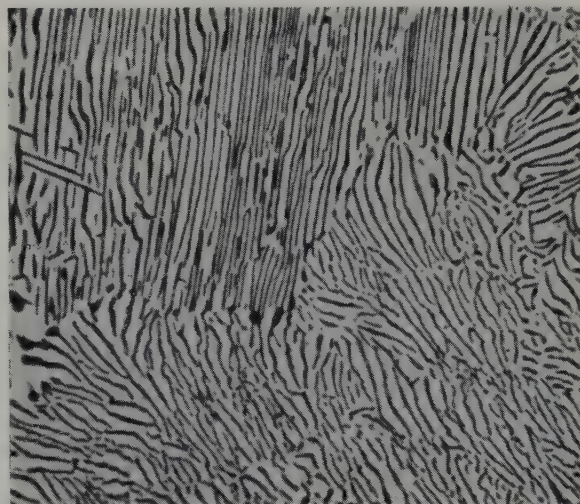

Fig. 7. α lamellae in γ matrix after quenching a U + 5.92 wt % Mo alloy from 581° C. Bright field. Etchant: phosphoric acid. 1600 ×.

structure may have misled earlier workers into reporting a eutectoid in the range 5 to 8 wt % Mo. Therefore, the fact that proeutectoid α is rejected from solution below a sloping line (EG) is emphasized. On the other hand, the lamellar structure shown in fig. 6a was formed by the eutectoid transformation of $\beta \rightarrow \alpha + \gamma$. Of the two lamellar structures observed to form in the $\alpha + \gamma$ field, the one resulting from eutectoid decomposition of β consists of γ lamellae in a matrix of α, whereas the α lamellae precipitated from supersaturated γ occur in a matrix of residual γ.

The lower boundary of the $\alpha + \gamma$ field is the line FGH, at the eutectoid temperature. An attempt was made to determine the temperature of line FGH directly by heat treating X-ray needles of a 12 wt % Mo alloy (selected because it lay close to the probable eutectoid composition) at 555, 560 and 564° C for 1 month. The resulting patterns exhibited a mixture of γ and δ lines, indicating incomplete transformation. A more successful technique involved the use of a 3 wt % Mo alloy to allow rapid transformation. A finely dispersed $\alpha + \delta$ structure was first created and then this structure was reheated to successively higher temperatures until the δ changed to γ. In this method, X-ray needles were transformed to $\alpha + \delta$ at 500° C. which is near the nose of the TTT curve [7]), thus permitting rapid transformation. Diffraction patterns were taken to confirm the presence of δ. Due to the relatively low Mo content of 3 wt %, a strong α and weak δ pattern was obtained. The success of this method depends upon the fact that several strong lines of the δ diffraction pattern lie in a gap where there are no lines of the α pattern, making identification of a small amount of δ quite certain. Reheating the needles to 555°, 560°, 565° and 570° C for 3 weeks caused the disappearance of the δ lines in the 570° C sample, but not in the other three. Therefore, the line FGH is located at $565 \pm 5°$ C.

The crystal structure of the δ phase was found to be tetragonal, of the $MoSi_2$ type, as first reported by Halteman [8]). In the present

investigation, a needle shaped specimen containing 16 wt % Mo was heat treated at 536° C and a diffraction pattern taken with Cu radiation. The parameters are $c_0 = 9.854 \pm 0.001$, $a_0 = 3.427 \pm 0.0010$, $c/a = 2.876$. The microstructure of the δ phase is shown in fig. 8. No attempt was made to locate precisely the limits of the δ phase, but the apparent single phase present in the 16 wt % alloy is in agreement with the data of Halteman. The data of Konobeevsky et al.[3]) indicate a range of 16.5 to 17 wt % Mo for the δ phase.

The $\gamma/(\gamma + Mo)$ line was investigated by both metallography and X-ray diffraction from 600° C to 900° C. The metallographic results, all of which are shown in fig. 2, bracket the line between rather wide limits at 600, 700 and 800° C. In theory the line can be located by means of fig. 1 at 700, 800 and 900° C by the intersections of the three iso-parametric lines of the $\gamma + Mo$ alloys with the sloping line of the single phase γ alloys. However, the small variation of a_0 over this temperature range, the relatively small amount of X-ray data in the two-phase region and the limited precision of the data of fig. 1 all combine to limit the accuracy with which the phase boundary can be determined in this way. A rather detailed analysis of the data indicates that at the three
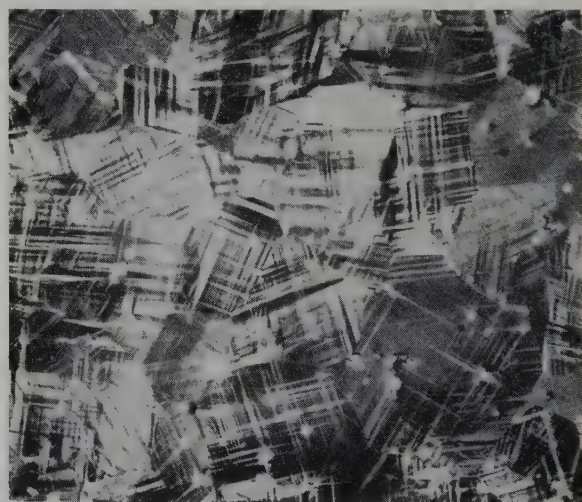

Fig. 8. δ phase formed at 532° C in alloy of U + 16 wt % Mo. Polarised light. Etchant: acetic-chromic. 400 ×.

pertinent temperatures the $\gamma/(\gamma+\text{Mo})$ line lies between the following limits:

$$700° \text{ C}: 16.6\text{--}18.2 \text{ wt } \% \text{ Mo}$$
$$800° \text{ C}: 16.7\text{--}18.3 \text{ wt } \% \text{ Mo}$$
$$900° \text{ C}: 17.3\text{--}18.9 \text{ wt } \% \text{ Mo}.$$

The X-ray data points on fig. 2 are the mean values and the boundary has been drawn through these.

The location of the $\gamma/(\gamma+\text{Mo})$ line was also confirmed by the method of vanishing lines. As an example, a pattern taken of an alloy of U + 18.19 wt % Mo heat treated at 800° C showed a faint (110) line of the Mo pattern, but an alloy of U + 16.32 wt % Mo showed no trace of a Mo pattern.

The eutectoid horizontal passing through point J of fig. 2 is purely speculative, as is the peak of the δ phase. It is believed that the $\gamma/(\gamma+\text{Mo})$ line is known with sufficient accuracy to require a eutectoid at J although no data are available.

4. Discussion

There is general agreement that the lattice parameter of γ-U is contracted by Mo additions, but there is some variation among the results of different investigators. Wilson and Rundle [9] presented data for five alloys. Their data have been extrapolated to a value of 3.474 Å for γ-U at room temperature. Pfeil [10] has reported parameter data on two alloys, and these data lie fairly close to the line determined in the present investigation. Konobeevsky et al.[3] have reported the equation 3.481–0.00333 wt % Mo = a_0, but did not report the number of points on which this equation was based, or the purity of the uranium. The present investigation is believed to give the most reliable lattice parameter data as it is based upon ten alloys made from high purity electrolytic uranium.

The U-Mo diagram in figs. 2 and 3 differs from those of earlier workers principally in the lower temperature for the $\beta \to \alpha+\gamma$ eutectoid (639° C) and in the open maximum formation of δ rather than the peritectoid transformation. The major difference between the diagram of Konobeevsky et al.[3] and the present work is that the former authors place the maximum Mo content of the $\beta+\gamma$ field at 6 at % Mo and 635° C compared with 11 at % Mo and 639° C in the present work.

Acknowledgements

References

1) F. A. Rough and A. A. Bauer, Constitution of Uranium and Thorium Alloys, Battelle Memorial Institute (USA) Report, BMI-1300 (1958)
2) A. J. Carrea, D. R. F. West and J. G. Ball, J. Nuclear Eng. 7 (1958) 189
3) S. T. Konobeevsky et al., Proceedings of the Second Geneva Conference (1958) 6, 194
4) B. Blumenthal and R. A. Noland, Progress in Nuclear Energy, 1, Series V (1956)
5) B. Blumenthal, private communication
6) A. G. Harding and M. B. Waldron, AERE Harwell (UK) Report, M/R 2673 (1958)
7) R. J. Van Thyne and D. J. McPherson, Trans. Amer. Soc. Metals 49 (1957) 598
8) E. K. Halteman, Acta Cryst. 10 (1957) 166
9) A. S. Wilson and R. E. Rundle, Acta Cryst. 2 (1949) 126
10) P. C. L. Pfeil, J. Inst. Metals 77 (1950) 553
11) O. S. Ivanov and T. A. Badajeva, Proceedings of the Second Geneva Conference (1958) 6 139
12) R. F. Hills, D. R. Harries, D. J. Hodkin and M. B. Waldron, AERE Harwell (UK) Report, M/R 2840

LETTERS TO THE EDITORS – LETTRES AUX EDITEURS

THE NATURE OF SUBGRAIN BOUNDARIES DUE TO PHASE TRANSFORMATION IN URANIUM

R. W. CAHN and Mrs. H. TOMLINSON

Department of Physical Metallurgy, University of Birmingham, Birmingham 15, UK

When β-uranium is transformed into the α-phase on cooling, each grain is broken up into numerous subgrains, each slightly disoriented from its neighbours [1-3]. It has been suggested [1] that these subgrains are formed because of the large volume change accompanying the transformation. It was proposed that the α phase, which is softer than the β phase at the transformation temperature, suffers distortion during the transformation; this distortion is a form of creep which, at the high temperature concerned results in the formation of "creep cells" such as are formed in aluminium during creep. This process may also be regarded as a strain-induced polygonization. The faster the rate of cooling through the transformation temperature, the faster is the effective rate of creep of the α grains, and the smaller should be the mean size of creep cells. This is in fact observed.

As a test of the proposed mechanism, the orientation relationship between neighbouring pairs of subgrains has been determined. If subgrains are indeed formed by the thermally activated rearrangement of glissile dislocations, as in creep, then the sub-boundaries will normally consist of arrays of well-defined types of dislocations; if the active slip systems are known, the nature of the expected misorientations across the subboundaries can then be computed and compared with experiment. Creep cells in zinc have been examined experimentally in this way [4], and a detailed interpretation of the results obtained was given by Ball and Hirsch [5]) and by Ball [6]).

In the case of α-uranium, the slip systems active at high temperature have only recently been determined [7]). At 600° C, the system predominating at room temperature, (010) [100], still persists but a new system with a much lower critical stress has appeared: (001) [100]. (At room temperature this only acts as a cross-slip system.) The (110) [1$\bar{1}$0] system also operates at 600° C, but with a higher critical stress than either of the others. A fourth system, (021) [1$\bar{1}$2], has such a high critical stress that for present purposes it can safely be ignored.

If a sub-boundary were to consist entirely of edge dislocations of the (010) [100] system, it would be a simple tilt boundary and the *rotation axis* (i.e. the axis about which the lattice of one subgrain must be rotated to bring it into congruence with the lattice of its neighbour) will be normal to the slip direction and parallel to the slip plane, i.e. the axis will be [001]. Similarly, a tilt boundary consisting of (001) [100] edge dislocations would have a [010] tilt axis. A tilt boundary consisting of (110) [1$\bar{1}$0] edge dislocations would, again, have [001] as rotation axis.

An actual subgrain boundary formed in the way suggested above would normally contain a mixture of two different kinds of dislocations. The crystallography of this situation is discussed by Ball and Hirsch [5]). The combination: (010) [100] + (001) [100] corresponds to their

case 3; here *the axis of rotation may take up any position in the plane normal to the common Burgers vector, i.e any position lying in the (100) plane*. The combinations (010) [100]+ (110) [1$\bar{1}$0], or (001) [100]+(110) [1$\bar{1}$0], both correspond to Ball and Hirsch's case 4, and here the rotation axis must be normal to both the Burgers vectors; i.e. it must be parallel to [001].

It follows that, if the present hypothesis as to the origin of subgrains in α-uranium is correct, all observed rotation axes relating to orientations of neighbouring pairs of subgrains should either coincide with [001] or else lie in the (100) plane (in other words, in the zone defined by [001] and [010]). The theoretical treatment also predicts the relationship of the rotation axis to the plane of the sub-boundary itself; however, this aspect was not examined in the present experiments.

Three uranium rods were passed slowly through a fairly steep temperature gradient so that they transformed progressively from the β into the α phase. Under these conditions [1] very large α grains, each decomposed into large subgrains, are formed. Several pairs of adjacent subgrains were examined in each specimen; some of the sub-boundaries concerned were longitudinal, some inclined to the direction of the thermal gradient. In each case, a Laue photograph was made of the two subgrains together, by causing the X-ray beam to straddle the boundary. A specially-designed micro-beam camera [8] was used which allowed precise positioning of the beam.

12 patterns were clear enough to interpret. In each case, the mean orientation of the α grain was determined from the Laue pattern, and the rotation axis was then determined from the relative positions of the various associated pairs of Laue spots, by an analytical method previously described [4]. The results are shown in fig. 1, normalised into a quadrant of the standard stereographic protection of α uranium. Each circle represents the estimated experimental error in determining the corresponding rotation axis (the error depends primarily on
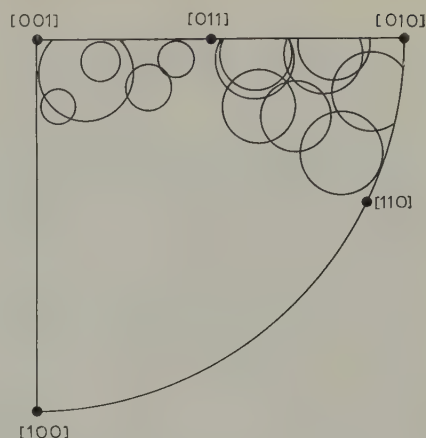

Fig. 1. Observed rotation axes for 12 pairs of subgrains in α-uranium samples, after $\beta \rightarrow \alpha$ transformation.

the magnitude of the misorientation of the subgrain pairs). Although some of the axes deviate slightly from the predicted [001]–[010] zone, all are close to it, and within the margin of error half of the axes actually lie in the expected zone.

The results of these experiments, therefore, confirm the hypothesis that subgrains in $\beta \rightarrow \alpha$ transformed uranium are due to a strain-induced form of polygonization of glissile dislocations in the α-uranium lattice. A corollary of this mechanism is that the subgrain configuration can be modified by applying an external stress during transformation; it is hoped to investigate this experimentally.

References

[1] R. W. Cahn, Acta Metallurgica **1** (1963) 176
[2] P. Lehr, Comptes Rendus **241** (1955) 1043
[3] P. Lehr, Saclay (France) rapport CEA (1958)
[4] R. W. Cahn, I. J. Bear and R. L. Bell, J. Inst. Metals **82** (1954) 481
[5] C. J. Ball and P. B. Hirsch, Phil. Mag. [vii] **46** (1955) 1343
[6] C. J. Ball, Phil. Mag. [viii] **2** (1957) 977
[7] H. H. Chiswick, A. E. Dwight, L. T. Lloyd, M. V. Nevitt and S. T. Zegler, Second Geneva Conference (1958) 15/P/713
[8] H. M. Otte and R. W. Cahn, J. Sci. Instr. **36** (1959) 463

CHANGEMENT DE PHASE ET MISE EN DESORDRE PAR IRRADIATION DU COMPOSE U₂Mo

Mme J. BLOCH

Centre d'Etudes Nucléaires de Saclay, Gif-sur-Yvette (S & O), France

Nous avons étudié des plaquettes d'un alliage uranium-molybdène ayant la composition de U_2Mo. Après homogénéisation à 1050° C, l'alliage a subi un traitement de recuit de sept jours à 500° C afin d'obtenir la phase γ' quadratique ordonnée.

Les échantillons ont été irradiés dans un flux de neutrons thermiques variant de 2×10^{10} à 2×10^{12} n/cm²/sec et à une température inférieure à 65° C. Des moniteurs d'Al-Co ont servi à mesurer les flux intégrés reçus par chaque échantillon; la gamme étudiée s'étend de 10^{16} à $1,2 \times 10^{18}$ n/cm². Nous avons fait sur chaque échantillon, avant et après irradiation, un diagramme de diffraction de rayons X sur un diffractomètre à compteur [1]).

Nous avons porté notre attention sur la disparition des raies d'ordre et sur le passage de la structure quadratique de la phase γ' à la structure cubique de la phase γ. Cette phase est stable à haute température. La disparition par irradiation de cette phase γ' a déjà été constatée par Bleiberg d'une part [2]) et par Konobeevski d'autre part [3]) sur des alliages U-Mo présentant la structure $\alpha + \gamma'$.

1. DISPARITION DES RAIES D'ORDRE

Nous avons pour chaque échantillon évalué le degré d'ordre d'après le rapport I'/I des intensités de la raie de surstructure (101) après et avant irradiation.

D'après ces résultats préliminaires nous avons tracé la courbe donnant I'/I en fonction du flux total ϕt, ce qui indique la vitesse de mise en désordre du composé considéré. (courbe 1)
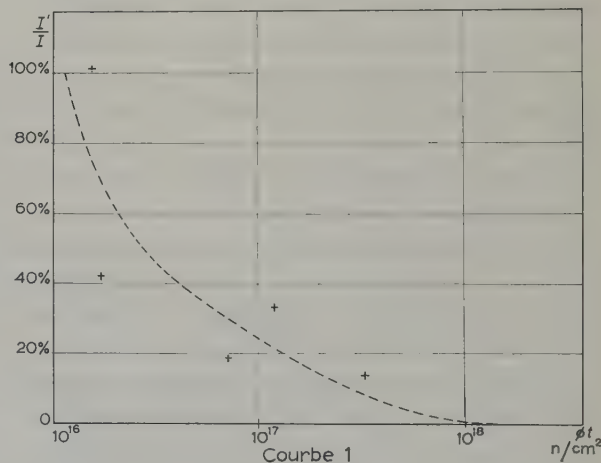
Courbe 1

2. CHANGEMENT DE PHASE

Nous avons étudié chaque échantillon sous des angles de Bragg variant de 10 à 75°. A partir de ces diagrammes nous avons calculé la meilleure valeur des paramètres pour chaque échantillon irradié et tracé les courbes des paramètres en fonction du flux total (courbes 2: nous avons porté en abscisses a' et $\frac{1}{3}c'$ car dans la maille quadratique de γ' la valeur de c est voisine de $3a$).

Nous avons constaté une évolution des paramètres de la phase quadratique vers une valeur qui est celle du paramètre de la phase

cubique, traduisant donc un passage *continu* de la structure quadratique à la structure cubique.
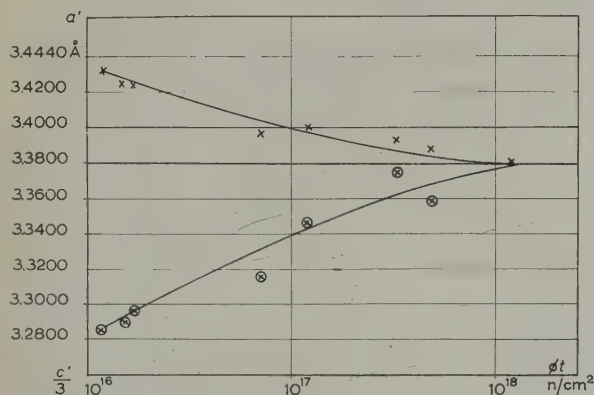
Courbes 2

TABLEAU 1

Flux total en neutrons/ cm²	Ordre I'/I en %	a' (Å)	c' (Å)	$\frac{1}{3}c'$ (Å)	$a' - \frac{1}{3}c'$ (Å)
$1,26 \times 10^{16}$		3.4322	9,8592	3,2864	0,1458
$1,5 \times 10^{16}$	100	3,4239	9,8747	3,2916	0,1323
$1,71 \times 10^{16}$	42	3,4238	9,8930	3,2976	0,1262
$7,1 \times 10^{16}$	17,6	3,3970	9,9621	3,3173	0,0797
$1,22 \times 10^{17}$	33	3,4045	10,0345	3,3448	0,0597
$3,3 \times 10^{17}$	14	3,3930	10,1259	3,3753	0,0177
$4,8 \times 10^{17}$		3,3890	10,0770	3,3590	0,0300
$1,2 \times 10^{18}$	0	3,3798			0

Wittels a constaté un phénomène analogue dans des composés du type $BaTiO_3$ [4]).

Il n'y a, à aucun moment, coexistence des raies quadratiques et des raies cubiques comme on aurait pu s'y attendre si l'on pensait à un mécanisme de transformation qui soit celui d'une pointe de fission où une petite région est chauffée au-dessus de la température de transition et trempée. C'est par exemple ce qui a été observé par Wittels [5]) pour de la zircone contenant un peu d'uranium.

La transformation, débutant à des flux aussi faibles que 10^{16} n/cm² est achevée pour un flux voisin de $1,2 \times 10^{18}$ n/cm².

Bibliographie

[1] J. Bloch, Appareil de radiocristallographie pour examen de matériaux irradiés, Rapport C.E.A., Saclay, France, à paraître

[2] M. L. Bleiberg, L. J. Jones et B. Lustman, J. Appl. Physics **27** (1956) 1270

[3] S. T. Konobeewski et N. F. Pradviouk, J. Nucl. Energy II **9** (1959) 75

[4] M. C. Wittels et F. A. Sherril, J. Appl. Physics **28** (1957) 606

[5] M. C. Wittels et F. A. Sherril, J. Appl. Physics **27** (1956) 643

THE SINTERING OF URANIUM OXIDES †

(DISCUSSION OF PAPER BY BEL, DELMAS AND FRANCOIS: FRITTAGE DE L'OXYDE D'URANIUM DANS L'HYDROGENE A 1350° C)

J. WILLIAMS

UKAEA, *Atomic Energy Research Establishment, Harwell, Didcot, Berkshire, UK*

In their recent paper "The sintering of uranium dioxide in hydrogen at 1350° C" M. Bel and his co-authors [1]) raise a number of points which call for comment.

The French investigators failed to detect any beneficial effect of departure from stoichiometry upon sintering behaviour in neutral atmospheres, in contradiction to our findings [2]). In our studies we used no additions of binder or lubricant, and the pressed pellets were sintered on alumina trays; M. Bel *et al.* added 3 % camphor and 0.5 % stearine and probably sintered on molybdenum trays, although this latter point is not clear from the text.

Our experience using a wide variety of organic binders with non-stoichiometric powders is that unless the binders are removed carefully, preferably in an oxidising atmosphere, the non-stoichiometric powders can be reduced to the stoichiometric condition before appreciable sintering has occurred. In the absence of further data on the oxygen content of the pellets sintered in argon by French investigators it cannot be said therefore that they were truly studying the sintering behaviour of non-stoichiometric oxides. A second factor which would also affect their results would be the use of molybdenum trays. We found that non-stoichiometric oxide in contact with molybdenum sintered less readily than the same material

TABLE 1

Powder characteristics			Green density (g/cm³)	Sintering conditions					Final density (g/cm³)	Porosity decrease (%)	Density increase (%)
Origin	Surface area (m²/g)	O/U ratio		Heating rate °C/h	Time at temp. (h)	Sintering temp. (°C)	Atmosphere	Dew points (°C)			
French H	16	—	5.5	75	5	1400	Cracked ammonia	—78*(?)	10.4	92.9	89.1
French J	4.5	—	6.3						10.25	91.3	63.1
British	6	2.18	4.6	300	2	1410	Hydrogen	—78 to —96	9.65	90.6	110
	2	2.08	5.4					—96	9.07	80.0	68
	6	2.24	4.6					—96	8.24	76.4	78.7
	16	2.67	5.0					—96	10.4	95.9	108

Dewpoint of —96° C ≡ 2 × 10⁻⁵ mg/l; —78° C ≡ 5 × 10⁻⁴ mg/l
* Assumed from the text to have been dried with magnesium perchlorate.

† *Editors' note:* Dr. DELMAS' reply to this letter will be published in this journal, Vol. 2, no. 2.

in contact with alumina. On the basis of the data reported, there is no evidence that an insensitivity of sintering behaviour towards oxygen content has been established.

The second feature on which I wish to comment relates to the sintering of "active" uranium oxide powders in hydrogen. In the table 1 are assembled data selected from both the French and our own work. Comparison of the sintering behaviour of the various powders is complicated by their differing compacting behaviour and it is necessary to use some parameter which takes into account the variation in green density. A reasonable, although not ideal parameter is the percentage decrease in porosity. Ignoring the difference in sintering cycles which reflect to the advantage of the French powders it will be seen that these powders, and the one British powder sintered in what we termed "incompletely dried hydrogen" showed approximately the same percentage decrease in porosity. Thus there seems to be no great difference between the two sets of results when rationalized. However when comparable British powders were sintered in "dry hydrogen", i.e. using phosphorus pentoxide as a dessicant, their sintering behaviour deteriorated. This apparently large effect of a small variation in moisture content of the hydrogen upon sintering behaviour was emphasized in our original paper and is worthy of further investigation. Judged on the basis of percentage decrease in porosity, the powder which sintered best in hydrogen was the British U_3O_8 which had the highest surface area and oxygen content of the powders examined.

The third feature concerns the existence of the "over-sintering" phenomenon, i.e. the deterioration of density with increase of sintering temperature above some optimum value. To the best of my knowledge, this phenomenon was first reported for uranium oxide by Murray and Thackray in 1950[3]) and has been shown by ourselves and other investigators to be a common occurrence when sintering other "active" powders. An explanation of these effects could lie in the interaction of grain growth and sintering, but explanations in terms of grosser mechanisms such as bloating due to entrainment of gases in closed pores should not be lost sight of; dilatometric studies of the sintering process using heating rate as a variable would help to eliminate some of the possible explanations of the "over-sintering" of uranium oxides.

References

[1]) A. Bel, R. Delmas and B. Francois, J. Nucl. Mat. 1 (1959) 259

[2]) J. Williams, E. Barnes, R. Scott and A. Hall, J. Nucl. Mat. 1 (1959) 28

[3]) P. Murray and R. W. Thackray, AERE, Harwell (UK) Report M/R 614 (1959)

BOOK REVIEWS

F. A. Rough et A. A. Bauer, *Constitution of Uranium and Thorium alloys* (Addison–Wesley, 1958. 153 p.)

Ce livre représente la 2ème édition d'un document (BMI 1000) déjà bien connu dans les laboratoires de métallurgie nucléaire. Il faut lui souhaiter une diffusion encore plus grande car il rassemble des renseignements plus récents, plus complets et la présentation a été améliorée.

Les systèmes sont présentés dans l'ordre alphabétique (en langue anglaise) des éléments d'addition; il n'y a plus de classement à part des systèmes dont le diagramme d'équilibre n'a pas été établi et la consultation de l'ouvrage s'en trouve facilitée.

Tous les diagrammes comportent les deux échelles de concentration: atomes % et poids %, ce qui est particulièrement utile pour les alliages à base d'uranium et de thorium. Un bref exposé résume les données existantes sur la constitution des alliages et les structures cristallines des composés formés. Comme beaucoup de références sont classifiées ou non publiées, ce livre constitue une source unique d'informations, très précieuse pour les chercheurs extérieurs à l'AEC ou à l'UKAEA.

Un tel ouvrage n'est jamais complet. Le grand intérêt qu'il présente pour les diagrammes d'équilibre et les données cristallographiques fait regretter qu'il n'y ait pas un mot ni une référence sur les mécanismes et cinétiques de transformation, ni sur les principales propriétés des alliages.

On peut regretter aussi que certaines références françaises ou anglaises aient été omises, et qu'en général un plus grand poids soit accordé aux publications de source américaine; c'est le cas, par exemple, du système U-Zr pour lequel Rough et Bauer reproduisent le diagramme du Battelle Memorial Institute, alors qu'une toute récente étude d'Argonne vient de confirmer le diagramme différent de Summers-Smith (Aldermaston-G.B.).

La petite échelle des figures empêche souvent de distinguer la position des limites de solubilité; mais peut-être un agrandissement eut-il donné une idée fausse de la précision des mesures. Et cela se rattache à notre dernière observation:

On trouvera sur ces diagrammes beaucoup de lignes en pointillé, mais peut-être n'y en a-t-il pas encore assez. En effet, même lorsqu'un système a été étudié par plusieurs auteurs, il arrive fréquemment que chacun de ceux-ci se soit attaché plus spécialement à un domaine particulier de température ou de composition et qu'ils aient tous reporté une ligne, un liquidus par exemple, tracé par un des premiers expérimentateurs utilisant des métaux de base de pureté insuffisante ou des techniques d'élaboration n'excluant pas toute contamination des alliages. Ainsi dans un diagramme, fruit de nombreuses études, il peut se trouver encore des lignes douteuses.

C'est pourquoi, tout en insistant sur le grand intérêt de ce document, nous recommandons de l'utiliser seulement comme un catalogue pour une comparaison grossière, ou comme un recueil de constantes de provenances connues. Mais pour tout travail de détail il est indispensable de se reporter aux articles originaux cités par Rough et Bauer, pour connaître les analyses des matériaux utilisés, les modes opératoires, la précision des résultats, etc. . . . Pour mieux démontrer cette nécessité, il suffit de signaler qu'en reportant sur un même graphique toutes les données publiées concernant un diagramme très étudié comme U-Mo ou U-Nb, on obtient un faisceau de lignes qui révèle une incertitude atteignant souvent 3 at % ou 20° C, si on donne la même valeur à tous les résultats.

G. CABANE

J. A. Lane, H. G. MacPherson and F. Maslan (editors), *Fluid Fuel Reactors*. (Addison-Wesley Publishing Company, Reading, Pennsylvania, and London, 1958. 1008 pages. $ 11.50, 87s.).

This is the largest (1008 pages) of the Geneva Presentation Volumes commissioned by the USAEC for the 1958 Atoms for Peace Conference. One may, at first sight, be puzzled by the fact that this volume is larger than that on Solid Fuel Reactors (864 pages) of which there has been much more operational experience. The clue lies in the foreword by Dr. Alvin Weinberg in which he discusses the two approaches to reactor technology—the mechanical engineering approach with simplicity of design as its keynote and the chemical approach which leads to the concept of a reactor as a type of chemical plant utilizing a fissile solution as its working fluid. It is unfortunate that this comparison is not developed further in this book in view of the uncertainty in recent years of the value of pressing forward with the development of fluid fuel systems. This uncertainty is bound up with the reason

for the size of this volume, i.e. the very difficult problems arising from the design of plant for the generation and utilization of fission heat using a highly radioactive and corrosive fluid. The solution of these problems has involved a vast amount of research and development effort; this book provides a lucid and authoritative account of the results of this work.

The concept of fluid fuel reactors dates back to the early days of atomic energy when Halban and Kowarski in 1940 performed experiments on suspensions of U_3O_8 in heavy water and also are reported to have suggested the use of a uranium-bismuth solution as a fuel. The development of homogeneous aqueous reactors (HAR) has been the most rapid of the various fluid fuel types, probably because the physics experiments involved comparatively little experimental development. A number of reactors have been operated successfully, the most recent being the 5MW HRE-2 at Oak Ridge. In contrast only one fused salt reactor, the Aircraft Reactor Experiment (ARE), which had a very limited life, has operated and so far no liquid metal fuelled reactor (LMFR) has operated. This is partly a reflection of the relative degrees of experimental difficulty and partly of the effort applied reflected in the distribution of space in the book, between the three main types of system: HAR 566 pages, ARE 136 pages and LMFR 244 pages.

All three systems have the same ultimate objective —a breeder reactor, probably working on the Th^{232}/U^{233} cycle, incorporating integral chemical processing and using the fuel as the primary heat transfer fluid. Nearly all the systems considered have employed highly enriched fuel in thermal cores each using a different type of moderator (HAR-D_2O, ARE-BeF_2, LMFR-Graphite). These factors lead to compact cores with highly rated fuel, from which it follows that processing rates will be relatively high and neutron fluxes in the core very high. In the case of HAR and LMFR the favoured design is for a two-zone system with a U^{233} solution core surrounded by, but physically separated from, a thorium slurry breeder blanket. The advantages of such systems over conventional solid fuel reactors are the absence of a radiation damage limitation on fuel burn-up, lack of expense of complicated fuel fabrication processes, continuous removal of fission products and continuous make-up of fuel concentration. The HAR system offers the best neutron economy but the other two types offer high temperature, low pressure operation. In every case corrosion difficulties are the outstanding disadvantage.

In the HAR system the radiation-induced corrosion of the zirconium or Zircaloy-2 "window" between the core and the blanket has proved to be a major obstacle. It is now thought that the radiation-induced phase change in the ZrO_2 protective film causing the film to disrupt is probably the main corrosion-accelerating process. This had led to detailed studies of corrosion under irradiation, and to the development of new zirconium alloys and of titanium cladding as possible remedies. The problem has not yet, however, been fully solved and is one of the reasons for the considerable diminution of interest in HAR systems over the past year or two.

In the case of the fused salt reactor the corrosion problem seems to have been largely solved by the development of a new nickel-base alloy designated INOR-8 which combines the best characteristics of Inconel and Hastelloy B without their disadvantages. INOR-8 has excellent corrosion resistance to molten fluorides at temperatures well above those expected in a reactor. A great deal of work has been carried out on the fabrication and on the measurements of the properties of this alloy and is fully reported in this book.

Again the main materials problem of the LMFR system has been the development of a corrosion resistant container material. In this case a somewhat different approach is adopted in that a mildly corrodable steel ($2\frac{1}{4}$ % Cr, 1 % Mo) is used in conjunction with a corrosion inhibitor, zirconium, which forms a protective film of zirconium nitride and carbide on the steel surface. Extensive loop testing has developed this technique to a stage where it can be used with confidence. The study of the mechanism of the inhibition process, which also helps to protect the graphite moderator, is fascinating and it is a pity that it has not been described in this book in the detail which it deserves.

Apart from the work on problems of specific interest to these reactors there is much that is of far wider interest and application and it is probably this aspect which will give the book a fairly wide appeal. One of the best examples is the work on the HAR breeder blanket. In the first place the data on the physical and chemical properties of aqueous suspensions of oxides were not very comprehensive nor indeed well interpreted when this study was started and much of general value has been learned of the preparation, stability and flow behaviour of aqueous slurries. As part of this work it has proved necessary to investigate a variety of methods of producing UO_2 and ThO_2 particles of controlled size and shape, which is again of general interest.

The development of INOR-8 has been mentioned; here is another case where the material developed for a specific reactor application can find other uses in the chemical industry.

Many general problems associated with the use and handling of molten metals were investigated in the course of the LMFR study. In particular the process of thermal gradient mass transfer and its prevention by soluble inhibitors has been studied in detail. The

work has also led to consideration of fundamental aspects of liquid metal solubilities.

One could cite many other instances—development of impermeable graphite, the production of pure tantalum, remote maintenance of reactor components etc.—which illustrate the vast mine of useful information contained in this book.

Anyone who, like the reviewer, has been associated with work on fluid fuel systems will, on reading this book, feel a sense of disappointment, if not frustration that, on reaching this stage of development, a large-scale cut has been made over the past 18 months in the effort on such systems on both sides of the Atlantic. To the reviewer's knowledge only two teams in the world are currently pursuing integrated programmes on fluid fuel reactors; the LAMPRE plutonium-solution, tantalum-contained, fast reactor at Los Alamos and the Dutch UO_2-gas suspension (fluidized bed) reactor which, of course, is not mentioned in this book.

The fact that this book has been compiled with a separate editor and numerous contributors for each section, together with its length, mean that this is quite definitely a textbook of the type to which one refers for specific information rather than a coherent and easily readable account of fluid fuel reactor development. Moreover, it is a somewhat uncritical survey. Each section has been written by an enthusiast in his special field. A section by an uncommitted reactor technologist comparing the relative merits of the systems described and their advantages and disadvantages compared with solid fuel systems would have enhanced the value of the work. Nevertheless it will undoubtedly remain for many years the standard reference book on fluid fuel reactors.

B. T. R. FROST

SUMMARIES OF PHYSICAL RESEARCH IN METAL-LURGY, SOLID STATE PHYSICS AND CERAMICS. (USAEC, July 1959. TID-4005 (Pt-1, 5th Edition). 204 pages. Obtainable from Office of Technical Services, Department of Commerce, Washington 25, D.C., at $ 2.75.)

This is a useful survey of unclassified research work in progress at Universities and in industrial laboratories under USAEC sponsorship. About half of the 150 research projects are concerned with fundamental physical metallurgy of very diverse materials; the other half deal with the technology of reactor materials and with radiation damage. The total range covered by the projects is very wide.

Indexing is rather inadequate in that no page numbers are given and it is difficult to find a desired abstract quickly. In other respects the presentation is of a high standard.

FUEL ELEMENTS CONFERENCE. (USAEC, August 1950. TID-7559 (Part 1). 303 pages. Obtainable from Office of Technical Services, Department of Commerce, Washington 25, D.C., at $ 3.00).

This is a record of a conference held in May 1958 in the U.S.A. 17 of the 43 papers were classified and are not included here; in particular the classified group includes most of those under the headings "Non-Destructive Testing of Reactor Fuels" and "Mobile Reactors". Experience with some unconventional fuels, including U-ZrH and UO_2-ThO_2, is discussed, and several papers deal with problems of fabrication and design of fuel elements, including unusual forms such as tubular elements.

A significant amount of space is devoted to uranium oxide. Authors agree that this fuel is very little liable to fission gas swelling, and one paper goes in detail into the problem of calculating the life of UO_2 fuel elements on the criterion that life is limited by the time required to build up a maximum premissible released gas pressure. This and several other papers are followed by searching discussions which are a valuable part of the proceedings.

A final section consists of a number of brief papers in which experts evaluate future trends of fuel materials. This includes papers on U and U alloys, UO_2, dispersion fuels, fast reactor fuels, canning materials, reprocessing and radiation damage. The author of the last paper evidently felt something of an outsider and concludes plaintively: "Well, the other thing that I should like to anticipate is that some day there will be a fuel element conference and radiation damage will be the first thing on the program, not the last".

R. W. CAHN